

**DEVELOPMENT OF MULTILAYER LIQUID CRYSTAL POLYMER
BASED RADIO FREQUENCY FRONT-END
RECEIVING MODULE AT W-BAND**

by

Yifei Zhang

A dissertation submitted to the Faculty of the University of Delaware in partial fulfillment of the requirements for the degree of Doctor of Philosophy in Electrical and Computer Engineering

Spring 2016

© 2016 Yifei Zhang
All Rights Reserved

ProQuest Number: 10156508

All rights reserved

INFORMATION TO ALL USERS

The quality of this reproduction is dependent upon the quality of the copy submitted.

In the unlikely event that the author did not send a complete manuscript and there are missing pages, these will be noted. Also, if material had to be removed, a note will indicate the deletion.



ProQuest 10156508

Published by ProQuest LLC (2016). Copyright of the Dissertation is held by the Author.

All rights reserved.

This work is protected against unauthorized copying under Title 17, United States Code
Microform Edition © ProQuest LLC.

ProQuest LLC.
789 East Eisenhower Parkway
P.O. Box 1346
Ann Arbor, MI 48106 - 1346

**DEVELOPMENT OF MULTILAYER LIQUID CRYSTAL POLYMER
BASED RADIO FREQUENCY FRONT-END
RECEIVING MODULE AT W-BAND**

by

Yifei Zhang

Approved: _____
Kenneth E. Barner, Ph.D.
Chair of the Department of Electrical and Computer Engineering

Approved: _____
Babatunde Ogunnaike, Ph.D.
Dean of the College of Engineering

Approved: _____
Ann L. Ardis, Ph.D.
Senior Vice Provost for Graduate and Professional Education

I certify that I have read this dissertation and that in my opinion it meets the academic and professional standard required by the University as a dissertation for the degree of Doctor of Philosophy.

Signed:

Dennis W. Prather, Ph.D.
Professor in charge of dissertation

I certify that I have read this dissertation and that in my opinion it meets the academic and professional standard required by the University as a dissertation for the degree of Doctor of Philosophy.

Signed:

Mark S. Mirotznik, Ph.D.
Member of dissertation committee

I certify that I have read this dissertation and that in my opinion it meets the academic and professional standard required by the University as a dissertation for the degree of Doctor of Philosophy.

Signed:

Keith W. Goossen, Ph.D.
Member of dissertation committee

I certify that I have read this dissertation and that in my opinion it meets the academic and professional standard required by the University as a dissertation for the degree of Doctor of Philosophy.

Signed:

Shouyuan Shi, Ph.D.
Member of dissertation committee

I certify that I have read this dissertation and that in my opinion it meets the academic and professional standard required by the University as a dissertation for the degree of Doctor of Philosophy.

Signed:

Richard D. Martin, Ph.D.
Member of dissertation committee

ACKNOWLEDGMENTS

There are many people to whom I must express my deepest gratitude. Without their helps and encouragements, this dissertation would never have been completed.

First, I must thank my advisor, Dr. Dennis W. Prather, whose guidance, persistence, and vision have been the guiding light for my research. Your belief and support have encouraged me throughout the whole journey. You have been a great mentor and inspired me to broaden my horizon.

To all the members of this community, I must express my sincerest thanks. I would like to particularly thank: Dr. Shouyuan Shi for your brilliant guidance, valuable suggestions, and kind patience throughout this process, Dr. Richard D. Martin for your remarkable management and coordination in this research and irreplaceable experiences and contributions in device manufacturing and measurement, Dr. Peng Yao for your outstanding integration techniques and professional suggestions in the millimeter wave measurement, Andrew A. Wright and Kevin Shreve for your excellent integration and packaging techniques. I would also like to thank my colleagues, Dr. Christopher A. Schuetz, Dr. Garrett Schneider, Dr. Janusz Murakowski, Dr. Rownak Shireen, Dr. Yuehao Wu, Dr. Jian Bai, Dr. David Eng, Dr. David W. Grund, Stephen Kozacik, Maciej Murakowski, Matthew R. Konkol, Andrew Mercante, Dylan Ross, and the rest of the group members for your great helps and sharing your experience in this work. May our friendships last a lifetime.

I would like to express my most genuine thanks to: all the members of my committee for reviewing my dissertation, attending my defense, and helping me

through this process, Mr. Bruce Wallace and other program officers at Defense Advanced Research Projects Agency (DARPA) for generously supporting this work, Jesse Ward and Brent Mayfield at Compunetics Inc. for your great supports in fabrication and manufacturing.

Finally, I would like to thank my family and friends. To my father, thank you for teaching me the persistence and providing me the foundation to allow me to make this journey. To my mother, thank you for your unconditional love, support, and encouragement throughout my life. To my aunt, thank you for exciting me the self-confidence and faith to reach the final destination. To Dr. Tian Gu and Dr. Liang Qiu, thank you for your selfless helps and precious friendships in the department.

TABLE OF CONTENTS

LIST OF TABLES	x
LIST OF FIGURES	xi
ABBREVIATIONS	xv
ABSTRACT	xviii
Chapter	
1 INTRODUCTION	1
1.1 Millimeter Wave Frequencies	1
1.2 W-band Frequencies and Their Challenges	3
1.2.1 PCB Materials	4
1.2.2 Fabrication Limits	7
1.2.3 Electromagnetic Interference	8
1.2.4 Measurement Limits	9
1.3 Wireless Systems and Their Applications at W-band	10
1.3.1 Wireless Communication Systems	10
1.3.2 Radar Systems	12
1.3.3 Radiometry Systems	14
1.4 W-band Front-End Receiving Module in Multilayer LCP Substrates	17
1.4.1 State-of-The-Art	17
1.4.2 Multilayer Circuitry	18
1.5 Dissertation Outline	19
1.6 List of Original Contributions	20
2 HIGH-GAIN LINEARLY TAPERED ANTIPODAL SLOT ANTENNA AT E- AND W-BANDS	26
2.1 System Aspects of Receiving Antennas	26
2.2 Challenges for W-band Antennas	28

2.2.1	Design Aspect.....	28
2.2.2	Measurement Aspect	29
2.3	Linearly Tapered Antipodal Slot Antenna	30
2.3.1	LTASA Design.....	32
2.3.2	Bandwidth Measurement.....	37
2.3.3	Far-field Measurement	38
2.3.3.1	Optically addressed far-field measurement system	38
2.3.3.2	Characterized radiation patterns and gain	41
2.4	Summary.....	42
3	TRANSITIONS IN MULTILAYER LCP SUBSTRATES	44
3.1	Transmission Lines and Waveguides	44
3.2	CBCPW-to-Stripline Vertical Transition	47
3.2.1	Transition Design	48
3.2.2	Measurement	50
3.2.2.1	System set-up.....	50
3.2.2.2	Back-to-back transition	52
3.3	MS-to-SIW Transition.....	54
3.3.1	Transition Design	55
3.3.2	Measurement	57
3.3.2.1	CBCPW probe pad	57
3.3.2.2	Back-to-back transition	59
3.4	SIW-to-Waveguide Transition	61
3.4.1	Transition Design	62
3.4.2	Measurement	65
3.5	MS-to-CPW Transition	67
3.5.1	Transition Design	68
3.5.2	Measurement	69
3.6	Summary.....	71

4	MULTI-CHIP MODULE INTEGRATION AND PACKAGE	72
4.1	NG ALP283 Low Noise Amplifier	74
4.2	Multilayer-LCP MMIC Carrier	76
4.3	V-Shape Wire Bond	78
4.4	Multi-Chip Module.....	82
4.4.1	Single-LNA Module.....	82
4.4.2	Double-LNA Module	83
4.5	Packaging Technologies	87
4.6	Summary.....	87
5	SIW FILTER AND DIRECTIONAL FILTER AT W-BAND	89
5.1	Challenges for W-band Filters.....	90
5.2	SIW Filter at 94 GHZ.....	92
5.2.1	SIW Filter Design.....	93
5.2.2	Measurement	96
5.3	Directional Filters at 95 GHZ.....	96
5.3.1	Directional Coupler Design.....	99
5.3.1.1	Slot coupling of the vertically overlapped MS lines ..	100
5.3.1.2	Dual-slot directional coupler	102
5.3.2	Directional Filter Design	104
5.3.2.1	Single-loop directional filter.....	106
5.3.2.1.1	Symmetric loop	106
5.3.2.1.2	Asymmetric loop	107
5.3.2.2	Double-loop directional filter	108
5.3.3	Hybrid Substrates and Measurement.....	111
5.3.3.1	Hybrid substrates	111
5.3.3.2	Measurement set-up and W-band load	112
5.3.3.3	Measured S-parameters	113
5.3.3.3.1	Single-loop DFs.....	114
5.3.3.3.2	Cascaded double-loop DFs.....	114

5.4	Summary.....	117
6	CONCLUSION AND FUTURE WORK.....	119
6.1	Conclusion.....	119
6.2	Future Work.....	122
	REFERENCES.....	126
Appendix		
	COPYRIGHT PERMISSION	136

LIST OF TABLES

Table 1.1.	Material properties of traditional and new PCB substrates [4] and [6]-[8].	6
Table 2.1.	Optimized dimensions of the proposed LTASA.	34
Table 2.2.	Simulated gain, beamwidth, first sidelobe, and cross-polarization of the proposed LTASA.	35
Table 3.1.	Fundamental mode, dimensions, and simulated propagation loss and impedance at W-band of the five planar transmission components on a 100 μ m thick LCP substrate and WR-10 rectangular waveguide.	46
Table 3.2.	Cut-off frequency of the SIWs and dimensions of the corresponding MS-to-SIW transitions.	56
Table 4.1.	Resistance, inductance, and capacitance of the circuit module for the V-shape wire bond.	81
Table 5.1.	Material properties of the substrates and dimensions of the HFSS models and fabricated devices	113
Table 5.2.	Insertion loss, bandwidth, and out-of-band rejection of the directional filters.	116

LIST OF FIGURES

Figure 1.1.	Electromagnetic spectrum and the corresponding applications [1].	2
Figure 1.2.	Propagation attenuation of electromagnetic waves in atmospheric conditions with different relative humidity (RH) and fog visibility [2].	3
Figure 1.3.	(a) World PCB production by type of substrates in 2010 from Ref. [5], and (b) market response of frequencies reported by military and aerospace participants from Ref. [3].	5
Figure 1.4.	Block diagram of a basic wireless communication system [11].	11
Figure 1.5.	Block diagram of a basic monostatic radar system [11].	13
Figure 1.6.	Block diagram of a basic microwave radiometer [11].	15
Figure 2.1.	Configuration of the proposed linearly tapered antipodal slot antenna.	33
Figure 2.2.	Simulated S11 of the LTASA and measured S11 of the LTASAs integrated with a via-less CBCPW probe pad and a MS-to-SIW-to-waveguide transition.	35
Figure 2.3.	Simulated and measured radiation patterns of the LTASA at (a) 75 GHz, (b) 80 GHz, (c) 85 GHz, (d) 90 GHz, and (e) 95 GHz.	36
Figure 2.4.	Fabricated LTASAs with a via-less CBCPW probe pad and a MS-to-SIW-to-waveguide transition.	37
Figure 2.5.	(a) Configuration of the SIW-to-waveguide transition, and (b) measured and simulated S-parameters of its back-to-back transition.	39
Figure 2.6.	Optically addressed far-field measurement system.	40
Figure 2.7.	Simulated and measured gain spectrum of the proposed LTASA.	42
Figure 3.1.	Cross-section structure and fundamental mode profile of MS line, CPW, CBCPW, stripline, SIW, and rectangular waveguide.	45

Figure 3.2. (a) Cross section and (b) layer-by-layer configuration and dimensions of the CBCPW-to-SL transition.	49
Figure 3.3. Simulated S-parameters of a CBCPW-to-SL transition: (a) tolerance analysis of the diameter of the blind via, and (b) tolerance analysis of the pitch between the blind and through vias.	51
Figure 3.4. (a) Fabricated CBCPW-to-SL-to-CBCPW transition, and (b) cross-section cut of the fabricated back-to-back transition.	52
Figure 3.5. Simulated and measured S-parameters of the back-to-back transition with a 3 mm long SL.	53
Figure 3.6. Configuration of the MS-to-SIW transition.	56
Figure 3.7. Simulated S-parameters of a MS-to-SIW transition ($w = 1.7$ mm).	57
Figure 3.8. (a) Configuration of a CBCPW probe pad and its back-to-back transition, (b) simulated and measured S-parameters of a 5mm long MS line terminated with a pair of probe pads, and (c) calculated propagation loss of a MS line and insertion loss of a pair of probe pads.	58
Figure 3.9. (a) Fabricated MS-to-SIW-to-MS transition, and (b) simulated and measured S-parameters of the back-to-back transition ($w = 1.7$ mm).	60
Figure 3.10. Configuration and dimensions of the SIW-to-WG transition in multilayer LCP substrates.	63
Figure 3.11. (a) Propagation and cross-section of the fundamental and parasitic modes of the proposed SIW-to-WG transition, and simulated (b) S11 and (c) S21 of the transition with varying L at W-band.	64
Figure 3.12. (a) Fabricated waveguide-to-SIW-to-waveguide transition with metal housing, and (b) simulated and measured S-parameters of the back-to-back transition.	66
Figure 3.13. Configuration of the MS-to-CPW transition.	69
Figure 3.14. (a) Fabricated MS-to-CPW transition with a CBCPW probe pad, and (b) simulated and measured S-parameters of this transition.	70
Figure 4.1. (a) Top view, (b) measured on-chip gain, and (c) calculated input and output impedances of the NG ALP283 LNA.	75

Figure 4.2.	Layer-to-layer circuit schematic of the multilayer LCP carrier.....	77
Figure 4.3.	(a) Configuration of the V-shape wire bond and traditional single wire bond, (b) simulated S-parameters of these two wire bonds as well as the circuit module (CM) of the V-shape wire bond, and (c) calculated input and output impedances of the wire bonds.....	79
Figure 4.4.	Equivalent circuit model of the proposed V-shape wire bond.....	81
Figure 4.5.	(a) Configuration of the single-LNA module, (b) simulated net loss of the single-LNA module and double-LNA module, and (c) measured and calculated net gain of the single-LNA module.....	83
Figure 4.6.	Packaged double-LNA module and 3-D printed housing.....	84
Figure 4.7.	Measured and calculated (a) net gain, (b) unwrapped phase, and (c) noise figure of the double-LNA module.....	86
Figure 5.1.	Configuration of the second-ordered SIW filter fed by MS lines.....	94
Figure 5.2.	(a) Fabricated second-ordered SIW filter, and (b) simulated and measured S-parameters of the SIW filter.....	95
Figure 5.3.	Traditional directional filters: (a) waveguide-based, (b) standing-wave I, (c) standing-wave II, and (d) travelling-wave.....	97
Figure 5.4.	(a) Configuration, electric fields, and equivalent circuit models of the slot-coupled vertically overlapped MS lines, and simulated S-parameters of the slot-coupled MS lines with (b) different LCP thickness and (c) slot size.....	101
Figure 5.5.	(a) Configuration, (b) simulated S11 and S31, and (c) simulated S21 and S41 of the directional coupler in LCP substrates and hybrid substrates.....	103
Figure 5.6.	(a) Configuration of the single-loop DFs with symmetric and asymmetric loop topologies in multilayer LCP substrates, and simulated S-parameters of the (b) symmetric and (c) asymmetric DFs with $p_s = 0.35$ mm.....	105
Figure 5.7.	Simulated (a) effective dielectric constant and (b) loss of MS lines with a width of $160\ \mu\text{m}$ on a $100\ \mu\text{m}$ LCP substrate and a $50\ \mu\text{m}$ LCP substrate laminated with a $66\ \mu\text{m}$ AG bond-ply.....	106

Figure 5.8. (a) Configuration of the cascaded double-loop DF with asymmetric loops, and simulated S-parameters of the cascaded DF with $P_d =$ (b) 1.9 mm and (c) 2.3 mm.	109
Figure 5.9. Fabricated single-loop and cascaded DFs with RF absorbers.....	113
Figure 5.10. Measured and simulated S-parameters of (a) the asymmetric single-loop DF with $p_s = 0.37$ mm and cascaded double-loop DFs with $P_d =$ (b) 1.9mm and (c) 2.3 mm.	115
Figure 6.1. Configuration of a multilayer LCP-based ultra-wideband front-end module.....	122
Figure 6.2. Passive mmW imager at 77 GHz.	124
Figure 6.3. Packaged receiving module based on multilayer LCP substrates for mmW imaging at 95 GHz.	125

ABBREVIATIONS

RF: Radio Frequency

IR: Infrared

mmW: Millimeter Wave

AM: Amplitude Modulation

FM: Frequency Modulation

TV: Television

GPS: Global Positioning System

RFID: Radio Frequency Identification

HDI: High Density Interconnection

PCB: Printed Circuit Board

CTE: Coefficient of Thermal Expansion

PTFE: Polytetrafluoroethylen

LTCC: Low Temperature Co-fired Ceramic

LCP: Liquid Crystal Polymer

EMI: Electromagnetic Interference

RFI: Radio-Frequency Interference

EMC: Electromagnetic Compatibility

DUT: Device Under Test

SMC: Surface-Mounted Connector

G-S-G: Ground-Single-Ground

WLAN: Wireless Local Area Network

DBS: Direct Broadcast Satellite

FCC: Federal Communication Commission

RCS: Radar Cross Section

ECCM: Electronic Counter-countermeasures

LNA: Low Noise Amplifier

IF: Intermedium Frequency

SNR: Signal-to-Noise Ratio

SWaP: Size, Weight, and Power

LTASA: Linearly Tapered Antipodal Slot Antenna

CBCPW: Conductor-Backed Co-Planar Waveguide

MS: Microstrip

SIW: Substrate Integrated Waveguide

UWB: Ultra-Wideband

NF: Noise Figure

AUT: Antenna Under Test

TSA: Tapered Slot Antenna

CPW: Co-Planar Waveguide

PA: Power Amplifier

ASL: Antipodal Slot-line

APSL: Antipodal Parallel Stripline

HFSS: High Frequency Structural Simulator

SOLT: Short-Open-Load-Through

PNA: Programmable Network Analyzer

EO: Electro-Optic

DWDM: Dense Wavelength Division Multiplexing

SL: Stripline

FEM: Finite Element Method

RWG: Rectangular Waveguide

MMIC: Monolithic Microwave/Millimeter Integrated Circuit

MCM: Multi-Chip Module

SOP: System On Package

SCM: Single-Chip Module

ADS: Advanced Design System

ABSTRACT

To extend the sensing of human vision, radio frequencies have found prolific wireless applications in everyday life, e.g., wireless communication, radar, and radiometry. To overcome the crowded microwave spectrum, millimeter wave (mmW) frequencies have gained tremendous interest in these systems within several spectral windows, i.e., 35 GHz, 77 GHz, 95 GHz, and 140 GHz, due to their low atmospheric propagation loss. Additionally, mmWs can provide gigabyte data transmission rates for wireless communication systems and high resolution for radar and radiometry systems. To date, most mmW wireless systems have been implemented at Ka-band, i.e., 35 GHz, where they can be directly extended from the traditional microwave systems. However, as the frequency increases to W-band, such as 77 GHz and 95 GHz, RF engineers encounter nontrivial challenges from various technical aspects.

In a general sense, the most critical part of wireless communication, radar, and radiometry systems is the receiver. Despite the different mechanisms and applications of these receivers, it should be noted that they have similar front-end components, i.e., antennas, pre-amplifiers, and filters. Assembling these components can achieve a front-end receiving module, which could potentially be utilized in most wireless systems.

To this end, I present my work on the development of a W-band front-end receiving module, consisting of a high-gain antenna, high-gain low noise amplifiers, bandpass filters, transmission lines, and their transitions for interconnection. To

minimize the dielectric loss, liquid crystal polymer (LCP) is selected as the module substrate, which has a low loss tangent and low dielectric constant at W-band. To achieve high density, light weight, low profile, and low power consumption, the proposed module is designed on a multilayer circuit. The multilayer circuit is fabricated using the commercial state-of-the-art large-panel circuit print technologies, achieving low unit price and short manufacturing cycle. Multi-chip module packaging technologies have been developed to achieve a net gain of more than 50 dB for the proposed module, while maintaining linear phase and low electromagnetic interference. By using the state-of-the-art low noise amplifiers, the noise figure of the module can be minimized below 6 dB at W-band, which can satisfy most wireless receiving applications. The designed antenna, transitions between various transmission lines, low noise amplifiers, and developed integration and packaging technologies achieve an ultra-wide bandwidth that covers most of the frequencies in the W-band, providing sufficient bandwidth for gigabyte data transmission rates in wireless communication systems. For narrow-band applications, i.e., radiometry and frequency division multiplexing, the designed filters and directional filters can be utilized to pick out the frequencies of interest. In conclusion, the proposed front-end receiving module may find many applications in various wireless systems at W-band, i.e., wireless communication, radar, and radiometry.

Chapter 1

INTRODUCTION

1.1 Millimeter Wave Frequencies

Visible light, mainly emitted by our sun, is located within an electromagnetic spectrum with a wavelength between 390 and 700 nm. To sense objects in other regions of the electromagnetic spectrum, such as radio frequency (RF), infrared (IR), and X-ray, various instrumental technologies have been developed. For instance, RF radar systems provide significantly larger range and resistance to atmospheric disturbances for remote sensing and tracking. IR cameras provide night vision by capturing terrestrial temperature radiation at wavelengths of approximately ten microns. X-ray systems have been utilized for medical and security screening due to their ability to penetrate optically opaque materials. To date, electromagnetic frequencies have found prolific irreplaceable applications in our daily life, such as amplitude modulation (AM)/frequency modulation (FM) radio, television (TV) broadcast, global positioning system (GPS), remote control, wireless communication, fiber optic communication, astronomy, and RF identification (RFID).

However, it should be noted that there exists a region of the electromagnetic spectrum, between microwave and IR frequencies, with relatively less exploration, which is referred to as the millimeter wave (mmW) region. As its name implies, mmW spectrum has a wavelength measured on the order of millimeters in free space and extends from 30 to 300 GHz, as can be seen in Figure 1.1. Typically, the microwave spectrum is defined from 300 MHz to 300 GHz, covering mmW frequencies. However,

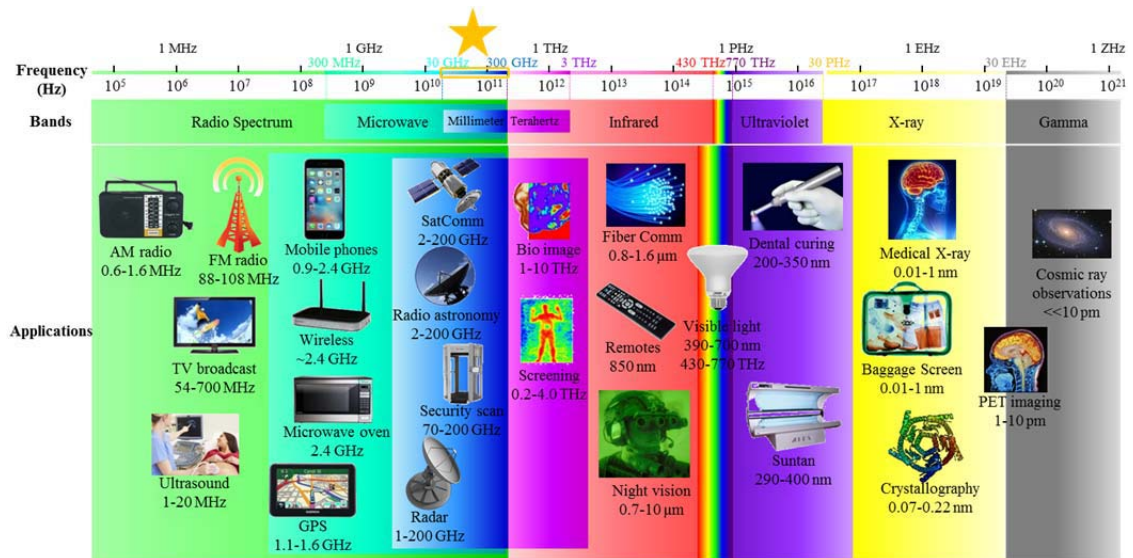


Figure 1.1. Electromagnetic spectrum and the corresponding applications [1].

most microwave systems and devices are developed below 30 GHz. To distinguish mmW from microwave, in this dissertation microwave frequencies are considered from 300 MHz to 30 GHz.

The relatively ‘unused’ mmW frequencies can provide many remarkable advantages to current wireless applications. On one hand, when compared to microwave systems, mmW frequencies can provide high resolution with low profile, while maintaining the high reflectivity contrast provided by good conductors. On the other hand, mmW radiation addresses a unique ability to penetrate fog, cloud, smoke cover, and sand and dust storms, which blind all current optical and IR systems. Also, millimeter waves can penetrate thin dielectrics, e.g., clothing and thin walls. For these reasons, this frequency range has gained tremendous interest in various applications,

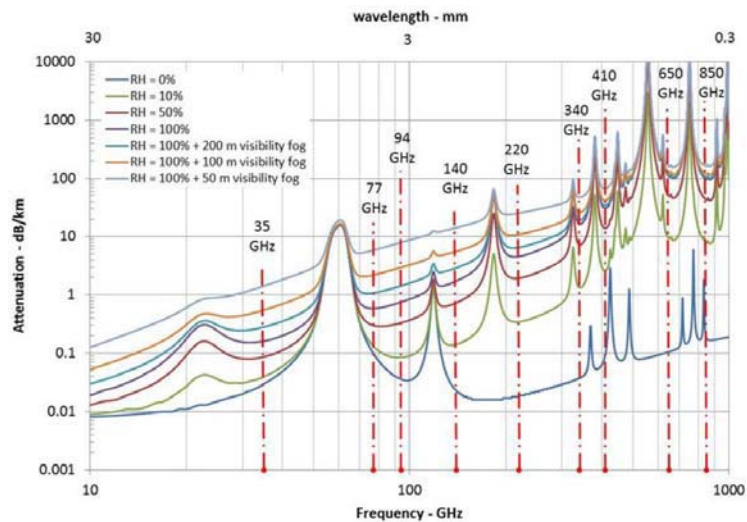


Figure 1.2. Propagation attenuation of electromagnetic waves in atmospheric conditions with different relative humidity (RH) and fog visibility [2].

spanning from remote sensing, security scanning, collision avoidance radar, high data rate communication, satellite and aircraft radars, to imaging.

1.2 W-band Frequencies and Their Challenges

For wireless systems, which constitute many of the contemplated mmW applications, the level of atmospheric attenuation experienced is of paramount importance. Water vapor and atmospheric oxygen introduce a high level of attenuation at certain frequencies within the mmW regime. Figure 1.2 illustrates the atmospheric absorption of electromagnetic waves with different levels of relative humidity and fog visibility [2]. It can be seen that there are four spectral windows of interest for wireless applications centered at 35 GHz, 94 GHz, 140 GHz, and 220 GHz. Each window has relative pros and cons. Using the 220 GHz window can provide over six times more

spatial resolution than the 35 GHz window, however, with a cost of largely increased atmospheric absorption, i.e., from 1.5 dB/km to 20 dB/km. To date, most mmW systems have been developed at *Ka*-band, i.e., 35 GHz, mainly due to the ease of detector fabrication as well as the availability of material and source. As the frequency increases to *W*-band, namely 75-110 GHz, the traditional wireless systems suffer from significant challenges of various aspects, i.e., substrate material, fabrication resolution and tolerance, electromagnetic interference (EMI), and measurement. These challenges are discussed in detail separately in the following subsections.

1.2.1 PCB Materials

Printed circuit boards (PCBs) mechanically support and electrically connect electronic components using conductive tracks, pads, and other features, which serve as the foundation for virtually all wireless electronic products, ranging from consumer products, i.e., smartphones, touch screen tablets, and personal computers, to high-end commercial electronic equipment and aerospace and defense electronic systems. According to the estimates from the Institute for Interconnecting and Packaging electronic Circuits (IPC)-Association Connecting Electronics Industries, the worldwide market for PCBs is approximately \$59 billion in 2012 [3]. As can be seen in Figure 1.3, the PCBs' application trend is towards high frequencies and high density interconnection (HDI), in terms of multilayer circuitry and micro vias, which introduces critical challenges to the traditional PCB materials. For instance, FR-4, the most traditional and well-known PCB material, still having lots of applications in planar and rigid-flexible circuits, has a significant loss tangent of higher than 0.025 at *W*-band [4]. Polyimide, which dominates 85% of the flexible circuit market [4] and large portion of the multilayer circuit market, also suffers from high loss at high

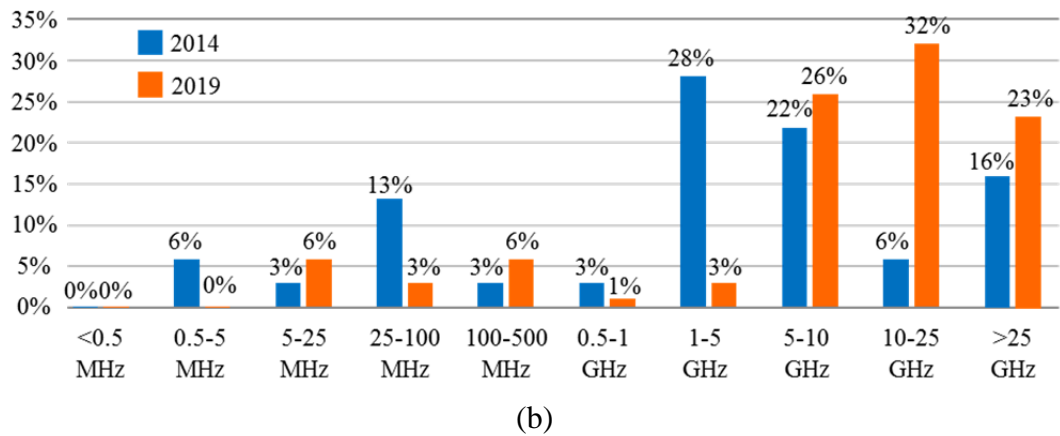
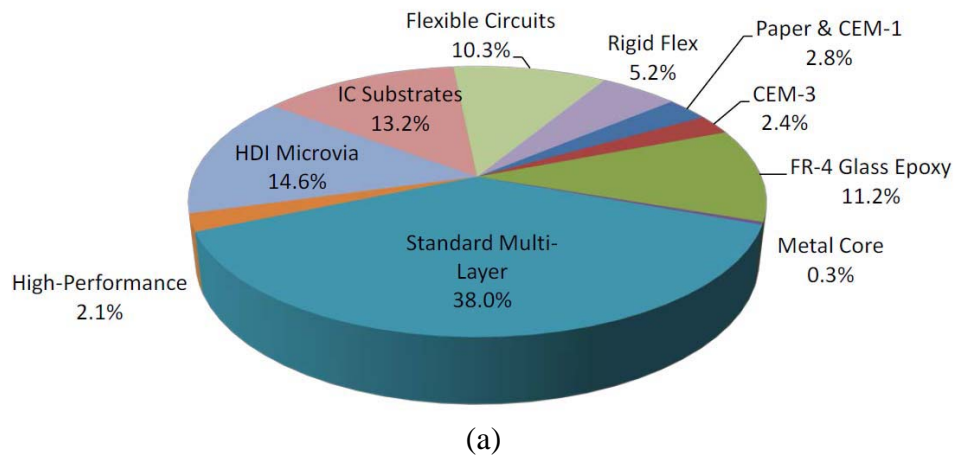


Figure 1.3. (a) World PCB production by type of substrates in 2010 from Ref. [5], and (b) market response of frequencies reported by military and aerospace participants from Ref. [3].

frequencies as well as high water absorption. To date, tremendous efforts have been done to investigate new materials for high-frequency applications. Table 1.1 lists the materials properties, including dielectric constant, loss tangent, water absorption,

Table 1.1. Material properties of traditional and new PCB substrates [4] and [6]-[8].

Substrate	Dielectric constant	Loss tangent	Water absorption	CTE (ppm/°C)	Density (g/cm³)	Test frequency
FR-4	4-4.8	0.025	0.15%	15	1.85	<10 GHz
Polyimide	2.9-3.9	0.03	1%-5%	20	1.4-1.7	<10 GHz
PTFE	2.1-2.5	0.003	0.03%	>112	2.1	<100 GHz
LTCC	5.7-9.1	<0.0063	0	5.8-7	3.2	<12 GHz
LCP	2.9-3.2	<0.0045	0.04%	0-40	1.4	<110 GHz

coefficient of thermal expansion (CTE), and density of some traditional and new substrate materials. To minimize the dielectric loss in printed circuits at high frequencies, low loss tangent and low dielectric constant are of primary importance. Polytetrafluoroethylen (PTFE) Teflon, low temperature co-fired ceramic (LTCC), and liquid crystal polymer (LCP) are the three promising candidates for high frequency applications. PTFE can provide low dielectric constant and low loss tangent below 100 GHz. However, its CTE is as high as 110 ppm/°C [6], which is much larger than that of the traditional cladding metals, e.g. 16.8 ppm/°C for gold. LTCC is hermetic, and has zero water absorption. However, it is expensive, has relatively high dielectric constant and density, and requires a high temperature of 850°C for multilayer lamination [7]. Among these three materials, LCP has gained tremendous interest due to its perfect material properties. LCP is cheap and flexible, and has a tunable CTE from 0 to 40 ppm/°C, which can be compatible with most traditional metal claddings, i.e., gold, copper, and silver. It can provide a low dielectric constant from 2.9 to 3.2 and a low loss tangent of less than 0.0045 from DC up to 110 GHz [8]. Also, LCP is preferred for multilayer circuitry due to its low lamination temperature of less than

300 °C. However, LCP has not been widely used so far. Many PCB manufacturers do not provide LCP as PCB material.

1.2.2 Fabrication Limits

PCBs can be manufactured mechanically using PCB milling or laser ablation, or chemically using photolithography techniques. To reduce the cost and manufacturing cycle, the printed circuits of wireless systems are typically fabricated using commercial large-panel PCB technologies, which, however, have to sacrifice the resolution of circuit components. In this section, I depict the limits of commercial large-panel fabrication technologies that will be employed for the development of the front-end receiving module in this dissertation.

Typically, laser ablation and photolithography techniques are preferable to achieve better fabrication resolution for printed circuits. However, their resolutions are limited by the laser spot size and aspect ratio of the etch solution. To date, the resolution of circuit patterns fabricated using the state-of-the-art commercial large-panel PCB technologies is 2 mil or 50.8 μm [9], which is electrically ‘small’ at microwave frequencies. As the frequency increases to *W*-band, the feature dimensions of the circuit devices reduce dramatically. In this case, some traditional transmission lines, e.g., slot-lines and coupled microstrip lines [10], become very lossy and some tightly-coupled devices cannot obtain sufficient coupling, e.g., planar quarter-wavelength directional coupler [11] at such high frequencies. To mitigate this problem, thin metal claddings or electroplating have been utilized to achieve higher resolution [8]. However, they are expensive for large-panel, large-quantity applications.

The HDI multilayer circuits are stacked by using bond plies to laminate core layers and micro vias to connect different circuit layers. Under commercial standards,

vias are typically drilled by using a laser at high frequencies. Limited by the laser spot size, e.g., 200 μm for neodymium-doped yttrium aluminium garnet (Nd:YAG) laser in Compunetics Inc. [9], the vias' resolution is determined by the substrate thickness and laser drilling aspect ratio, the latter of which is suggested to be larger than 1.25:1 [9] [12]. That is to say, on a 200 μm thick substrate, the diameter and pitch of the vias should be larger than 250 μm , which is electrically 'small' at microwave frequencies. However, at *W*-band, the pitch and diameter of the vias (250 μm) become electrically 'large' in terms of wavelength, which may increase the radiation loss of transmission lines, e.g., substrate integrated waveguides (SIWs), and parasitic capacitance for substrate modes. The ring pad of a via is typically 125 μm larger than the via itself [9], which may lead to impedance mismatch and parasitic capacitance at *W*-band. Also, the multilayer devices are sensitive to the layer-to-layer registration tolerance and bond-ply thickness variations at such high frequencies.

1.2.3 Electromagnetic Interference

Electromagnetic interference, also called radio-frequency interference (RFI) in the RF spectrum, is a disturbance generated by an external source that affects an electrical circuit by electromagnetic induction, electrostatic coupling, or conduction. The EMI discussed in this section is between the circuit components on the circuit level. As the device dimensions scale down at *W*-band, the device density increases significantly and, thereby, many EMI problems may be easily excited in printed circuits in term of crosstalk between the adjacent devices and transmission lines. The crosstalk typically occurs in the near field region by means of substrate modes in the circuit substrate, surface waves above the ground, or radiation in free space. For instance, at *W*-band, the vias with electrically 'large' diameter in electrically 'thick'

substrates may excite substrate modes more easily [13] and a traditional single wire bond may radiate energy to free space and excite surface waves [14].

On the circuit level, EMI may increase the noise floor and data error rate of the transmitting signals and degrade the performance of active devices, e.g., oscillation in amplifiers. To minimize the crosstalk between circuit components and improve electromagnetic compatibility (EMC) of the proposed module at *W*-band, shielding structures, such as via barriers and SIWs, may be desired in the substrates to eliminate substrate modes, and conductive housing may be desired to encapsulate the active components and isolate them in free space. Also, attenuation structures and absorption materials may be of great interest for some applications, e.g., high-gain cascaded active components.

1.2.4 Measurement Limits

An RF device under test (DUT) is typically characterized using a network analyzer to measure its S-parameters. At microwave frequencies, the DUT can be integrated with surface-mounted connectors (SMCs) and connected to the analyzer using coaxial cables. However, at *W*-band, coaxial cables and SMCs are lossy and expensive [15]-[16]. Alternatively, WR-10 waveguides can be utilized for connection, and ground-signal-ground (G-S-G) probes can be employed to couple RF signals into and out of the DUT. However, waveguides are rigid and bulky and probes are easily broken, which introduces many difficulties to the measurement system set-up. For a multi-port DUT, 50 Ω resistors are typically employed as good loads to minimize the reflection in measurement and practical applications at low frequencies. However, the state-of-the-art 50 Ω resistors can only work up to 50 GHz, and become significantly

inductive at *W*-band [17]. In this case, new loads and attenuation structures have to be investigated for high frequency applications.

The measurement of an antenna is different from that of the non-radiating DUT. To characterize an antenna's far-field properties, far-field or near-field antenna measurement systems have to be employed. At *W*-band, commercial antenna measurement systems are very expensive. Thus, to build a far-field measurement system at *W*-band, lossy coaxial cables and connectors, unbendable waveguides, vulnerable probes, and bulky and heavy rotation stage may have to be utilized, which may introduce many challenges into the measurement system. Also, antennas are more sensitive to electrically 'large' metallic structures in their near field region at *W*-band. To date, many antennas reported at *W*-band cannot be demonstrated experimentally [18] or have to be demonstrated at microwave frequencies with scaled dimensions [19].

1.3 Wireless Systems and Their Applications at *W*-band

A wireless system consists of passive and active RF components arranged to perform a useful function without the use of wires. The three most important and widely-used wireless systems are wireless communication, radar, and radiometry. In this section, I will discuss the basic conception of these three systems to reveal a general overview of their similarity and applications at *W*-band.

1.3.1 Wireless Communication Systems

Wireless communication systems transfer information between two points without direct physical connection, which can be achieved by using sound, infrared, optical, or radio frequency energy. Most modern wireless systems utilize RF frequencies that range from 800 MHz to a few GHz, which are able to penetrate fog,

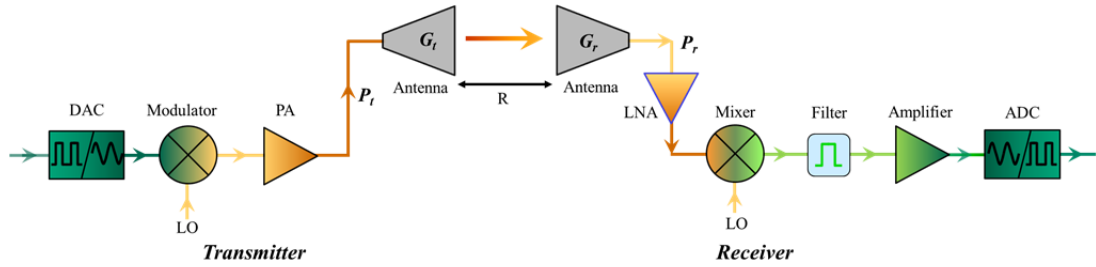


Figure 1.4. Block diagram of a basic wireless communication system [11].

rain, snow, dust, and foliage. Their applications can be found in broadcast radio and television, cellular phone and networks, wireless local area networks (WLAN), GPS, direct broadcast satellite (DBS) service and so on. To avoid the crowded microwave spectrum, *W*-band frequencies have gained great interest for wireless communications because they can provide high data transmission rates up to tens of gigabyte/second. Recently, the Federal Communication Commission (FCC) has defined 75 GHz, 85 GHz, and 95 GHz for gigabyte data rate communications, which may be utilized in local area networks, metropolitan links, satellite and aircraft communications, and future cellular phones.

The block diagram of a general wireless communication system is illustrated in Figure 1.4. The baseband signals are modulated onto a carrier, amplified, and then radiated by the transmitting antenna. The power captured by the receiving antenna can be expressed as [11]:

$$P_r = \frac{G_t G_r \lambda^2}{(4\pi R)^2} P_t, \quad (1.1)$$

where G_t and G_r are the gains of the transmitting and receiving antennas, respectively, λ is the wavelength in free space, R is the distance between the transmitter and receiver, and P_t is the transmit power. This equation is known as *Friis radio link formula*, which can be interpreted as the maximum possible received power in practice. According to Equation (1.1), to capture more power for the receiver, the receiving antenna should have high gain. Next, on the receiver side, the received signals are pre-amplified, down-converted to the baseband, filtered, amplified, and then converted to digital signals.

1.3.2 Radar Systems

Radar (RADio Detection And Ranging) is an electromagnetic system for detection and location of remote objects and constructs one of the oldest applications of RF wireless technology, dating back to World War II. It operates by transmitting a particular type of waveform and detecting the nature of the echo signal reflected back from a distant object [20]. Radar is employed to extend the capability of a person's senses for observing the environment. It can see through the conditions that are impervious to human vision, such as darkness, haze, fog, rain, and snow, and can measure the relative distance and velocity of the target. Its applications can be found in civilian and military systems, such as airport surveillance, navigation, detecting and targeting, mapping and imaging, astronomy, reconnaissance, and speed measurement.

Based on the mechanism, radar systems can be classified into two categories: monostatic radar and bistatic radar. The former uses the same antenna for both transmitting and receiving, while the latter uses two separate antennas to achieve the same functions. Since most radar systems are monostatic, I only give the radar equation for the monostatic radar in this section. The bistatic case is very similar. The

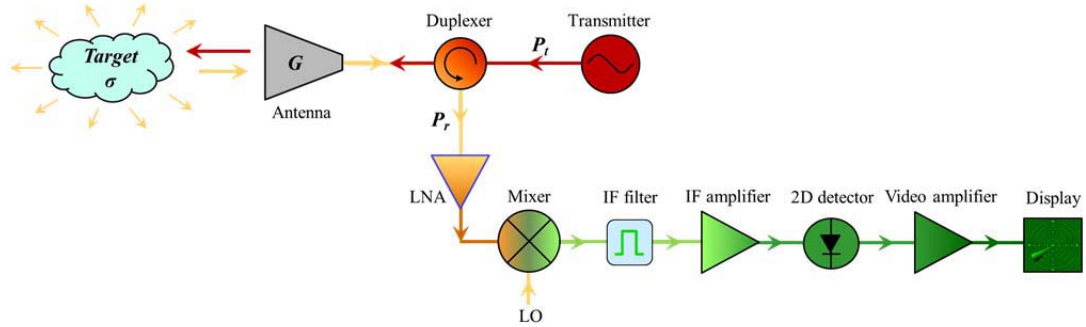


Figure 1.5. Block diagram of a basic monostatic radar system [11].

mechanism of a basic monostatic radar system is illustrated in Figure 1.5. The transmitted signal is reflected back from a distant object, and captured at the same location. The received power can be described in the following formula [20]:

$$P_r = \frac{P_t G^2 \lambda^2 \sigma}{(4\pi)^3 R^4}, \quad (1.2)$$

where G is the antenna gain, λ is the wavelength in free space, R is the distance between the transmitter and receiver, P_t is the transmit power, and σ is the radar cross section (RCS) of the target. RCS is defined as the ratio of the scattered power in a given direction to the incident power density and is a property of the target itself depending on the frequency, polarization, and incident/reflected angles. In the receiver, the signals captured by the antenna will be amplified, down-converted to an intermediate frequency (IF), filtered, and detected for imaging.

Conventional radar systems generally have operated at frequencies extending from about 220 MHz to 35 GHz, a spread of more than seven octaves. Interest in W -

band frequencies stems from the distinct characteristics exhibited by radar at these frequencies, i.e., large bandwidth, small antenna size, and short wavelength, as well as avoiding crowded low frequencies. Large bandwidth means high range-resolution, and can reduce the likelihood of mutual interference between equipment, which introduces vulnerabilities in electronic countermeasures [20]. Small antennas and short wavelengths allow narrow beamwidths for high directivity with physically small apertures. Narrow beamwidths are important for high-resolution imaging radar and to avoid multipath effects when tracking low-altitude targets. Also, short wavelengths can offer high accuracy for the velocity measurement of Doppler radars, and makes it possible to explore the targets whose dimensions are electrically ‘large’ at W-band and ‘small’ at microwave frequencies. The above mentioned attributes of W-band frequencies suggest potential applications in low-angle tracking, interference-free radar, electronic counter-countermeasures (ECCM), cloud-physics radar, high-resolution radar, fuses, and missile guidance.

1.3.3 Radiometry Systems

A radar system detects a distant target by transmitting a signal and receiving its echo from the target and, thus, can be described as an active sensing system. In contrast, radiometry is a passive technique that captures information of a target solely from its blackbody radiation (noise). Any object in thermodynamic equilibrium at a temperature, T , radiates energy according to *Planck’s radiation law*. In the microwave and millimeter wave region the radiated power is [11]:

$$P = kTB, \tag{1.3}$$

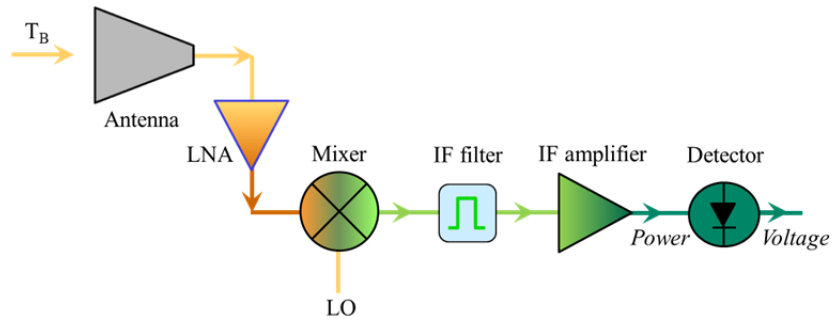


Figure 1.6. Block diagram of a basic microwave radiometer [11].

where k is *Boltzmann's constant*, B is the system bandwidth, and T is the temperature in degrees kelvin. This result strictly applies only to a blackbody, which is defined as an idealized material that absorbs all incident energy and reflects none. A non-ideal blackbody will partially reflect incident energy, thereby radiating less power than an ideal blackbody at the same temperature. Thus, for radiometric purpose, a brightness temperature, T_B , should be defined as follows:

$$T_B = eT, \quad (1.4)$$

where T is the physical temperature of the body, and e is the emissivity of the body, representing the ratio of the power radiated by a body to that radiated by a perfect blackbody at the same temperature. The objective of radiometry is to infer information about the scene from the measured brightness temperature and an analysis of the radiometric mechanism that relates the brightness temperature to physical conditions of the scene.

The block diagram of a basic radiometer is illustrated in Figure 1.6. Blackbody radiation is omnidirectional and, therefore, the power captured by the receiving antenna can be described as

$$P_r = \frac{G \lambda^2}{(4\pi R)^2} P_B, \quad (1.5)$$

where G is the receiving antenna gain, λ is the wavelength in free space, R is the distance between the target and receiver, and P_B is the blackbody radiation power of the target. The front-end unit of the receiver of a radiometer is similar to that of wireless communication and radar systems, consisting an antenna to capture signal, a low noise amplifier (LNA) as a preamplifier, a down-conversion unit, and an IF stage.

Microwave radiometry has been developed over the last thirty years into a mature technology, which is strongly interdisciplinary and includes electrical engineering, oceanography, geophysics, atmospheric and space sciences and so on [11]. Its applications include mapping, surveillance, astronomy, target detection and recognition, and profile of temperature, moisture, and humidity. To achieve high resolution and reduce system size and weight, W -band frequencies have been investigated for advanced radiometers [21]. Similar to radar systems, W -band frequencies can provide large bandwidth, small antenna size, and shorter wavelengths to radiometers. According to Equation (1.3), larger bandwidth means stronger radiated power for a black body. For a given aperture size, shorter wavelengths and small antennas allow narrow beamwidths for high directivity within a physically small profile, thus increasing the resolution.

1.4 W-band Front-End Receiving Module in Multilayer LCP Substrates

In the previous section, three important RF systems, namely, wireless communication, radar, and radiometry, and their applications at *W*-band have been discussed. These three systems have many discrepancies in their system topologies, mechanisms, and applications. However, it should be noted that the front-end unit of their receivers are similar, as can be seen in Figures 1.4, 1.5, and 1.6, where the desired signals are all captured using antennas, pre-amplified using LNAs, and selected using filters. To cover a large dynamic range with high power, high gain antennas are necessary in the receivers. To reduce the receivers' noise figure, low noise amplifiers are typically integrated after the receiving antennas to improve the signal-to-noise ratio (SNR). Filters are utilized to obtain the spectra of interest and employed virtually in all wireless systems. These components all have the same function in the various receivers and can be integrated together as a front-end receiving module, which could potentially be utilized in various wireless systems.

1.4.1 State-of-The-Art

To reduce the unit price and manufacturing cycle for large quantity production, the proposed front-end receiving modules are fabricated using commercial state-of-the-art large-panel circuit print technologies [9]. LCP is chosen as the PCB substrate due to its unique advantages discussed in Section 1.2.1. To achieve broad bandwidth for wireless communications, the antenna and transitions in the front-end receiving module are designed with an ultra-wide bandwidth spanning the *W*-band frequencies. A state-of-the-art high-gain wideband LNA, Northrop Grumman ALP283, is chosen as the pre-amplifier to minimize the noise figure and improve SNR. Filters and directional filters are also developed as options for narrowband applications. To

achieve sufficient net gain for the three wireless applications, a multi-chip module with cascaded LNAs is proposed. To minimize the EMI induced by the high gain in a compact module at high frequencies, shielding structures, i.e., via barriers and substrate integrated waveguides, are designed and distributed in the LCP substrates and a metallic housing is designed to isolate the LNAs in air. To reduce the size, weight, and power consumption (SWaP), the front-end module is designed on multilayer circuits, whose detailed advantages will be addressed in the following subsection.

1.4.2 Multilayer Circuitry

A multilayer circuit comprises two or more core layers that are stacked together with bond-ply layers and reliable predefined mutual connection between them. Typically, the core layers with metal claddings are utilized to pattern the circuits, and the bond-ply layers are utilized for lamination. To date, multilayer circuits have been widely used in various applications, particularly in the high-end military and aerospace electronic equipment. As can be seen in Fig. 1.3 (a), multilayer circuits occupy more than 50% of the PCB market in 2010. As electronic devices become smaller, the single-sided and double-sided PCBs cannot satisfy the increasing assembly density due to their limited available space. Also, they are not suitable to avoid parallel lines, minimize signal line length, and shield sensitive devices due to the limited intersections that can be achieved. Under the demand of large number of interconnections and crosses, multilayer circuits are developed to achieve a satisfactory performance. Compared to the traditional single-sided and double-sided circuits, multilayer circuits can provide numerous advantages, i.e., high assembly

density, compact size, light weight, low interconnection loss, reliability, flexibility, high-speed, multi-function, and layer-to-layer electrical isolation.

1.5 Dissertation Outline

In this dissertation I present my research on the development of a front-end receiving module based on multilayer LCP substrates at *W*-band, consisting of passive components, i.e., antennas, filters, transmission lines, and transitions, and active components, i.e., LNAs and their integration with printed circuits. The detailed discussion of these components is organized as follows:

In Chapter 2, I present a high gain linearly tapered antipodal slot antenna (LTASA) on a thin film liquid crystal polymer substrate for the applications of wireless receivers at *E*- and *W*-bands. This chapter begins with the system aspects of the receiving antennas in Section 2.1 and the challenges of antennas at *W*-band discussed in Section 2.2. The design and measurement of the proposed LTASA and an optically-addressed antenna far-field measurement system is discussed in detail in Section 2.3. The proposed LTASA achieves an ultra-wide band (UWB) of operation from 47 to 110 GHz, a gain of 17 ± 0.5 dBi, narrow beamwidth, low side lobes, and low cross-polarization.

In Chapter 3, four ultra-wideband transitions in multilayer LCP substrates are presented, namely, conductor-backed coplanar waveguide (CBCPW)-to-stripline vertical transition, microstrip (MS) line-to-substrate integrated waveguide (SIW) transition, SIW-to-rectangular waveguide transition, and MS-to-coplanar waveguide (CPW) transition. In Section 3.1, I discuss the circuit components potentially desired for interconnection and integration in the front-end receiving module. Then, these four

transitions are presented individually from Section 3.2 to Section 3.5. The proposed four transitions achieve low loss, low reflection, and ultra-wide bandwidth at W -band.

In Chapter 4, I present the integration and packaging technologies for multi-chip modules and a 50dB gain double-LNA module in multilayer LCP substrates at W -band. First, the utilized state-of-the-art W -band LNA is described in Section 4.1. Then, the topology of the multilayer LCP carrier and V-shape low profile wire bonding are depicted in Section 4.2 and Section 4.3, respectively. In Section 4.4, the double-LNA module and its package are presented. The proposed double-LNA module achieves a gain of more than 46.5 dB and a noise figure of less than 6 dB from 80 to 100 GHz.

In Chapter 5, a SIW-based filter and a MS line-based directional filter in multilayer LCP substrates at 95 GHz are presented. In the beginning of this chapter, I discuss the challenges for filter design and fabrication at W -band. Then, the SIW filter and directional filter are depicted in detail in Section 5.2 and Section 5.3, respectively. The former has an insertion loss of 1.5 dB at 95 GHz and a 3dB bandwidth from 90.8 GHz to 98.5 GHz, and the latter achieves an insertion loss of 3 dB at 96 GHz and a 3dB bandwidth of 8% centered at 96 GHz.

In Chapter 6, I summarize this dissertation and discuss the future direction of my research.

1.6 List of Original Contributions

Most of my research as a Ph.D. student in the Department of Electrical and Computer Engineering at University of Delaware are presented in this dissertation. Here, I list the original contributions of my work as follows:

- A linearly tapered antipodal slot antenna at E - and W -bands was proposed and demonstrated with high gain, ultra-wide bandwidth, narrow beamwidth, low

side lobes, and low cross-polarization. To characterize the gain and radiation patterns of the proposed antenna, an optically-addressed antenna far field measurement system was proposed and constructed;

- A novel ultra-wideband conductor-backed coplanar waveguide-to-stripline vertical transition was proposed and demonstrated in multilayer liquid crystal polymer substrates. The transition achieves low insertion loss and low reflection from DC to 80 GHz;
- A novel ultra-wideband substrate integrated waveguide-to-rectangular waveguide transition in multilayer liquid crystal polymer substrates was proposed and demonstrated at *W*-band. The proposed transition avoids using guided vias, eliminates the potential substrate mode, and addresses low insertion loss from 70 to 110 GHz;
- Integration and packaging technologies of high-gain multi-chip module were developed in multilayer liquid crystal polymer substrates at *W*-band. A novel double-LNA module was integrated and packaged on a four-layer liquid crystal polymer carrier, achieving a net gain of higher than 46.5 dB and a noise figure of less than 6 dB from 75 to 100 GHz;
- A substrate integrated waveguide filter at 95 GHz was proposed and characterized to demonstrate its application possibility in commercial large-scale printed circuitry at *W*-band;
- A microstrip line-based directional coupler and directional filters are proposed and demonstrated in multilayer liquid crystal polymer substrates at 95 GHz. The proposed filters comprise the invented dual-slot directional couplers and

two-wavelength loop resonators. This is the first time that directional filter was demonstrated at *W*-band;

- A high-gain low-noise figure front-end receiving module for passive millimeter wave imaging was proposed and demonstrated at 96 GHz. The receiving module achieves a net gain of 62 dB, a 3dB bandwidth of 4 GHz centered at 96 GHz, and a low noise figure of less than 6 dB;
- A 4×4 phased patch array antenna integrated with a Piezoelectric transducer-controlled phase shifter was proposed and demonstrated at *Ka*-band. The antenna achieves a bandwidth of 23% centered at 35 GHz, and a continuous true-time delay beam steering in a large angle of 33°. This work is not presented in this dissertation.

Most of the contributions were published in peer-reviewed journals and/or presented at conferences. The directional filter has been submitted as a provisional patent disclosure. The following is a list of my publications.

Journals:

1. **Y. Zhang**, S. Shi, R. D. Martin, and D. W. Prather, “Ultra-wideband CBCPW to stripline vertical transition in multilayer LCP substrates,” *Microwave and Optical Technology Letters*, vol. 57, no. 6, pp. 1481-1484, Jun. 2015.
2. **Y. Zhang**, S. Shi, R. D. Martin, and D. W. Prather, “Substrate integrated waveguide filter on LCP substrate at 94 GHz,” *Microwave and Optical Technology Letters*, vol. 58, no. 3, pp. 577-580, Mar. 2016.
3. **Y. Zhang**, J. Bai, S. Shi, and D. W. Prather, “Ka-band phased patch array antenna integrated with a PET-controlled phase shifter,” *International Journal*

of RF and Microwave Computer-Aided Engineering, vol. 26, no. 3, pp. 199-208, Mar. 2016.

4. **Y. Zhang**, S. Shi, R. D. Martin, and D. W. Prather, "High-gain linearly tapered antipodal slot antenna on LCP substrate at E- and W-bands," *IEEE Antennas and Wireless Propagation Letters*, accepted in Nov. 2015.
5. **Y. Zhang**, S. Shi, R. D. Martin, and D. W. Prather, "Slot-coupled directional filters in multilayer LCP substrates at 95 GHz," (in review).
6. **Y. Zhang**, S. Shi, R. D. Martin, A. A. Wright, P. Yao, K. Shreve, C. Harrity, and D. W. Prather, "Packaging of high-gain multi-chip module in multilayer LCP substrates at W-band," (in review).
7. **Y. Zhang**, S. Shi, R. D. Martin, and D. W. Prather, "Broadband SIW-to-waveguide transition in multilayer LCP substrates at W-band," (in review).
8. J. Bai, S. Shi, G. Schneider, J. Wilson, **Y. Zhang**, W. Pan, and D. Prather, "Optically driven ultrawideband phased array with an optical interleaving feed network," *IEEE Antennas and Wireless Propagation Letters*, vol. 13, pp. 47-50, Jan. 2014.
9. S. Shi, J. Bai, G. J. Schneider, **Y. Zhang**, R. Nelson, J. Wilson, C. Schuetz, D. W. Grund, and D. W. Prather, "Conformal wideband optically addressed transmitting phased array with photonic receiver," *Journal of Lightwave Technology*, vol. 32, no. 20, pp. 3468-3477, Oct. 2014.
10. S. Shi, J. Bai, R. Nelson, C. Schuetz, Peng, Yao, G. Schneider, **Y. Zhang**, and D. W. Prather, "Ultrawideband optically fed tightly coupled phased array," *Journal of Lightwave Technology*, vol. 33, no. 23, pp. 4781-4790, Dec. 2015.

Conferences:

1. **Y. Zhang**, S. Shi, R. D. Martin, P. Yao, K. Shreve, and D. W. Prather, "Multilayer liquid crystal polymer based RF front-end module for millimeter wave imaging," *Antennas and Propagation Society International Symposium (APSURSI), 2014 IEEE*, pp. 1700-1701, Jul. 2014.
2. **Y. Zhang**, S. Shi, R. D. Martin, and D. W. Prather, "Vertical transitions between transmission lines and waveguides in multilayer liquid crystal polymer (LCP) substrate," *Proc. SPIE 8985, Terahertz, RF, Millimeter, and Submillimeter-Wave Technology and Applications VII, 898514*, Mar. 2014.
3. **Y. Zhang**, S. Shi, and D. W. Prather, "Slot-coupled waveguide-to-microstrip transition and waveguide-fed patch antenna at E-band," *Antennas and Propagation Society International Symposium (APSURSI), 2013 IEEE*, pp. 1858-1859, Jul. 2013.
4. **Y. Zhang**, J. Bai, S. Shi, and D. W. Prather, "Ka-band phased patch antenna array," *Antennas and Propagation Society International Symposium (APSURSI), 2012 IEEE*, pp. 1-2, Jul. 2012.
5. **Y. Zhang**, J. Bai, S. Shi, J. Macario, G. J. Schneider, J. Murakowski, and D. W. Prather, "Ka-band patch antenna array integrated with an optical feed network," *SAMPE 2012*, May 2012.
6. R. D. Martin, S. Shi, **Y. Zhang**, A. Wright, et al., "Video rate passive millimeter-wave imager utilizing optical upconversion with improved size, weight, and power," *Proc. SPIE 9462, Passive and Active Millimeter-Wave Imaging XVIII, 946209*, May 2015.
7. S. Shi, J. Bai, G. Schneider, **Y. Zhang**, and D. Prather, "Ultra-wideband optically addressed transmitting phased array," in *Antennas and Propagation*

Society International Symposium (APSURSI), 2013 IEEE, pp. 2237–2238, 2013.

8. S. Shi, J. Bai, G. Schneider, **Y. Zhang**, R. Nelson, J. Wilson, C. Schuetz, and D. Prather, “Conformal ultra-wideband optically addressed transmitting phased array and photonic receiver systems,” *Microwave Photonics (MWP), 2013 International Topical Meeting on*, pp. 221-224, Oct. 2013.
9. A. Wright, R. Martin, F. Kiamilev, J. Bai, K. Shreve, A. Mercante, **Y. Zhang**, et al., “95 GHz SiGe LNA for sparse aperture mmW imaging,” *GOMACTech 2015*, Mar. 2015.

Patent:

Y. Zhang, S. Shi, R. D. Martin, and D. W. Prather, Slot-Coupled Directional Coupler and Filters in Multilayer Substrates, filed as a provisional patent in Sep. 2015.

Chapter 2

HIGH-GAIN LINEARLY TAPERED ANTIPODAL SLOT ANTENNA AT E- AND W-BANDS

An antenna is a transitional structure between free space and a feed device, e.g., transmission lines and waveguides, converting electric power to propagating electromagnetic waves in the transmitter, and vice-versa in the receiver. The origin of the word ‘antenna’ relative to wireless apparatus is an Italian word for ‘pole’ first used by radio pioneer Guglielmo Marconi [22]. Since Marconi demonstrated the first antenna in 1895, thousands of antennas have been designed and utilized for the wireless applications at radio frequencies.

2.1 System Aspects of Receiving Antennas

In wireless systems, i.e., wireless communication, radar, and radiometry, the antenna is a necessary component. A properly designed antenna can relax system requirements and improve overall system performance. Antennas are inherently bidirectional, in that they can be utilized for both transmitting and receiving functions. In the remainder of this section I describe some of the basic characteristics of antennas that will be needed for the study of receivers in wireless systems.

In a general sense, the receiver is one of the most critical parts in a wireless system. On the system level, the performance of a receiver can be described using some common factors:

- Dynamic range: the amplitude ratio of the strongest and weakest signals that the receiver can decode.

- Bandwidth: the spectral region where the receiver can operate.
- Sensitivity: the minimum amplitude of the incoming RF signal that the receiver can decode, under the conditions of the required SNR.
- Selectivity: the minimum separation between the desired carrier frequency and its first neighboring frequency, under the condition that the receiver can safely receive the intended signal.

The first three factors are closely related to the receiving antennas' characteristics, i.e., gain, bandwidth, and radiation efficiency as well as feed loss, while selectivity is a factor determined by filters, whose design and measurement will be discussed in Chapter 5.

The gain of an antenna is traditionally defined as “the ratio of the intensity, in a given direction, to the radiation intensity that would be obtained if the power accepted by the antenna was radiated isotropically. The radiation intensity corresponding to the isotropically radiated power is equal to the power accepted by the antenna divided by 4π [22].” According to Equations (1.1), (1.2), and (1.5), the gain of a receiving antenna directly determines the received power and operating range of a wireless system. Typically, to capture more power, high gain antennas, such as travelling wave antennas and array antennas, are preferable in some receive modules for wireless systems.

The bandwidth of an antenna is the spectral range where the performance of the antenna, with respect to some characteristics, conforms to a specified standard. Typically, it is referred to as impedance bandwidth, which is related to the input impedance of an antenna and the corresponding reflection. Wide bandwidth can provide many advantages for wireless applications. For instance, in wireless

communication systems broader bandwidth means more data capability and, consequently, higher data transmission rates. Also, large bandwidth can provide high range resolution for radar systems. In this regard, receive antennas with wide bandwidth are of great interest in many wireless systems.

Typically, the system sensitivity is described using SNR, and the noise is quantified using noise figure (NF). To minimize the NF of a receiver, a LNA should be integrated after the receiving antenna as a pre-amplifier. In a practical module, the dissipative loss of the receiving antenna and the insertion loss from the LNA to the antenna feed are added to the receiver's NF. In this case, the receiving antenna should be designed with a high radiation efficiency and a low feed loss.

2.2 Challenges for W-band Antennas

In Section 1.2, the challenges in material, fabrication, electromagnetic interference, and measurement for *W*-band applications have been discussed from a more general perspectives. In this section, I describe the challenges for *W*-band antenna design and measurement in detail.

2.2.1 Design Aspect

As presented in Section 1.4, LCP is chosen as the substrate for the proposed receiver module. The loss tangent of LCP is approximately 0.0045 at *W*-band, which is two times larger than that at low frequencies, i.e., 35 GHz. However, the dielectric loss of LCP is still much smaller than most other materials at *W*-band. Another benefit of LCP is commercially available thicknesses down to 25 μm , 50 μm , and 100 μm [23], which are preferable for high-frequency applications. However, thin substrates significantly increase the propagation loss of many transmission lines, such as

microstrip lines and CBCPWs. Also, it may introduce challenges for the design of some antennas. For instance, patch antennas and SIW-based slot antennas prefer thick substrates to achieve large bandwidth and high radiation efficiency. To mitigate these issues, a 100 μm thick LCP is selected as the substrate for the module components. Using this substrate, the signal line width of the 50 Ω microstrip lines and CBCPWs is a few hundred micrometers, which is electrically ‘small’ at microwave frequencies. However, at *W*-band, the thickness of the selected LCP substrate and signal line width of the corresponding transmission lines becomes electrically ‘large’ in terms of wavelength, which may introduce parasitic modes and asymmetry to some antennas and arrays, i.e., patch antenna and tapered slot antenna.

In addition, the *W*-band antennas with small features are sensitive to fabrication and manufacturing tolerance. Thus, tolerance analysis and fabrication compensation have to be considered in the design of these antennas.

2.2.2 Measurement Aspect

In the antenna measurement, the impedance bandwidth can be characterized using a network analyzer and the far field properties can be validated using antenna far-field or near-field measurements. As the name implies, the far-field measurement means characterizing the antenna under test (AUT) in its far-field region, and the near-field measurement is to characterize the AUT in its near field region and compute its corresponding far-field radiation using a Fourier Transform, namely stationary phase to the Laplace transform [22]. Typically, the latter is suggested for the antennas’ measurement at high frequencies, but comes at an increased cost.

Generally, at *W*-band, WR-10 rectangular waveguides are employed for connection, and G-S-G probes are utilized to feed the DUTs. However, these

waveguides and probes may not be suitable for the measurement of an antenna's far-field properties. In antenna far-field measurement, either the transmitting antenna or receiving antenna has to be rotated in a large angular range to obtain comprehensive field data. However, *W*-band probes are easily broken during the rotation, and the waveguides are rigid and cannot be bent. In this case, a specially-designed transition may be desired to connect the AUT to waveguide and flexible, yet lossy, coaxial lines and additional coaxial line-to-waveguide transitions have to be utilized to make the antenna rotation easier. As a result, amplifiers may be used to pre-compensate for the loss of coaxial lines and transitions and make the received power measurable, consequently increasing both the cost and complexity of the measurement system. Also, the measurement of *W*-band antennas is sensitive to the metallic rotation stage, waveguide, and holding structures as well as rotation tolerance. To this end, low-profile accurate rotation stages and RF absorbers are required, further increasing the cost of the measurement system.

2.3 Linearly Tapered Antipodal Slot Antenna

In *W*-band wireless systems, i.e., local area networks, metropolitan links, satellite communication, vehicle collision avoidance radar, and high-definition imaging [24]-[25], one of the most critical components is UWB, high gain, light weight, and low cost antennas. Unfortunately, not many antennas can provide both high gain and an ultra-wide band spanning for both the *E*- and *W*-bands. Among these antennas, tapered slot antenna (TSA) is a promising candidate due to its tunable gain, planar profile, light weight, low cost, and versatile feeds [26]. Typically, the bandwidth of a TSA is limited by the bandwidth of the transition from the antenna feed to the flared slot-line. In practical systems, the TSA may require MS line or co-

planar waveguide (CPW) as a feed, to integrate with power amplifiers (PAs) or LNAs. However, conventional MS-to-slot-line [27] and CPW-to-slot-line [19] baluns have a limited bandwidth of less than 1.3:1. A SIW, as a balanced structure, can be utilized to feed the TSA directly. However, the maximum bandwidth of a SIW-fed TSA is less than 2:1 due to the second-order guided mode of the waveguide [28]-[29].

It is noted that most of the TSAs reported so far operate below *Ka*-band [26]-[30], which is mainly limited by the availability of the substrate and antenna far-field measurement system. On one hand, due to the TSAs' asymmetry, a thin substrate is desired to minimize cross-polarization and maintain symmetric radiation patterns. However, most available substrates become electrically 'thick' in terms of wavelength at *E*- and *W*-bands. Typically, the transmission lines and waveguides on a thinner substrate address higher propagation loss [8]. Thus, the utilized thin substrate should have low loss tangent at high frequencies, e.g., *W*-band. Also, to reduce the discontinuity between the substrate and air, low dielectric constant substrates are preferable for TSAs. On the other hand, it is challenging to characterize the far-field of the antennas at high frequencies, i.e., *E*- and *W*-bands. The traditional high-frequency, far-field or near-field measurement system utilizes a frequency multiplier (mmW head) for the RF source, rigid waveguides for connection, and flexible coaxial lines for the rotated antennas. However, the multiplier is heavy and bulky, the waveguides are cumbersome and unbendable, and the coaxial lines are lossy at *W*-band [31], thereby introducing significant difficulties for the measurement system set-up.

In this section, I present a linearly tapered antipodal slot antenna (LTASA) on a thin film LCP substrate at *E*- and *W*-bands that was fabricated on a 12×18 inch LCP panel using state-of-the-art commercial large-panel PCB technologies. The proposed

LTASA achieves an ultra-wide bandwidth and impressive far-field properties, i.e., high gain, nearly symmetric narrow beamwidth, high radiation efficiency, low side lobes, and low cross-polarization.

2.3.1 LTASA Design

A tapered slot antenna is a class of end-fire radiating directional travelling-wave antennas, whose design principles have already been thoroughly investigated. According to Ref. [26], when the aperture size of any TSA becomes on the order of a half-wavelength in free space, it no longer acts as a broad-band travelling-wave antenna. Thus, the opening width of the flared antipodal slot-line (ASL) should be

$$W_0 \geq \lambda_0/2. \quad (2.1)$$

To minimize the TSA's asymmetry, the effective thickness of the antenna substrate is suggested to be:

$$0.005 < T_{eff} = (\sqrt{\epsilon_r} - 1)t/\lambda_0 < 0.03, \quad (2.2)$$

where λ_0 is the wavelength in free space, t and ϵ_r are the thickness and dielectric constant of the antenna substrate, respectively.

The dielectric constant of LCP is approximately 3 and 3.2 at 60 GHz and 110 GHz, respectively. According to Equation (2.2), to design a TSA with its band covering E - and W -bands, the ideal LCP thickness is $33 \mu\text{m} < t < 100 \mu\text{m}$. To minimize the loss of the feed transmission line, Rogers LCP, Ultralam3850, with a thickness of $100 \mu\text{m}$ is chosen as the antenna substrate. With such a thin substrate, the cross-polarization can be efficiently suppressed.

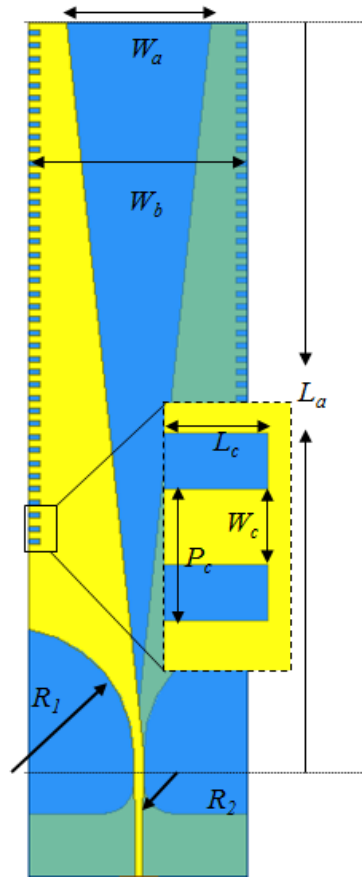


Figure 2.1. Configuration of the proposed linearly tapered antipodal slot antenna.

Ansys High Frequency Structural Simulator (HFSS) was utilized to design and optimize the proposed LTASA, whose configuration is illustrated in Figure 2.1. The antenna comprises a MS line feed, a MS-to-antipodal parallel stripline (APSL) balun, a linearly flared ASL, and periodic corrugations at the outer edges of the ASL. To achieve 50Ω impedance, the width of the MS line and APSL is 240 and 320 μm , respectively. The MS-to-APSL balun reported in Ref. [30] was utilized on LCP

Table 2.1. Optimized dimensions of the proposed LTASA.

Parameters	Dimensions (mm)
L_a	23.5
W_a	5
W_b	7
R_1	3
R_2	1
L_c	0.38
W_c	0.24
P_c	0.42

substrate, and scaled up to E -band to provide an ultra-wide band. The corrugations are designed to further suppress the cross-polarization as well as the backward and side lobes [28] [30]. Table 2.1 lists the optimized dimensions of the proposed LTASA.

The simulated S_{11} of the LTASA is shown in Figure 2.2, and it can be found that the 10dB impedance bandwidth is from 48 to 110 GHz. Figure 2.3 illustrates the simulated radiation patterns of the proposed antenna. Within the operational band, the side lobes are less than -20 and -9 dB in the E- and H-planes, respectively, the backward radiation is lower than -18 dB, and the cross-polarization is less than -15 dB. The simulated gain, 3dB beamwidths in the E- and H-planes, sidelobe, and cross-polarization are listed in Table 2.2. It can be seen that the simulated gain is better than 17 dBi from 75 to 95 GHz, and the beamwidths are approximately symmetric in the E - and H -planes at most of the frequencies. The radiation efficiency of the proposed LTASA is higher than 95% from 70 to 110 GHz.

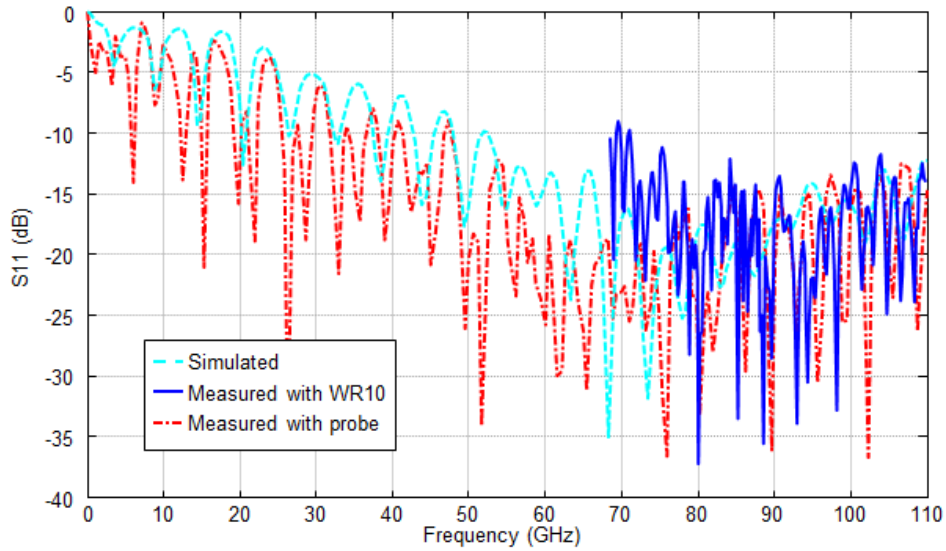


Figure 2.2. Simulated S11 of the LTASA and measured S11 of the LTASAs integrated with a via-less CBCPW probe pad and a MS-to-SIW-to-waveguide transition.

Table 2.2. Simulated gain, beamwidth, first sidelobe, and cross-polarization of the proposed LTASA.

Freq.	Gain	Beamwidth	1st Sidelobe(H)	Cross-Pol.
75 GHz	17.7 dB	$\pm 8.8^\circ(\text{E})/\pm 13.5^\circ(\text{H})$	-11.5 dB	-21.7 dB
80 GHz	17.5 dB	$\pm 9.1^\circ(\text{E})/\pm 13^\circ(\text{H})$	-10.5 dB	-18.3 dB
85 GHz	17 dB	$\pm 9.4^\circ(\text{E})/\pm 12^\circ(\text{H})$	-9.7 dB	-16.7 dB
90 GHz	17.1 dB	$\pm 8.8^\circ(\text{E})/\pm 11.6^\circ(\text{H})$	-9.2 dB	-16 dB
95 GHz	17 dB	$\pm 8.7^\circ(\text{E})/\pm 11.2^\circ(\text{H})$	-8.9 dB	-15.5 dB

Freq. and *Pol.* denote the frequency and polarization, respectively.
E and H denote in the *E*-plane and *H*-plane, respectively.

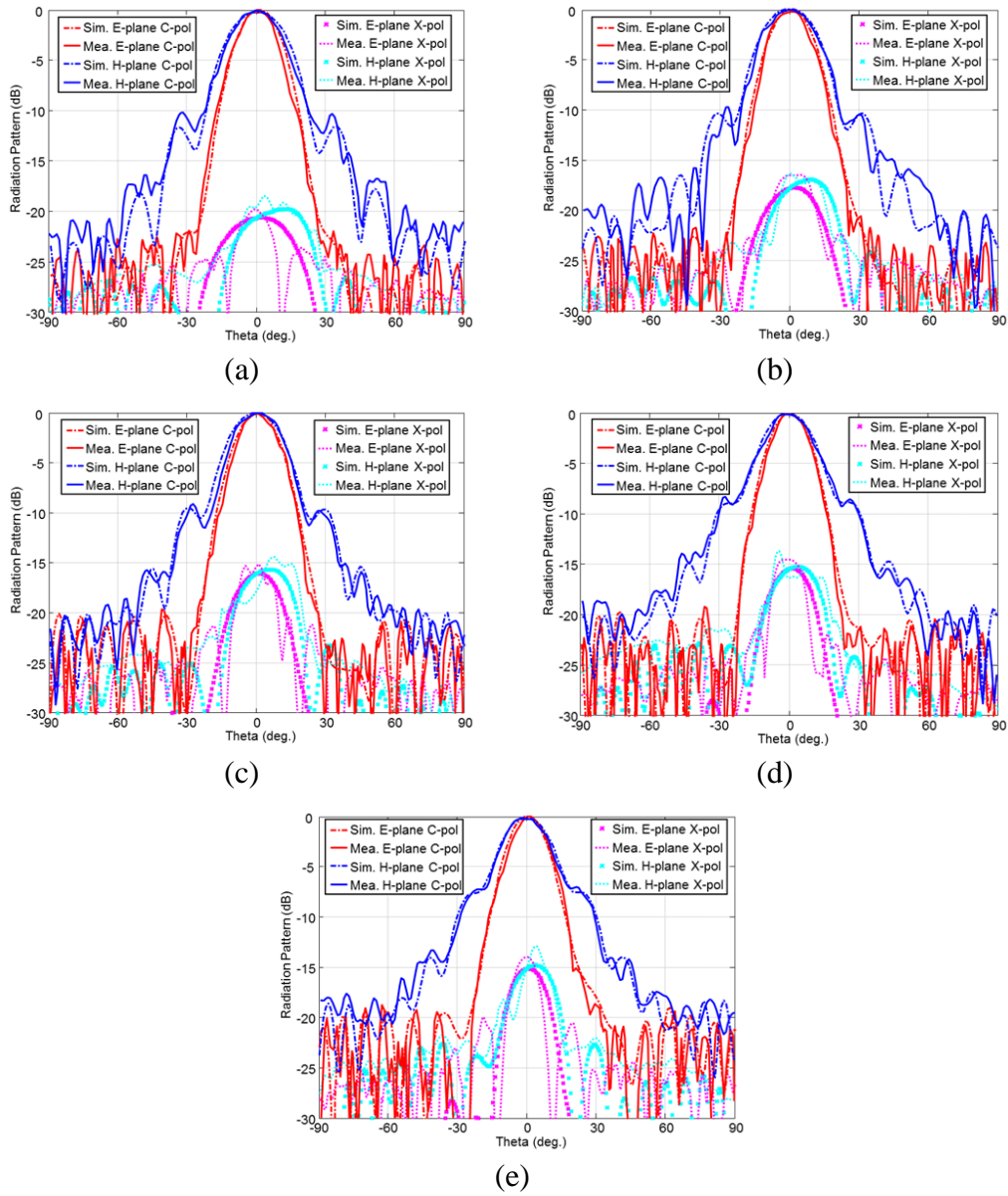


Figure 2.3. Simulated and measured radiation patterns of the LTASA at (a) 75 GHz, (b) 80 GHz, (c) 85 GHz, (d) 90 GHz, and (e) 95 GHz.

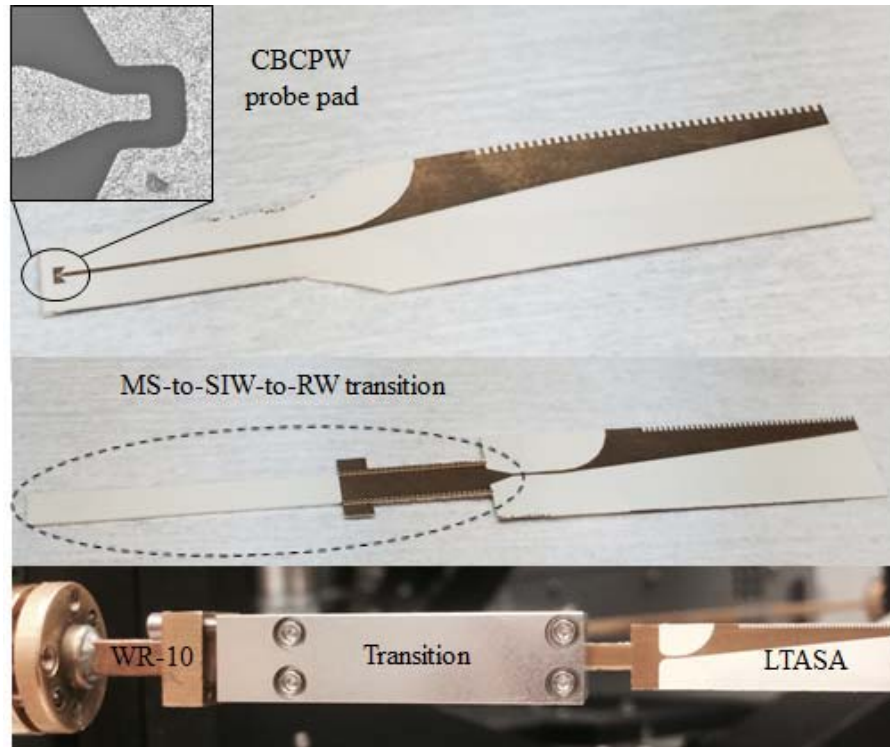


Figure 2.4. Fabricated LTASAs with a via-less CBCPW probe pad and a MS-to-SIW-to-waveguide transition.

2.3.2 Bandwidth Measurement

A G-S-G probe with an impedance of 50Ω was utilized to characterize the LTASA from DC to 110 GHz. To match the G-S-G mode of the probe, the MS feed is terminated with a CBCPW probe pad [32], as shown in Figure 2.4. The termination achieves low loss and low reflection at *E*- and *W*-bands, and its design will be discussed in Section 3.2.2. In our measurement, the probe was calibrated with the short-open-load-through (SOLT) method by using the on-wafer calibration substrate

from GGB Industries Inc. The measured S11 is illustrated in Figure 2.2. An ultra-wide band was demonstrated from 47 to 110 GHz, showing good agreement with simulated data.

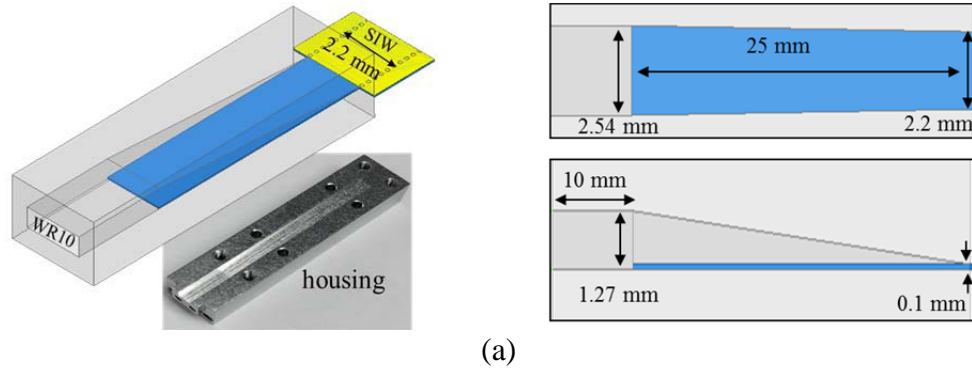
2.3.3 Far-field Measurement

At *W*-band, WR-10 waveguides are typically utilized to connect RF sources to antennas due to their low attenuation. In order to integrate the LTASA with a waveguide, a MS-to-SIW transition and a SIW-to-waveguide transition were designed. The MS-to-SIW transition will be discussed in Section 3.3 of the next chapter. Here, I present the SIW-to-waveguide transition, whose configuration is shown in Figure 2.5 (a). The transition linearly flares a 2.2mm wide SIW to a WR-10 waveguide with a length of 25 mm. The insertion loss of its back-to-back transition is less than 1.6 dB from 70 to 110 GHz, as illustrated in Figure 2.5 (b).

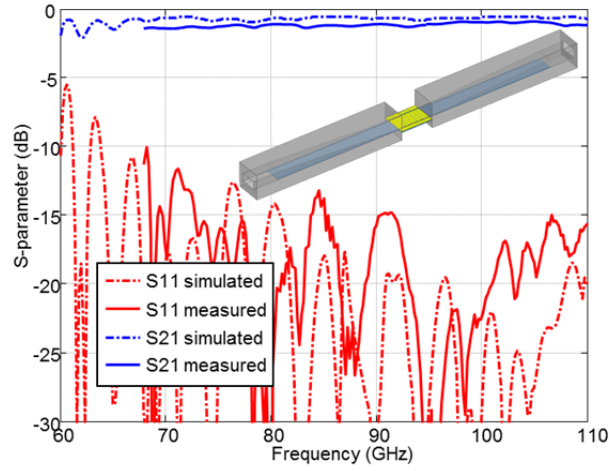
To characterize the antenna far fields, the proposed LTASA is terminated with the aforementioned two transitions, as shown in Figure 2.4. The measured S11 of the WR-10 fed LTASA is less than -12 dB at *W*-band, with the exception of the frequencies near the waveguide's cut-off, as illustrated in Figure 2.2.

2.3.3.1 Optically addressed far-field measurement system

Based on an optical upconversion approach [33], an optically addressed antenna far-field measurement system is developed, whose configuration and mechanism schematic are illustrated in Figure 2.6. Agilent programmable network analyzer (PNA) E8361C integrated with millimeter wave head controller N5260A is utilized as a *W*-band source, providing RF signals to a standard transmitting horn antenna. The AUT is mounted on a rotation stage, and serves as a receiver. The



(a)



(b)

Figure 2.5. (a) Configuration of the SIW-to-waveguide transition, and (b) measured and simulated S-parameters of its back-to-back transition.

received RF signal is amplified, and then upconverted onto an optical carrier by using a high-speed Lithium Niobate (LiNbO_3) electro-optical (EO) phase modulator [34], resulting in an upper and a lower optical sideband around the carrier frequency. The amount of the energy of the sidebands, I_{sb} , can be quantified as [35]:

$$I_{sb} = \eta_{mod} g_{LNA} P_{rf} I_{opt}, \quad (2.3)$$

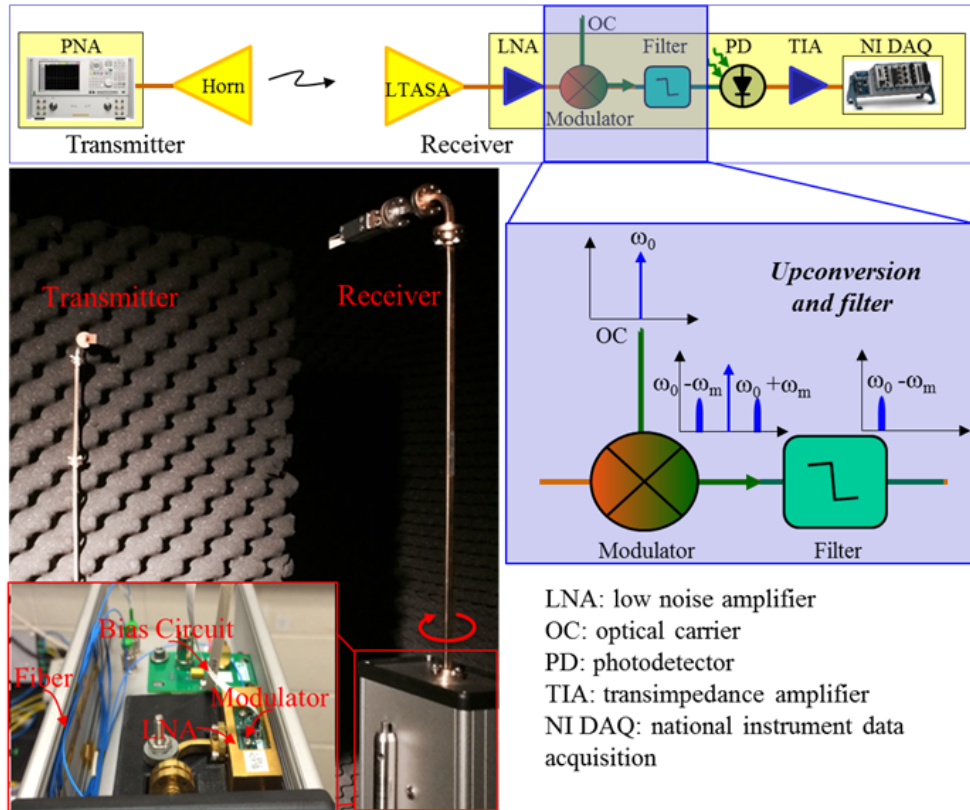


Figure 2.6. Optically addressed far-field measurement system.

where I_{opt} is the optical power into the modulator, P_{rf} is the RF power received at the antenna, g_{LNA} is the gain of the LNA, η_{mod} is the modulation efficiency of the phase modulator.

The modulated signals are routed through optical fibers, which are preferable for the measurement system setup due to their flexibility, low loss, small profile, and light weight. These signals are then fed into a dense wavelength division multiplexing (DWDM) optical filter to pass one of the sidebands while suppressing the carrier

frequency and the other sideband. Next, a square-law detector (photodetector) is used to convert this sideband to a photo-current. The weak current will be amplified using a transimpedance amplifier (TIA). As a result, the voltage generated by the TIA can be derived as [35]:

$$V_{TIA} = g_{TIA} \mathfrak{R}_{PD} \eta_{mod} g_{LNA} P_{rf} I_{opt}, \quad (2.4)$$

where g_{TIA} is the gain of the TIA, and \mathfrak{R}_{PD} is the responsivity of the photodetector. Then, the produced voltage is measured using National Instrument data acquisition (NI DAQ) system.

2.3.3.2 Characterized radiation patterns and gain

Due to the limited bandwidth of the packaged LNA, the far fields of the proposed LTASA were characterized from 75 to 95 GHz. The measured co- and cross-polarized radiation patterns in the E - and H - planes are illustrated in Figure 2.3, which are in good agreement with the simulated results. As the frequency increases from 75 to 95 GHz, the 3dB beamwidth in the E -plane remains approximately $\pm 9^\circ$, and that in the H -plane is reduced from $\pm 13.5^\circ$ to $\pm 11^\circ$. The measured sidelobes are less than -20 and -9 dB in the E - and H -planes, respectively. As the frequency increases from 75 to 95 GHz, the cross-polarization increases from -20 dB to -15 dB, which is due to the increasing substrate thickness in terms of wavelength.

To characterize the AUT's gain, a standard pyramid horn with a gain of 15 dBi was utilized as a reference to replace the LTASA and capture RF power. The insertion losses of the MS-to-SIW and SIW-to-waveguide transitions were calibrated out so that the actual gain of the LTASA could be acquired. The measured gain is higher than

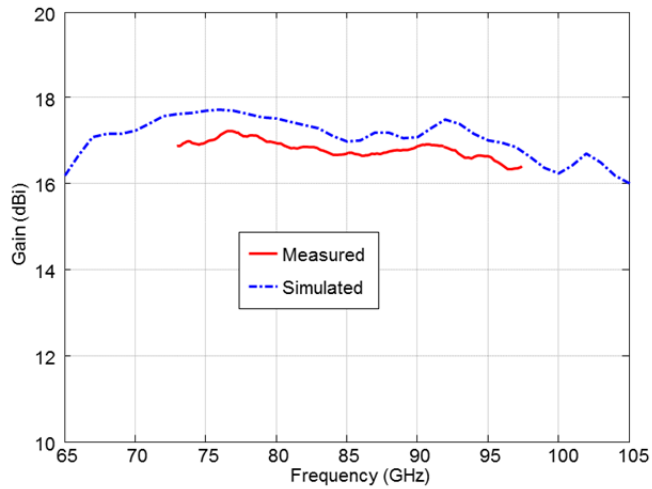


Figure 2.7. Simulated and measured gain spectrum of the proposed LTASA.

16.5 dBi from 73 to 97 GHz, as illustrated in Figure 2.7. The discrepancy between the measured and simulated results may be attributed to the integration tolerance.

2.4 Summary

In this chapter, I first discussed the system requirements for receiving antennas in wireless systems, i.e., wireless communication, radar, and radiometry, and the challenges for antenna design and measurement at *W*-band. Then, an UWB high-gain LTASA on a 100 μ m thick LCP substrate for the *E*- and *W*-bands applications was presented. The 10dB impedance bandwidth of the LTASA was demonstrated from 47 to 110 GHz. A sophisticated optical antenna far-field measurement system, based on an optical upconversion, was developed to characterize the far-field properties of the proposed LTASA. A high gain of 16.5-17.5 dBi, a narrow beamwidth of $\pm 9^\circ$ in the *E*-

plane, and a narrow beamwidth of around $\pm 12^\circ$ in the H -plane were demonstrated from 75 to 95 GHz. The proposed LTASA also achieves low side lobes and low cross-polarization at E - and W -bands, and may have many applications in various wireless systems.

Chapter 3

TRANSITIONS IN MULTILAYER LCP SUBSTRATES

A transition is a passive transforming structure that connects circuit components with different topologies. Its bandwidth determines the system bandwidth, and its insertion loss may impact the system's net gain and noise figure, which are closely related to the dynamic range and sensitivity of a receiver.

3.1 Transmission Lines and Waveguides

Prior to the design of the transitions, the corresponding circuit components and their topologies in the front-end receiving module should be determined. Typically, in multilayer circuits, MS lines and CBCPWs are preferable in the surface layers due to their low propagation loss and shielding ground, while striplines (SLs) and SIWs are more appropriate in the inner layers due to their perfect layer-to-layer electrical shielding. At the input and output interfaces, WR-10 air-filled rectangular waveguides may be utilized for practical applications and measurement, and coplanar waveguides (CPWs) may be desired for probing and integration with CPW-based EO modulators [34]. In the traditional sense, MS lines, CPWs, CBCPWs, SLs, and rectangular waveguides are the classic transmission components, and have been well investigated [10]-[11] [14].

- MS line: a conducting strip separated from a ground plane by a dielectric substrate.
- CPW: a single conducting track printed onto a dielectric substrate, together with a pair of return conductors distributed on both sides of the track.

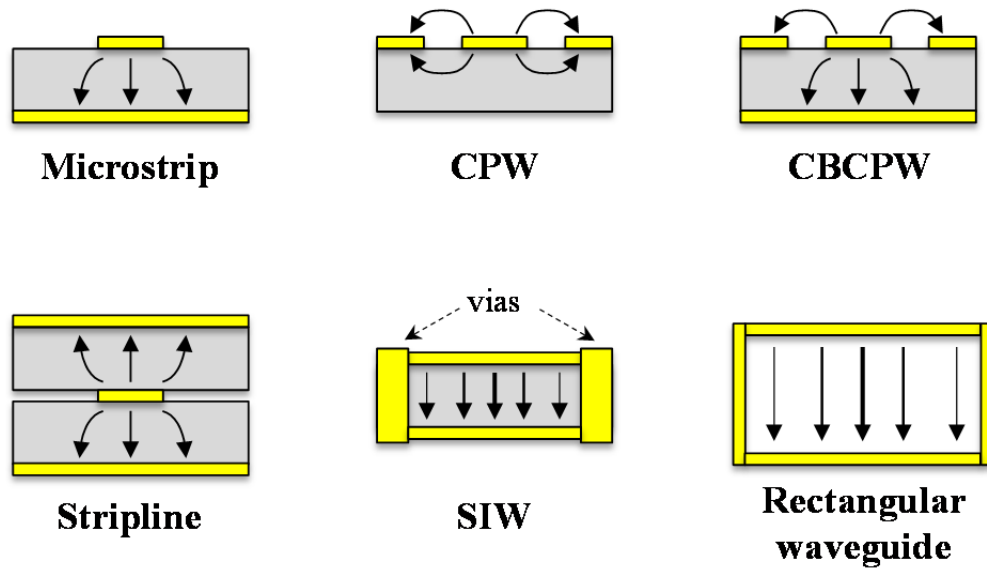


Figure 3.1. Cross-section structure and fundamental mode profile of MS line, CPW, CBCPW, stripline, SIW, and rectangular waveguide.

- CBCPW: a CPW with a ground plane underneath.
- SL: a thin conducting strip sandwiched between two parallel ground planes with dielectric substrates as insulating materials.
- Rectangular waveguide: a metal pipe with a rectangular cross-section.

Recently, SIWs have been developed for printed circuits, which are waveguide-like structures in a dielectric substrate by using two rows of metal vias to connect the top and bottom parallel conductor layers. The cross-section and mode profile of these six transmission components are illustrated in Figure 3.1. It can be seen that MS lines, CPWs, and CBCPWs support quasi-TEM mode, SLs support TEM mode, and SIWs and RWGs support TE_{10} mode.

Table 3.1. Fundamental mode, dimensions, and simulated propagation loss and impedance at W-band of the five planar transmission components on a 100 μm thick LCP substrate and WR-10 rectangular waveguide.

TL	Mode	Dimensions	Loss (dB/cm)	Impedance (Ω)
MS line	Quasi-TEM	246 μm	1-1.5	50
CPW	Quasi-TEM	50 (gap) \times 100(signal) μm	0.9-1.3	66
CBCPW	Quasi-TEM	50 (gap) \times 100(signal) μm	1-1.7	68
Stripline	TEM	60 μm	1.6-2.4	50
SIW	TE ₁₀	1.7 mm (width)	2	23
RWG	TE ₁₀	2.54 \times 1.27 mm	0.05	

TL denotes transmission line.

As discussed in Section 1.4, LCP substrates with a multilayer topology are proposed for the front-end receiving module, which is fabricated using commercial state-of-the-art large-panel circuit print technologies [9]. At W-band, the dielectric constant and loss tangent of LCP substrates are approximately 3.2 and 0.0045, respectively. Thereby, using LCP substrates can minimize the dielectric loss of the transmission lines. In addition, multilayer circuits can provide high density, small size, light weight, and low power consumption for the module as well as symmetric substrates for the SLs and directional filters discussed in Chapter 5. Under the large-panel fabrication standards [9], the minimum resolution of the circuit patterns is 50 μm , and the aspect ratio of the laser-drilled vias is 1.25:1. Table 3.1 lists the fundamental mode, dimensions, and the corresponding propagation loss and impedance at W-band of the five planar transmission components fabricated on a 100 μm thick LCP substrate using the state-of-the-art large-panel circuit print technologies. The MS line and SL have an impedance of 50 Ω , while the CPW and CBCPW have higher impedances close to 70 Ω , which is limited by the fabrication

resolution. The CPW has the minimum propagation loss, while the SIW has the maximum propagation loss. To concurrently compensate for the propagation loss and EMI between circuit components as well as mode and impedance mismatch, MS lines are chosen for interconnection, SIWs and SLs are utilized to purify the guided modes in the substrate, and CBCPWs and CPWs are used for integration and measurement. In the following sections, I will present four ultra-wideband low-loss transitions between these six transmission components for *W*-band applications.

3.2 CBCPW-to-Stripline Vertical Transition

As electronic devices become smaller and lighter, traditional single-sided and double-sided printed circuits cannot satisfy increasing assembly densities due to their limited space. As an alternative, multilayer circuits have received significant attention, which can provide many advantages to RF/microwave circuit designers, i.e., high density, small profile, hybrid integration, multi-function, low interconnection loss, and good electrical shielding [36].

One of the most critical components in a multilayer circuit is the vertical interconnection between different circuit layers. Conventional vertical transitions can be classified in two categories: aperture-coupled transitions [37]-[40] and transitions with vertical micro vias [40]-[42]. The former exhibit a bandpass behavior with a bandwidth of 100% with respect to its center frequency, and the latter can offer a wider bandwidth, but require more sophisticated manufacturing. Most of the vertical transitions reported so far are designed for surface-to-surface connection [37]-[41], which cannot be used for inner-layer applications. Additionally, these reported transitions are designed at low frequencies, i.e., *X*-and *K*-band, and may not be

suitable at *W*-band. Reference [42] reported a transition that is able to operate up to 50 GHz. However, its insertion loss is higher than 3 dB at higher frequencies.

In this section, I present a CBCPW-to-stripline vertical transition in multilayer LCP substrates, which can provide an insertion loss less than 2.5 dB over an ultra-wide band from DC up to 78 GHz.

3.2.1 Transition Design

CBCPWs and SLs are commonly used transmission lines in multilayer RF circuits, due to their superior advantages of good electrical shielding and low loss at high frequencies. The former can be used for probing and external integration, and the latter allows for the design of efficient and compact circuit topologies. As can be seen in Figure 3.1, the CBCPW mode is the combination of a MS line mode and a CPW mode, and the SL mode is a TEM mode. The proposed CBCPW-to-SL transition is designed on two Rogers Ultralam3850 LCP substrates that consist of three metal cladding layers. The thickness of each LCP layer and copper cladding is 50 and 9 μm , respectively. The cross-section and layer-by-layer configuration of the transition are illustrated in Figure 3.2 (a) and (b), respectively. The CBCPW is designed on the top electrode layer, and the SL is sandwiched between the top and bottom LCP layers. To achieve the transition, one blind-via and two through-vias are used to perpendicularly connect the signal lines and grounds of the CBCPW and SL, respectively.

A 3-D finite element method (FEM) based electromagnetic solver, Ansys HFSS, was used to design and optimize the CBCPW-to-SL transition and the following transitions in this chapter. To attain an impedance of 50 Ω , the width of the CBCPW's signal line and gap is designed to be 110 and 70 μm , respectively, and the width of the SL, L_s , is 60 μm . According to the circuit model of a vertical via [43], the

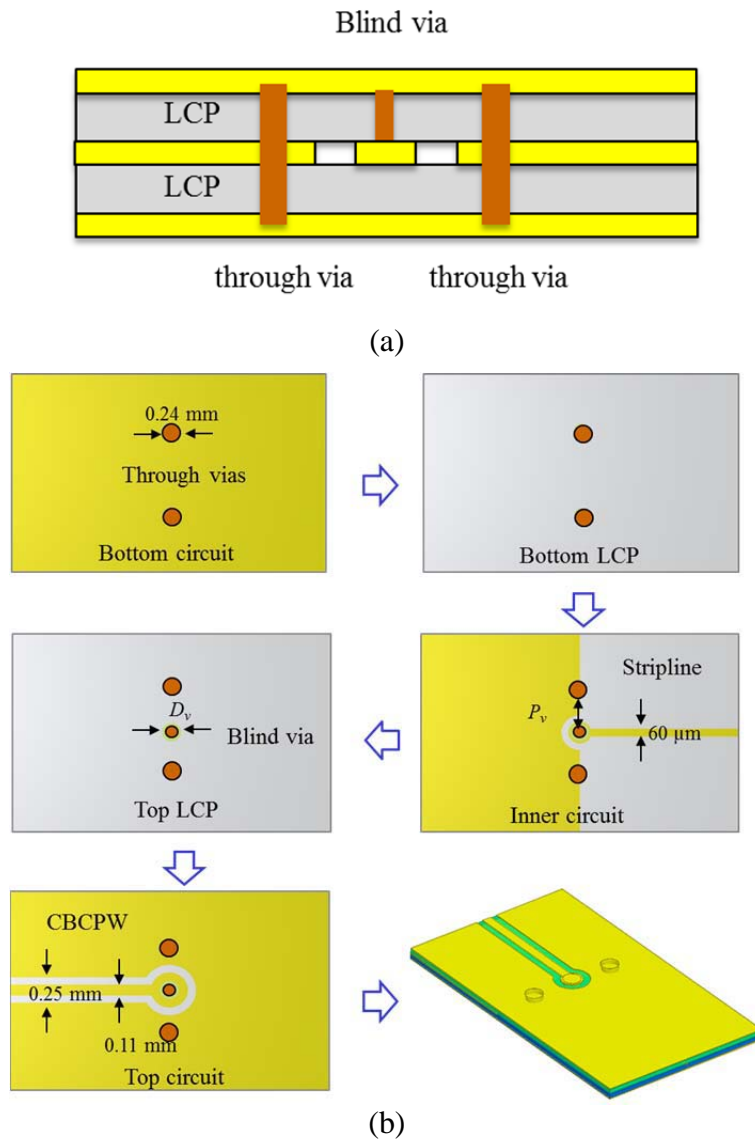


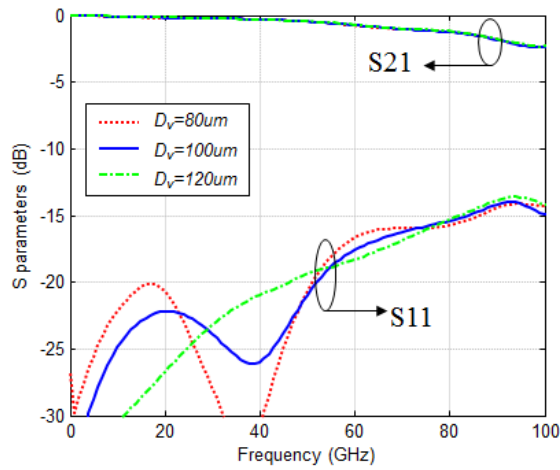
Figure 3.2. (a) Cross section and (b) layer-by-layer configuration and dimensions of the CBCPW-to-SL transition.

parasitic capacitance between the vias barrel and parallel grounds may contribute to parallel-plane evanescent wave. To investigate the impact of the blind via to the performance of the transition, the diameter, D_v , was varied from 80 to 120 μm , and the pitch between the signal and ground vias, P_v , was swept from 0.4 to 0.5 mm. The simulated S-parameters for the tolerance analysis are illustrated in Figure 3.3 (a) and (b). It can be seen that slightly sweeping the diameter and pitch of the vias does not change the transition performance significantly. The insertion loss and reflection become enhanced as the frequency increases, which is due to the fact that the evanescent wave is easier to be excited at high frequencies. A larger blind via could smooth the reflection response, but can also provide higher capacitance at the frequencies over 80 GHz. Also, a larger blind via represents larger ring [9], which could lead to additional impedance mismatch between the vias and transmission lines. As illustrated in Figure 3.3 (b), increasing the pitch between the signal and ground vias can suppress the mutual coupling between the vias, but also increases the insertion loss at high frequencies due to the inductance mismatch. To concurrently optimize the performance of the transition and avoid touching the fabrication limit, the diameter of the signal via is chosen as 100 μm , and the pitch between the signal and ground vias is chosen as 0.5 mm. The diameter of the ground vias is chosen as 240 μm , since they are not dimension-sensitive.

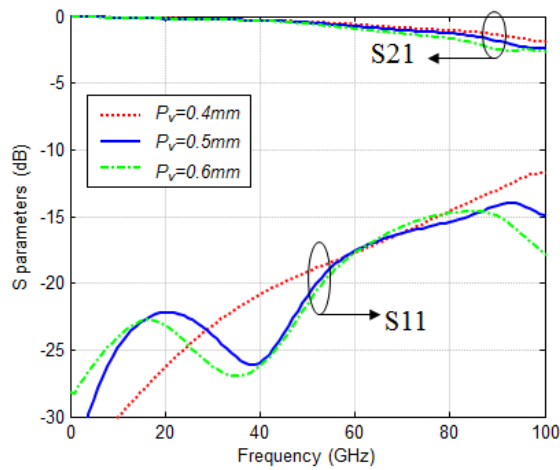
3.2.2 Measurement

3.2.2.1 System set-up

As discussed in Section 1.2, the traditional SMCs for device integration are lossy and expensive at *W*-band. As an alternative, G-S-G probes are typically utilized



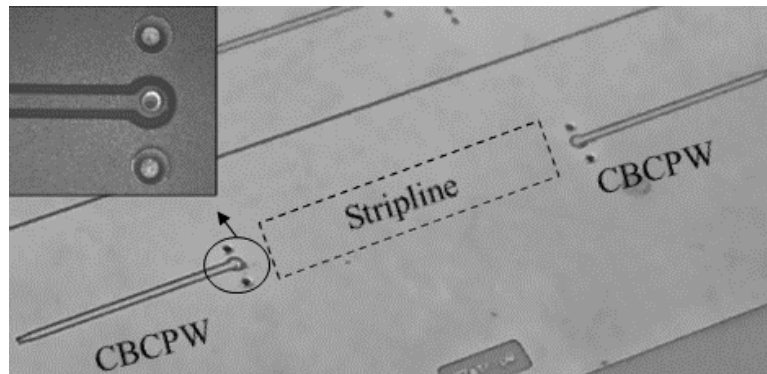
(a)



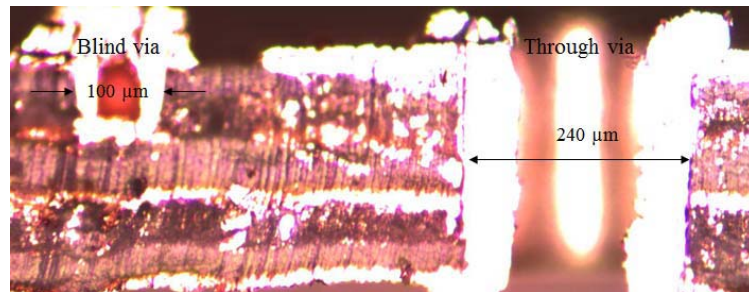
(b)

Figure 3.3. Simulated S-parameters of a CBCPW-to-SL transition: (a) tolerance analysis of the diameter of the blind via, and (b) tolerance analysis of the pitch between the blind and through vias.

to couple signals into and out of the DUTs at high frequencies, which have a characteristic impedance of 50Ω and provide a CPW mode. In the measurement set-up, the probes on probe stations were integrated with Agilent PNA E8361C and mmW



(a)



(b)

Figure 3.4. (a) Fabricated CBCPW-to-SL-to-CBCPW transition, and (b) cross-section cut of the fabricated back-to-back transition.

head controller N5260A. Then, the two probes were calibrated with CS-5 calibration substrate from GGB Industries Inc. using SOLT method. The same system set-up and calibration method will be utilized in the following sections and chapters without special clarification.

3.2.2.2 Back-to-back transition

To demonstrate the proposed CBCPW-to-SL transition, its back-to-back transition was designed and fabricated, which consists of one SL and two CBCPWs, as

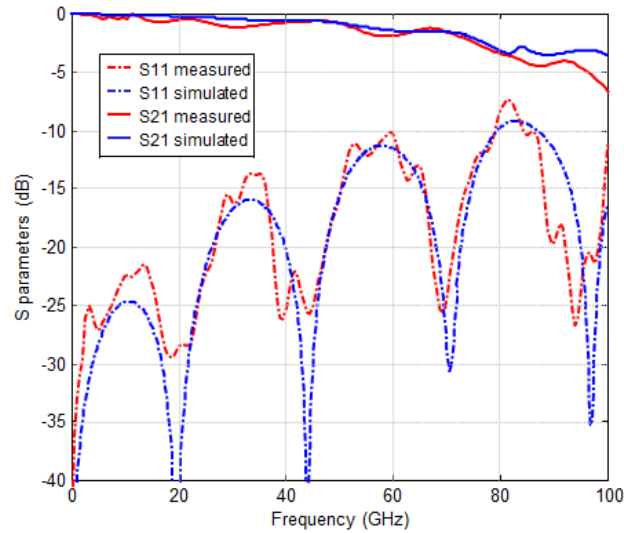


Figure 3.5. Simulated and measured S-parameters of the back-to-back transition with a 3 mm long SL.

shown in Figure 3.4 (a). Choosing two CBCPWs is for the consideration of probing. The fabricated CBCPW's signal line width is reduced to $105\ \mu\text{m}$, while its gap width is increased to $80\ \mu\text{m}$ due to the fabrication tolerance. The length and width of the SL are 3 mm and $58\ \mu\text{m}$, respectively. The cross-section cut of the transition is shown in Figure 3.4 (b). It can be seen that the laser-drilled vias are slightly tapered cylinders. The diameter of the blind via varies from $93\ \mu\text{m}$ to $100\ \mu\text{m}$, and that of the through vias varies from $220\ \mu\text{m}$ to $240\ \mu\text{m}$.

The measured S-parameters of the back-to-back transition are illustrated in Figure 3.5, showing good agreement with the simulated results. The insertion loss is 1.8 dB at 60 GHz and less than 2.5 dB up until 78 GHz, and the reflection remains less than -10 dB from DC up to 78 GHz. The slight discrepancy between the simulated and

measured data may be attributed to fabrication tolerances and probe positioning uncertainty.

3.3 MS-to-SIW Transition

Recently, substrate integrated waveguides have been developed to adapt traditional rectangular waveguides into planar substrates with existing PCB technologies. SIWs are typically fabricated by using two rows of conducting vias connecting two parallel grounds [44], which preserve most of the rectangular waveguides' advantages, i.e., high-power handling capability and perfect electrical shielding, and can further provide low profile, light weight, and simple integration. Typically, the loss of a SIW is higher than that of a hollow rectangular waveguide due to the dielectric loss of the substrate material. A carefully designed SIW can only support TE_{10} mode within a wide spectrum and, therefore, can be utilized to purify the guided mode and improve the module's EMC. Generally, SIWs can be fed by using MS lines, CPWs, and CBCPWs [44]. As discussed in Section 3.1, MS lines are utilized to interconnect different circuit components in the receiving module due to their relatively low propagation loss and shielding ground. Thereby, an efficient transition from MS line to SIW is desired in the proposed module.

As can be seen in Figure 3.1, the MS line mode is a quasi-TEM mode, and the SIW mode is a TE_{10} mode. These two modes have similar mode profiles in their substrates. Herein, a transition between a MS line and a SIW can be achieved directly by connecting the MS line's signal line to the SIW's top ground and the MS line's ground to the SIW's bottom ground. To date, several broadband MS-to-SIW transitions have been reported in planar or multilayer substrates [44]-[46] at microwave frequencies, which, however, may not be migrated to high frequencies, e.g.,

95 GHz. As the frequency increases to *W*-band, due to the limited commercial fabrication resolution of the micro vias discussed in Section 1.2, the pitch between vias becomes electrically ‘large’ in terms of wavelength, which may introduce additional leakage loss at such high frequencies. Thus, the MS-to-SIW transitions reported at microwave frequencies have to be validated at *W*-band.

In this section, I present a planar MS-to-SIW transition on a thin film LCP substrate and demonstrate its application in commercial printed circuits. The proposed transition achieves a low loss of less than 1.6 dB and an ultra-wide bandwidth from 60 to 110 GHz.

3.3.1 Transition Design

To minimize the impact of multilayer lamination tolerance, the MS line and SIW are designed in a core LCP layer. The thickness of this core layer is chosen as 100 μm to minimize the propagation loss of the MS line and SIW. The proposed MS-to-SIW transition is a linear taper between a MS line and a SIW, whose configuration is illustrated in Figure 3.6. The width of the SIW is denoted as w , and the corresponding effective width is:

$$w_{eff} = w - \frac{d^2}{0.95s}, \quad (3.1)$$

where d and s are the diameter and pitch of the vias, respectively. The corresponding cut-off frequency of the SIW can be calculated using the following formula [44]:

$$f = \frac{c}{2w_{eff}\sqrt{\epsilon_r}}, \quad (3.2)$$

where c is the speed of light in free space, and ϵ_r is the dielectric constant of the substrate. Limited by the fabrication aspect ratio (1.25:1) and thickness of the

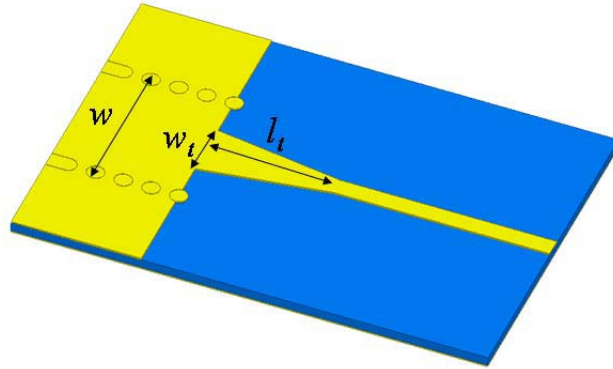


Figure 3.6. Configuration of the MS-to-SIW transition.

Table 3.2. Cut-off frequency of the SIWs and dimensions of the corresponding MS-to-SIW transitions.

w (mm)	w_{eff} (mm)	f_c (GHz)	l_t (mm)	w_t (mm)
1.5	1.35	64	1.35	0.6
1.7	1.55	56	1.5	0.7
2.2	2.05	43	1.6	1.3

multilayer substrates [9], the diameter and pitch of the vias are designed as 250 and 300 μm , respectively. The dimensions of the transitions with SIWs of different width and cut-off frequencies are listed in Table 3.1. To match the cut-off frequency of a WR-10 waveguide, the SIW's width is chosen as 1.7 mm. The width of MS lines is 240 μm , providing an impedance of 50 Ω .

Ansys HFSS was utilized to design and optimize the proposed transition. The simulated S-parameters of a MS-to-SIW transition with a 1.7mm wide SIW are illustrated in Figure 3.7. It can be seen that the simulated insertion loss is less than 0.7

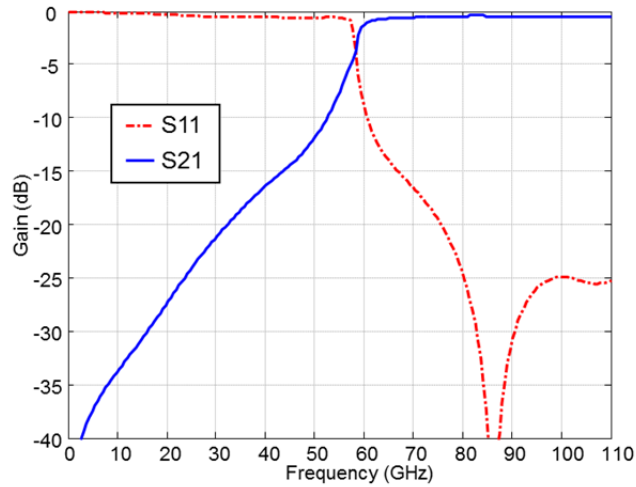


Figure 3.7. Simulated S-parameters of a MS-to-SIW transition ($w = 1.7$ mm).

dB, and the reflection is less than -15 dB at *W*-band. The simulated cut-off frequency of the SIW is 57.6 GHz, which is slightly higher than the calculated one in Table 3.1.

3.3.2 Measurement

3.3.2.1 CBCPW probe pad

At high frequencies, i.e., *W*-band, G-S-G probes are typically utilized to measure the RF components. To match the modes between the MS line and G-S-G probe, a CBCPW probe pad was designed to terminate the MS lines, as illustrated in Figure 3.8 (a). In the HFSS model, the designed width of the CBCPW's signal line and gap is 80 and 50 μm , respectively, and the taper length is 0.2 mm. For the fabricated device, the width of the signal electrode reduces to 70 μm , while the gap between the signal line and ground increases to 60 μm due to the fabrication tolerance.

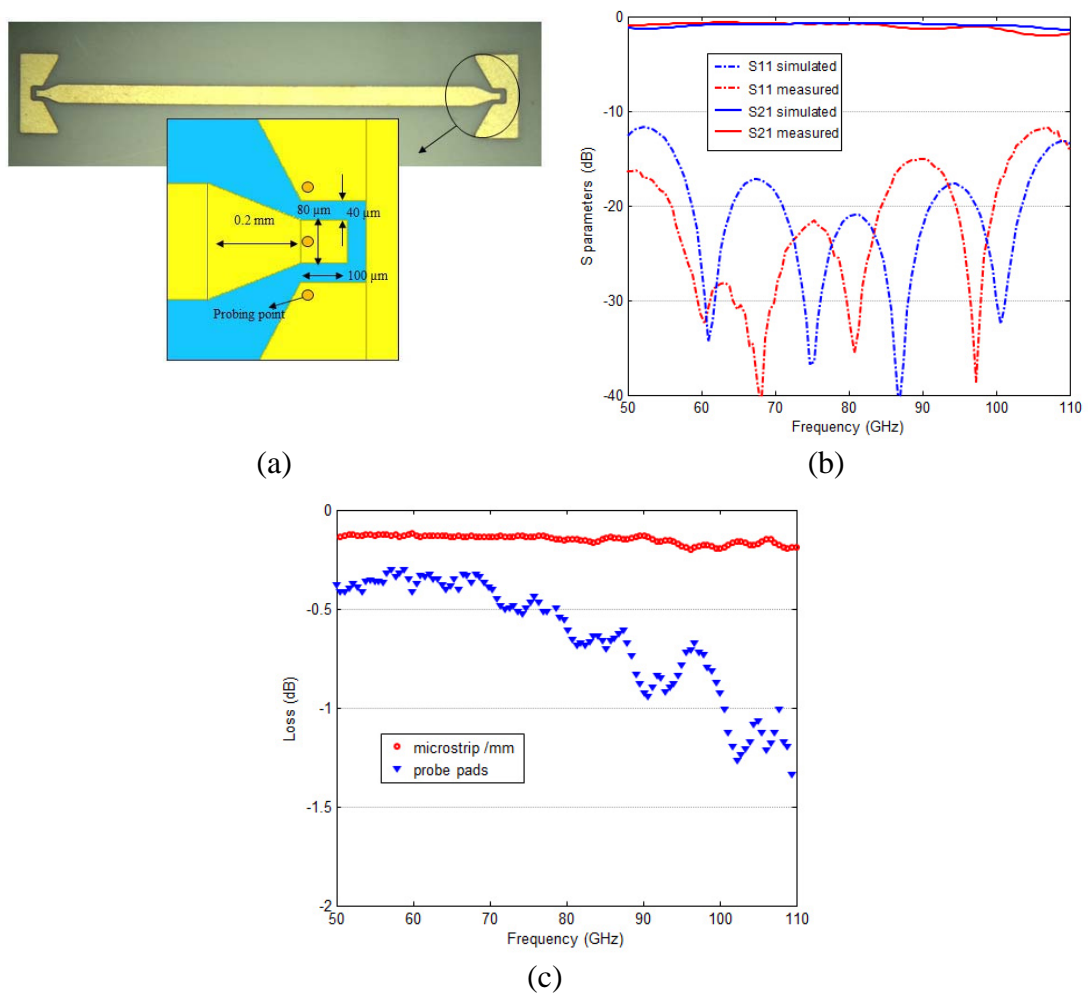


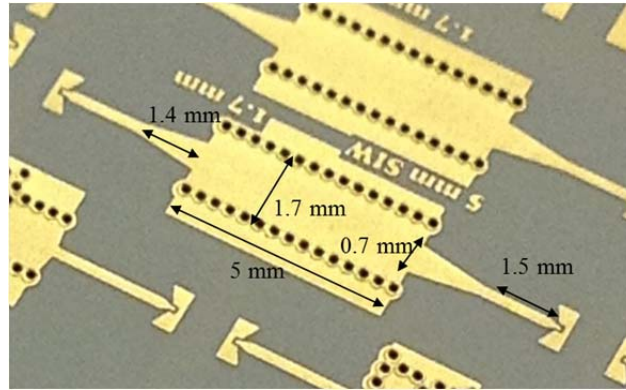
Figure 3.8. (a) Configuration of a CBCPW probe pad and its back-to-back transition,(b) simulated and measured S-parameters of a 5mm long MS line terminated with a pair of probe pads, and (c) calculated propagation loss of a MS line and insertion loss of a pair of probe pads.

This overetching enlarges the corresponding impedance of the CBCPW up to around 80 Ω . The probing position is chosen right at the end of CBCPW to minimize the mismatch.

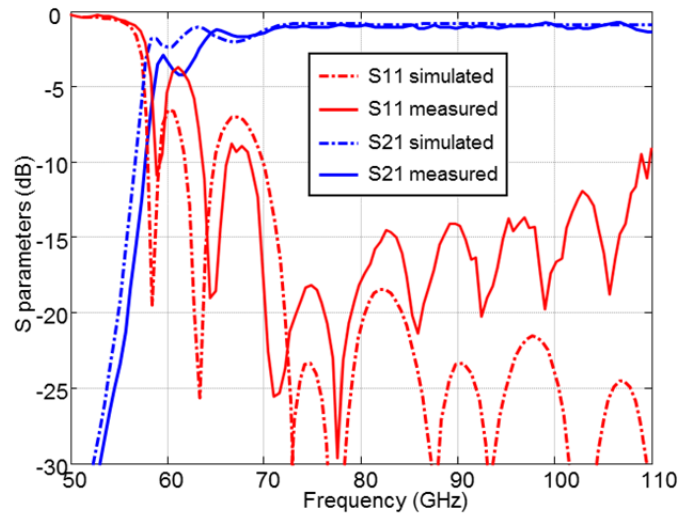
To characterize the insertion loss of the proposed probe pads, back-to-back structures including two CBCPW probe pads and MS lines with different length, are fabricated and measured. The simulated and measured S-parameters of a 5mm long MS line with a pair of probe pads are illustrated in Figure 3.8 (b). The loss of the MS line can be calculated by dividing the S21 discrepancy of the back-to-back structures by their length difference. Then, the insertion loss of a pair of CBCPW probe pads can be derived by subtracting the loss of the MS line from the total loss of a back-to-back transition. More than twenty devices were measured to obtain robust loss curves, which are illustrated in Figure 3.8 (c). The propagation loss of the MS line is less than 0.14 dB/mm from 50 GHz to 110 GHz, showing good agreement with the simulated data in Table 3.1, and the loss of a pair of probe pads is lower than 1.4 dB at *W*-band. The relatively large ripples from 95 to 110 GHz may be attributed to the spectrum edge error of calibration and probing position uncertainty. The designed CBCPW probe pads will be utilized in the measurements of the devices with MS line feed in the following sections and chapters.

3.3.2.2 Back-to-back transition

To validate the design of the proposed transition, a MS-to-SIW-to-MS transition terminated with a pair of CBCPW probe pads was designed and fabricated. The length and width of the SIW is 5 mm and 1.7 mm, respectively, and the length of MS lines is 1.5 mm, as illustrated in Figure 3.9 (a). The measurement set-up and calibration method discussed in Section 3.2.2 were utilized for this test. Figure 3.9 (b) illustrates the measured and simulated S-parameters of the back-to-back structure, revealing reasonable agreement. The measured insertion loss is less than 1.6 dB at *W*-band, and the measured reflection is less than -13 dB within the working spectrum. It



(a)



(b)

Figure 3.9. (a) Fabricated MS-to-SIW-to-MS transition, and (b) simulated and measured S-parameters of the back-to-back transition ($w = 1.7$ mm).

can be concluded that SIWs and the MS-to-SIW planar transition can be fabricated in multilayer LCP substrates using commercial large-panel PCB technologies while maintaining low propagation loss and low leakage for the SIWs.

3.4 SIW-to-Waveguide Transition

Hollow rectangular waveguides (RWGs), one of the earliest transmission components for microwave signal transportation, have been widely utilized in the microwave and mmW systems due to their low loss, high power handling capability, and perfect electrical shielding. However, RWGs are bulky and heavy, and, thereby, not suitable for high-density and weight-constrained applications [25] [44]. Alternatively, SIWs have gained tremendous interests in these applications [44], which preserve the traditional RWGs' advantages, and can achieve low profile, light weight, and friendly packaging. So far, many efforts have been done to investigate SIW-to-rectangular waveguide transitions [46]-[54]. According to the mechanism used, these transitions can be classified into two categories: slot coupled transitions on the broadside [46]-[47] and travelling-wave transitions in the propagation direction [48]-[54]. The former utilize one or two slots on the SIW's broadside wall to couple signal into RWG. However, their bandwidth is typically several percent due to the SIWs' high quality factor. The latter are typically achieved by using tapered housings [48]-[51] or fin-lines [52]-[54] to gradually match the TE_{10} modes of the SIWs and RWGs in the wave propagation direction, and can achieve broad bandwidth at a cost of circuit footprint.

Recently, SIWs have been investigated in multilayer circuitry [25] due to their aforementioned advantages. However, it should be noted that all the reported SIW-to-RWG transitions [46]-[54] are designed on a single layer substrate, which may not be applicable in the multilayer substrate. On one hand, the broadside slot coupled transitions may have limited applications due to their narrow bandwidth and large profile in the broadside direction. On the other hand, for the travelling-wave transitions, the substrate thickness becomes electrically 'thick' in terms of wavelength

at *W*-band, easily exciting substrate mode in the multilayer substrates. To this end, a guided structure, e.g., fin-line, may be required to achieve an efficient transition. However, the reported transitions with the via-guided fin-lines [52]-[53] may not be suitable for the multilayer substrates at *W*-band. Due to the limited fabrication aspect ratio [9], the pitch and diameter of the vias in a thick multilayer substrate become electrically ‘large’ at *W*-band, introducing undesired leakage and radiation. Meanwhile, thicker substrate means larger and higher ring bump for the vias, which may further aggravate the leakage.

In this section, a SIW-to-RWG transition in multilayer LCP substrates is presented at *W*-band. The SIW is designed in the top LCP layer with a thickness of 100 μm , and laminated with another LCP layer underneath. A linearly flared slot-line without guided vias transitions the SIW to WR-10 rectangular waveguide efficiently. The proposed transition achieves low insertion loss and low reflection within the working spectrum.

3.4.1 Transition Design

Due to the antipodal asymmetry, the proposed SIW-to-RWG transition requires an electrically ‘thin’ substrate to minimize the polarization mismatch between the guided modes of the slot-line and RWG. To this end, the proposed transition is designed in the top LCP layer with a small thickness of 100 μm . A LCP bond-ply and a bottom LCP with a thickness of 50 μm are laminated with the top LCP layer to form a multilayer circuit. The configuration of the proposed transition is illustrated in Figure 3.10. Differing from the reported transitions with curved fin-lines [52]-[53], the proposed transition employs a linearly flared slot-line, and does not utilize vias in the transition region, thus minimizing the potential leakage. The top and bottom walls of

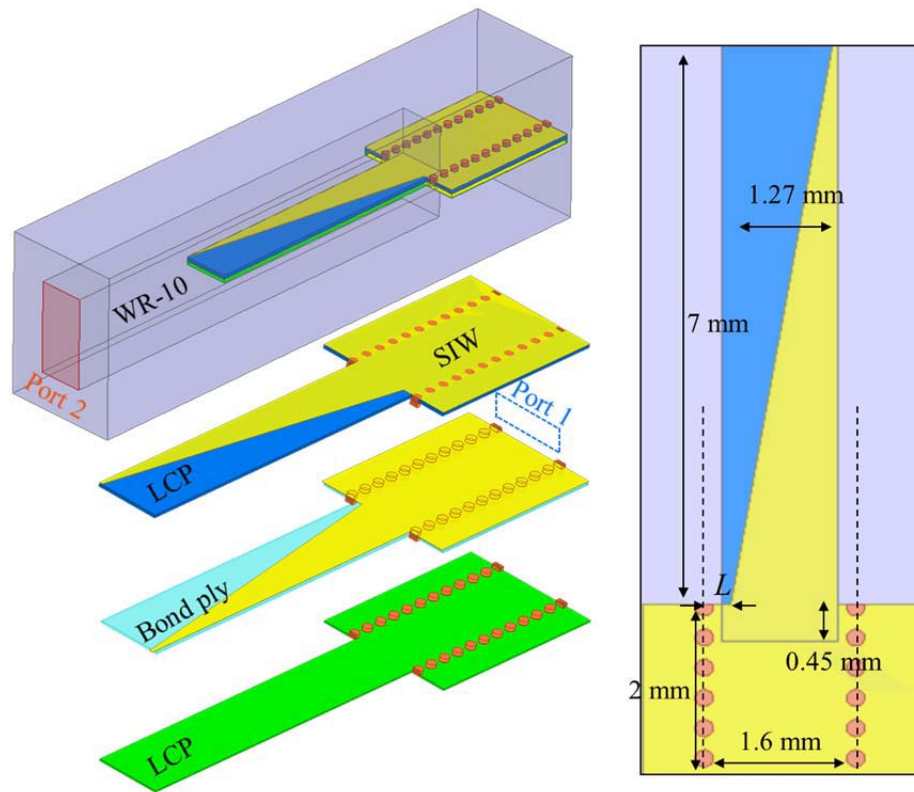


Figure 3.10. Configuration and dimensions of the SIW-to-WG transition in multilayer LCP substrates.

the SIW deviate with an odd symmetry to feed the slot-line. The diameter and pitch of the vias for the SIW is 250 and 300 μm , respectively. Then, the slot-line is linearly flared out and inserted into a WR-10 waveguide. By using this linear transition, the E-field of the SIW will be rotated 90° to excite the TE_{10} mode of the RWG.

To optimize the transition, 3-D full-wave models are designed and simulated in Ansys HFSS, as illustrated in Figure 3.10. The width of the SIW is chosen as 1.6 mm,

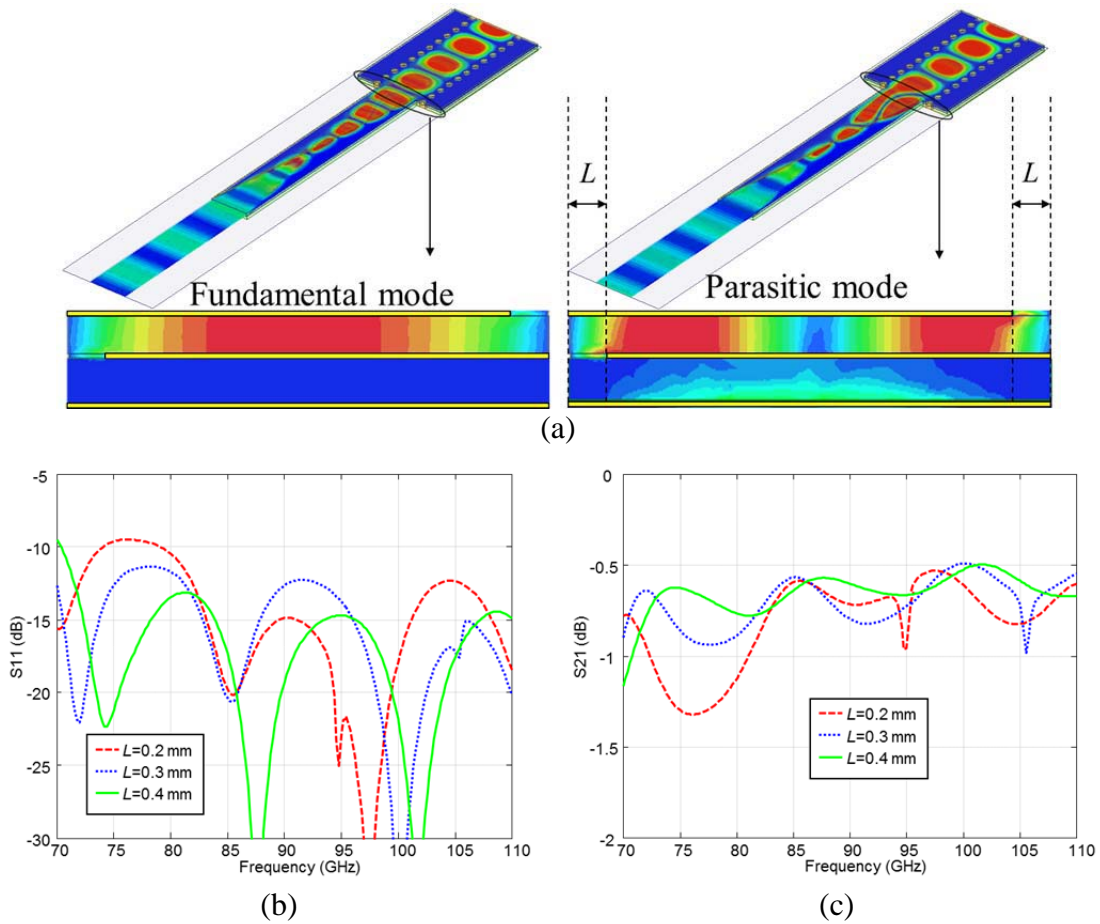


Figure 3.11. (a) Propagation and cross-section of the fundamental and parasitic modes of the proposed SIW-to-WG transition, and simulated (b) S_{11} and (c) S_{21} of the transition with varying L at W-band.

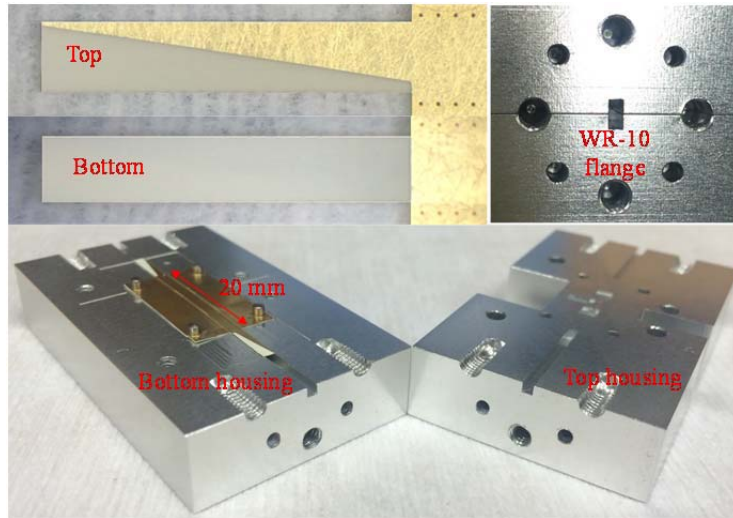
providing the same cut-off frequency as the WR-10 waveguide. The length of the flared slot-line is 7 mm, and the distance between the edges of the slot-line and SIW is depicted as L . The bond-ply and bottom LCP introduce index asymmetry between the top and bottom electrodes of the antipodal slot-line and, thereby, may excite a parasitic mode at high frequencies. The fundamental and parasitic modes of the proposed

transition are illustrated in Figure 3.11 (a). It can be found that this mode is confined between the top and bottom electrodes of the antipodal slot-line. Therefore, increasing L can push the parasitic mode to high frequencies. The simulated S-parameters of the transition with sweeping L are illustrated in Figure 3.11 (b). At $L = 0.4$ mm, the parasitic mode occurs at 117 GHz, beyond W -band. Further increasing L may increase the mode mismatch between the slot-line and SIW, thus enlarging the loss of the proposed transition significantly.

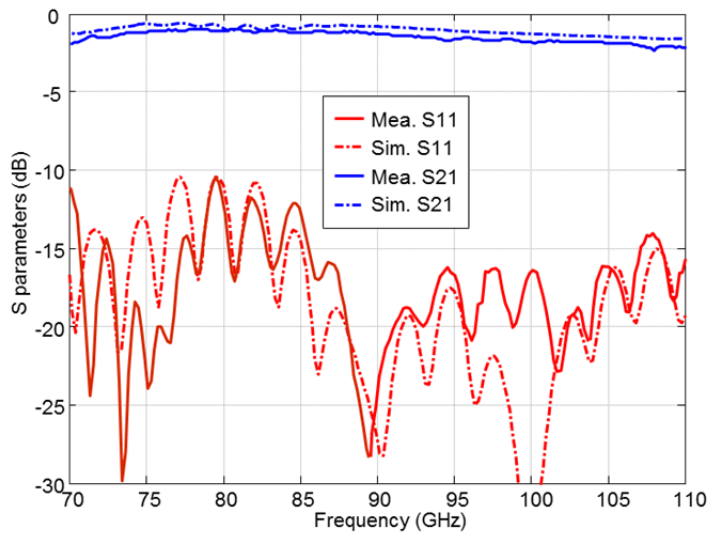
3.4.2 Measurement

To characterize the proposed transition, a RWG-to-SIW-to-RWG transition was designed and fabricated, as illustrated in Figure 3.12 (a). The length of the SIW is designed as 20 mm, providing enough space for the registration posts. A metallic housing is carefully designed to provide WR-10 waveguide input and output with a standard flange. In the measurement set-up, the external WR-10 waveguides were integrated with Agilent N5260 mmW heads and PNA E8361C and calibrated with SOLT method and W11644A calibration kit. Then, they were integrated with the packaged back-to-back transition and characterize its S-parameters.

The measured and simulated S-parameters of the back-to-back transition are illustrated in Figure 3.12 (b). The measured reflection is less than -11 dB, and the insertion loss is less than 1.9 dB from 70 to 110 GHz, showing good agreement with the simulated data. It should be noted that to precisely reveal the insertion loss of the back-to-back transition, the propagation loss of the SIW is eliminated, which can be calculated by using the method to calculate the insertion loss of probe pads discussed in Section 3.3.2. Both the simulated and measured S-parameters reveal that the proposed SIW-to-RWG transition does not excite substrate modes at W -band.



(a)



(b)

Figure 3.12. (a) Fabricated waveguide-to-SIW-to-waveguide transition with metal housing, and (b) simulated and measured S-parameters of the back-to-back transition.

3.5 MS-to-CPW Transition

Coplanar waveguide (CPW) is one type of transmission line whose signal and ground conductors are in the same plane, namely, on the top surface of the dielectric substrate [10]. Traditionally, CPWs are widely used in monolithic microwave/millimeter integrated circuits (MMICs) due to the simple mounting of lumped components. In this case, CPWs are also preferable in the circuits of MMIC carriers to provide the same mode for the MMICs' integration. At mmW frequencies, CPWs typically provide lower propagation loss than the other transmission lines due to their unique mode profile and relatively low dielectric loss, as depicted in Figure 3.1 and Table 3.1. However, they are not suitable in multilayer circuits due to their poor layer-to-layer isolation. In the proposed front-end receiving module, CPWs can be utilized for the G-S-G probing in the measurement and integration with amplifiers or EO modulators. As mentioned in Section 3.1, MS lines are chosen as the transmission lines for interconnection. Therefore, an efficient transition from MS line to CPW is important for the proposed module.

Recently, many MS-to-CPW transitions have been reported in single or multilayer substrates [55]-[63]. The transitions in a single-layer substrate are mainly designed for the input/output probe pads in RFICs or MMICs [55]-[57], typically having compact dimensions at a cost of relatively high insertion loss. The reported multilayer transitions are designed for surface-to-surface connection by using micro vias [58]-[59] or coupling slots [60]-[61]. However, these transitions are not suitable for the proposed module, where both the MS line and CPW are on the top circuit layer. To achieve an ultra-wide bandwidth, reference [63] used a CBCPW to mitigate the mode mismatch between the MS line and CPW [63] at Ka -band. However, it should be noted that most of the reported transitions [55]-[63] are designed at low frequencies,

such as *Ku*- and *K*-bands, and may not be applied to *W*-band due to the fabrication limits discussed in Section 1.2.

In this section, I present a planar MS-to-CPW transition in a thin-film LCP substrate at *W*-band using a CBCPW as an intermedium between the MS line and CPW. The proposed transition can provide low loss, low reflection, and ultra-wide bandwidth.

3.5.1 Transition Design

As can be seen in Figure 3.1, the MS line mode and CPW mode are quasi-TEM modes. The former is mainly confined underneath the metal strip within the substrate, while the latter is close to the surface of the substrate. Combining these two modes can form a CBCPW mode. Thereby, a broadband MS-to-CPW transition can be achieved naturally by cascading a MS-to-CBCPW transition and a CBCPW-to-CPW transition, whose configuration is illustrated in Figure 3.13. To minimize the propagation loss of the MS line and CBCPW, the transition is designed on a 100 μm thick LCP substrate. The width of MS line is chosen as 240 μm , providing an impedance of 50 Ω , and the width of the signal line and gap of the CBCPW and CPW are 110 μm and 60 μm , respectively, which is limited by the commercial large-panel PCB fabrication standards discussed in Section 3.1. The corresponding impedance of CBCPW and CPW is approximately 70 Ω , as depicted in Table 3.1. To transition a MS line to a CBCPW, the signal line of the MS line is gradually narrowed down, and two grounds connected to the bottom ground with through vias are added on the top circuit layer. To achieve a CPW, a linearly tapered notch is introduced in the CBCPW's bottom ground to push the electrical fields lifting up towards the substrate surface. A 3-D full-wave model of the proposed transition was designed and simulated

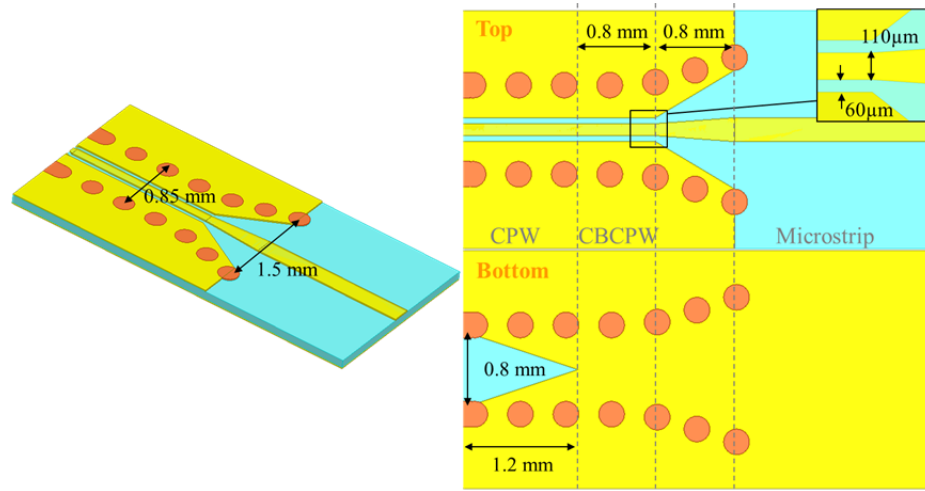
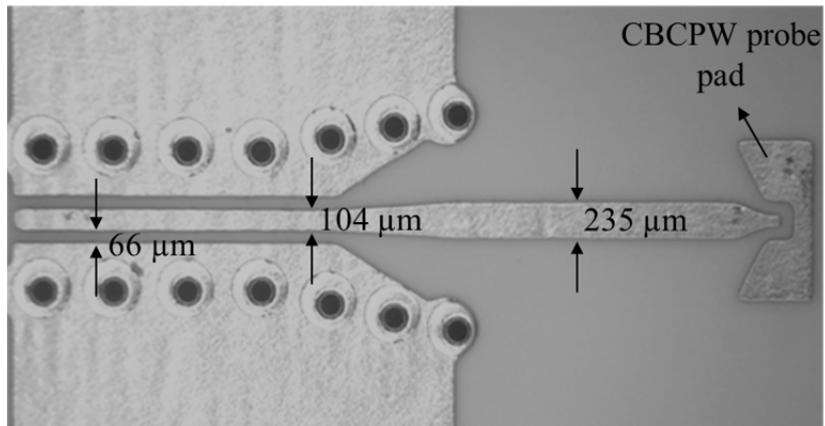


Figure 3.13. Configuration of the MS-to-CPW transition.

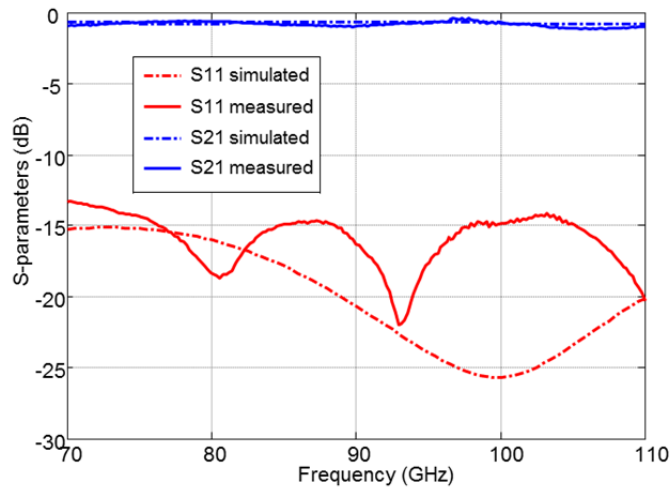
by using Ansys HFSS. The optimized dimensions of the transition are depicted in Figure 3.13. The length of the CBCPW is 0.8 mm, the length of the linear taper between the CBCPW and MS line is 0.8 mm, and the length and width of the notch in the bottom ground are 1.2mm and 0.8 mm, respectively. Figure 3.14 illustrates the simulated S-parameters of the proposed transition. It can be seen that the insertion loss is less than 0.8 dB, and the reflection is less than -15 dB from 70 to 110 GHz.

3.5.2 Measurement

The measurement system set-up and calibration method discussed in Section 3.2.2 are utilized to characterize the fabricated MS-to-SIW transition. The MS line is terminated with a low-loss CBCPW probe pad presented in Section 3.3.2. Figure 3.14 (a) illustrates the fabricated MS-to-SIW transition. It can be seen that the overetching is approximately 5 μm . In the measurement, the input and output probes are launched



(a)



(b)

Figure 3.14. (a) Fabricated MS-to-CPW transition with a CBCPW probe pad, and (b) simulated and measured S-parameters of this transition.

on the CBCPW probe pad and CPW, respectively, to couple the RF signal into and out of the transition. The measured S-parameters of the MS-to-CPW transition are illustrated in Figure 3.14 (b). It can be seen that the insertion loss and return loss are

less than -1 dB and -13.5 dB at *W*-band, respectively. Again, the discrepancy between the simulated and measured S-parameters may be attributed to the probe pad and fabrication tolerance.

3.6 Summary

In this chapter, I first discussed the transmission components desired in the multilayer LCP based front-end receiving module, including MS lines, CBCPWs, CPWs, SLs, RWGs, and SIWs. MS lines are utilized for interconnection, CBCPWs and CPWs are designed for the integration with MMICs and EO modulators as well as probing, and SIWs and SLs can be used to suppress the undesired substrate modes. In Section 3.2, a CBCPW-to-SL vertical transition is presented, which is achieved using one blind via connecting the signal lines and two through vias connecting the grounds in multilayer substrates. Then, a planar MS-to-SIW transition using a linear taper was presented in Section 3.3, and a SIW-to-RWG transition in multilayer substrates was presented in Section 3.4. The latter transition is achieved using a linearly flared antipodal slot-line without guided vias in the transition region, and, thereby, can minimize the potential leakage. In Section 3.5, I presented a planar MS-to-SIW transition for probing and integration purposes, which comprises a MS-to-CBCPW transition and a CBCPW-to-CPW transition. These four transitions can provide low loss and low reflection within an ultra-wide band covering the frequencies at *W*-band.

Chapter 4

MULTI-CHIP MODULE INTEGRATION AND PACKAGE

W-band frequencies within the millimeter wave spectrum have gained tremendous interest in various applications, including vehicle collision avoidance radar, gigabyte data rate communication, local wireless network, and passive and active imaging [25] [44], etc. To cover a large dynamic range and achieve high detection sensitivity, high-gain and low-noise figure receiving modules are of great interest, which typically comprise multiple microwave/mmW monolithic integrated circuits, such as low noise amplifiers and power amplifiers. Also, other system constraints, i.e., high density, low profile, low loss, and light weight [63], also need to be carefully considered in these applications, which typically can be achieved by using multilayer circuitry. However, as the frequency and packaging density increases, loss, reflection, and stray radiation in the form of crosstalk and package moding become critical limiting factors for multi-chip modules (MCMs) [64]. Traditional packaging technologies for the single-chip and low gain modules may not be suitable for high gain MCMs at *W*-band.

Recently, system-on-package (SOP) technologies have received significant attention in module integration and packaging at *W*-band [65]-[69]. However, most papers reported so far investigate single-chip modules (SCMs) with a fairly low gain of less than 18 dB using flip-chip bonding techniques. References [65] and [66] utilize traditional substrates, silicon and ceramic, as the MMIC carriers, respectively. However, these two kinds of substrates cannot be stacked to achieve multilayer

circuits and, thereby, are not able to provide high density for the components and assembly in a module. As an alternative, LCP is an ideal material for multilayer circuit at mmW frequencies, and has been investigated as MMIC carriers in Ref. [67]-[69]. Nevertheless, the integration of MMICs on LCP substrates using traditional flip-chip or wire bonding is challenging due to the large permittivity mismatch between the LCP and MMICs' substrates. Typically, flip-chip bonds require CPWs or CBCPWs as the feed lines for the MMICs. However, due to the low permittivity of the LCP substrate, it is critical to fabricate a $50\ \Omega$ CPW or CBCPW with a similar mode profile to that of the MMICs' probe pads at *W*-band using the commercial large-panel circuit print technologies [9]. Customized thin metal claddings [67]-[69] may be applied to the LCP substrate to improve fabrication resolution and achieve compact CPWs or CBCPWs. However, thin metal cladding increases the cost significantly, especially for large-panel and large-quantity applications. In addition, wire bonding is more versatile, and can be utilized for CPW, CBCPW, and microstrip (MS) line feeds. References [70]-[72] investigated the wire-bonded modules on LCP substrates at low frequencies, i.e., *Ka*-band. However, these feeding transmission lines suffer from the same mode mismatch due to the aforementioned permittivity mismatch. Besides, as the frequency increases, the inductance of the traditional wire bond increases significantly, thereby introducing additional impedance mismatch as well.

In this chapter, I present the integration and packaging techniques for high-gain MCMs in multilayer LCP substrates and propose a 50 dB gain double-LNA module at *W*-band. The proposed module employs a four-circuit layer LCP substrate as a MMIC carrier, which was fabricated on 12×18 inch panels using commercial state-of-the-art large-panel circuit print technologies [9]. In the proposed MCM, RF

components and bias circuits are distributed in different layers in order to achieve higher density. To efficiently integrate the LNAs with the MS line feeds, V-shape wire bonds are designed as a substitute to the traditional wire bonds. The proposed MCM achieves high gain, low NF, and linear phase at *W*-band. This chapter is organized as follows. In Section 4.1, the utilized LNA will be discussed. Then, the multilayer LCP carrier and V-shape wire bond will be depicted in Section 4.2 and 4.3, respectively. In Section 4.4, I will present the developed single-LNA and double-LNA modules. In Section 4.5, the package technologies will be discussed.

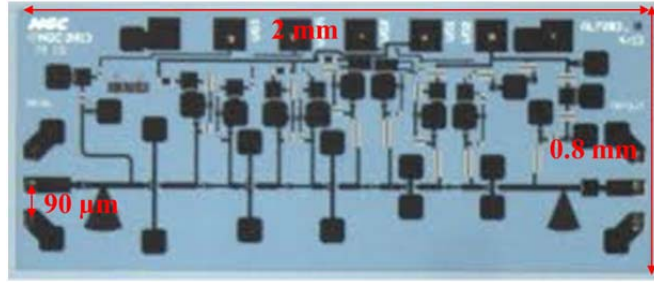
4.1 NG ALP283 Low Noise Amplifier

To achieve high gain and low NF, the state-of-the-art Northrop Grumman (NG) ALP283 LNA was chosen for the proposed modules, which can provide a high gain of 30 dB and a low NF of less than 2.5 dB at *W*-band [73]. The configuration of the LNA is illustrated in Figure 4.1 (a). It is 2 mm long and 0.8 mm wide, and is fabricated on a 75 μ m thick indium phosphide (InP) substrate. The pitch between the signal and ground bond pads is 90 μ m. Figure 4.1 (b) shows the on-chip measured gain of the LNA. It can be found that the measured gain is higher than 30 dB from 80 to 100 GHz. The active input and output impedances of the LNA can be extracted from the on-chip measured S-parameters as follows [11]:

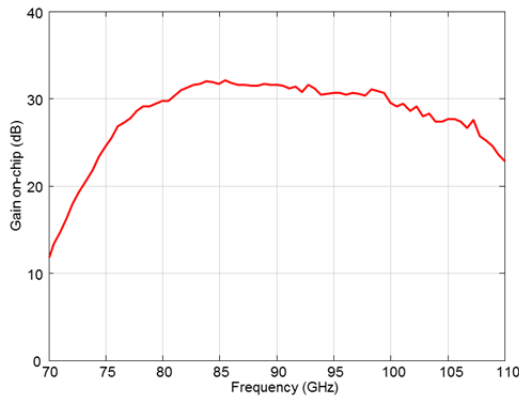
$$Z_{11} = \frac{(1 + S_{11})(1 - S_{22}) + S_{12}S_{21}}{\Delta S} Z_0 \quad (4.1)$$

$$Z_{12} = \frac{2S_{12}}{\Delta S} Z_0 \quad (4.2)$$

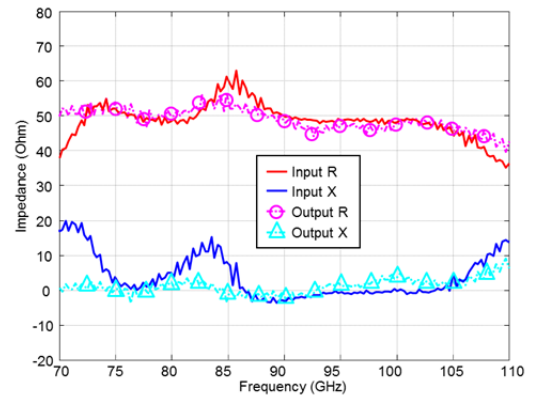
$$Z_{21} = \frac{2S_{21}}{\Delta S} Z_0 \quad (4.3)$$



(a)



(b)



(c)

Figure 4.1. (a) Top view, (b) measured on-chip gain, and (c) calculated input and output impedances of the NG ALP283 LNA.

$$Z_{22} = \frac{(1 + S_{22})(1 - S_{11}) + S_{12}S_{21}}{\Delta S} Z_0 \quad (4.4)$$

$$\Delta S = (1 - S_{11})(1 - S_{22}) - S_{12}S_{21} \quad (4.5)$$

$$Z_{in} = Z_{11} - \frac{Z_{12}Z_{21}}{Z_{22} + Z_L} \quad (4.6)$$

$$Z_{out} = Z_{22} - \frac{Z_{12}Z_{21}}{Z_{11} + Z_S} \quad (4.7)$$

where S_{mn} and Z_{mn} ($m = 1, 2$ and $n = 1, 2$) are the S- and Z-parameters, respectively; Z_0 , Z_L , and Z_S are the characteristic impedance, load impedance, and source impedance, respectively, and equal 50Ω in the on-chip measurement. The calculated input and output impedance of the LNA are illustrated in Figure 4.1 (c). It can be seen that the calculated active impedance of the LNA is approximately 50Ω at most of the frequencies at W-band. In this case, to minimize impedance mismatch, 50Ω transmission lines are preferred to feed the LNAs.

4.2 Multilayer-LCP MMIC Carrier

Multilayer printed circuits are superior to the traditional single-sided and double-sided circuits due to their high density, low connection loss, and multi-function capability [74]. At mmW frequencies, LCP is a promising material for the multilayer application due to its low loss, low dielectric constant, low water absorption, and available thicknesses down to $25 \mu\text{m}$ [8] [23]. The dielectric constant and loss tangent of LCP are approximately 3.2 and 0.004, respectively, at W-band [8]. Herein, a multilayer LCP substrate is chosen as the LNA's carrier, consisting of three LCP layers and four circuit layers, as illustrated in Figure 4.2. The thickness of the top LCP, inner bond-ply, and bottom LCP is $100 \mu\text{m}$, $50 \mu\text{m}$, and $50 \mu\text{m}$, respectively. The RF components, including LNAs, MS line feeds, and isolation structures, are designed in the top two circuit layers to minimize the impact of multilayer lamination tolerance, while the LNA bias and digital control circuits are designed in the bottom two layers, achieving high density and multi-function for the proposed module.

For the consideration of large quantity production, the proposed multilayer LCP carriers are fabricated using the commercial state-of-the-art large-scale circuit print technologies with a minimum fabrication resolution of $50 \mu\text{m}$ for circuit patterns

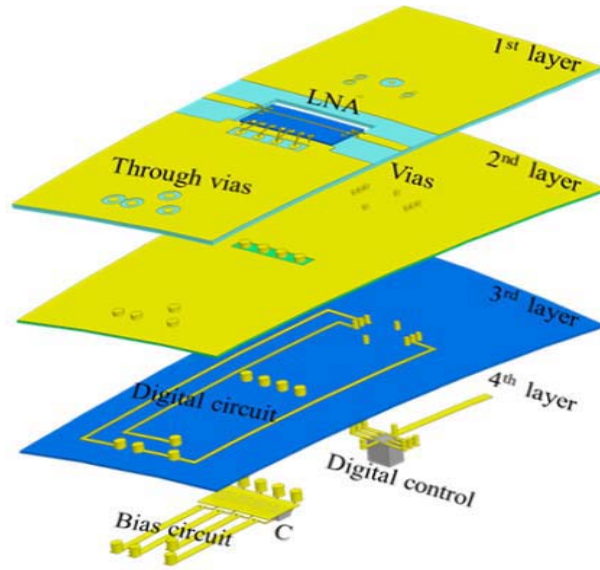


Figure 4.2. Layer-to-layer circuit schematic of the multilayer LCP carrier.

[9]. Generally, CBCPWs and MS lines are the two most prolific transmission lines in multilayer circuits due to their perfect layer-to-layer electrical shielding [74]-[75]. However, the CBCPWs are not suitable for the LNA integration on LCP substrates. On a 100 μm thick LCP substrate, in order to achieve a 50 Ω CBCPW with the commercial fabrication standards, the signal width of the CBCPW has to be as large as 200 μm , and the corresponding signal-to-ground pitch is much larger than that of the LNA bond pads (90 μm), leading to strong mode mismatch. To this end, 50 Ω MS lines with a width of 240 μm are chosen to feed the LNAs with carefully designed V-shape wire bonds, which will be presented in the next subsection. To probe the module, a pair of CBCPW probe pads presented in Section 3.3.2 are employed to terminate the MS lines.

4.3 V-Shape Wire Bond

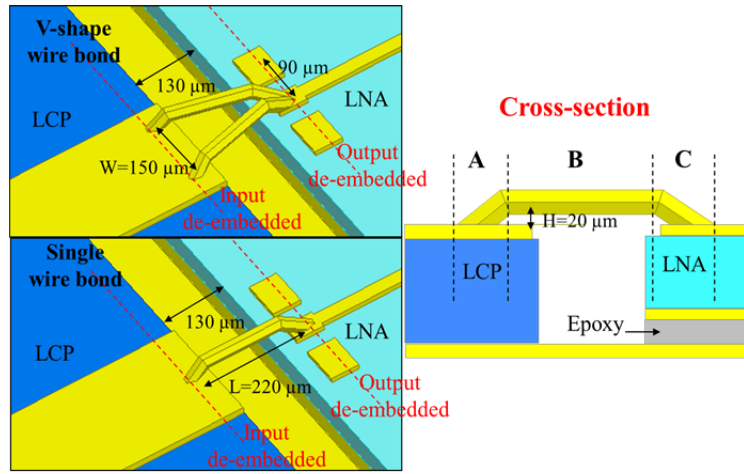
Flip-chip [76] and wire bonding [77] are the two main chip-level integration techniques at high frequencies. The former addresses low inductance and typically requires CPWs or CBCPWs as feed lines [76]. However, CPWs are not suitable for multilayer circuitry due to their poor layer-to-layer isolation, and CBCPWs suffer from the aforementioned mode dimension mismatch between the LCP and LNAs as well as inherent mode mismatch due to the fact that CBCPW mode is a combination of CPW and MS line modes. Alternatively, wire bonding can be adapted to most transmission lines, i.e., MS lines, CPWs, and CBCPWs. The inductance of a wire bond is typically larger than a flip-chip bond at high frequencies, and can be estimated by the following formula [14]:

$$L = 0.2 \cdot l \cdot \ln \left[\left(1 + \frac{2h}{d} \right) + 2 \sqrt{\frac{h}{d} \left(1 + \frac{h}{d} \right)} \right], \quad (4.8)$$

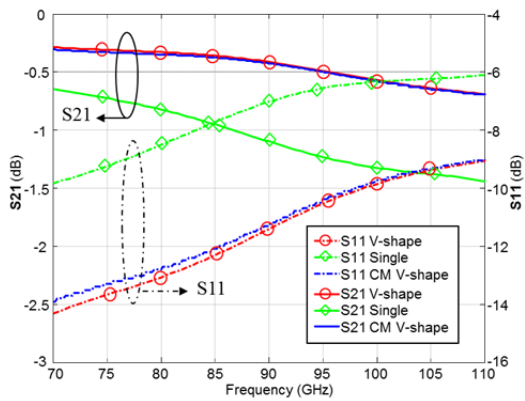
where l and d are the length and diameter of the wire bond, respectively, and h is the height of the wire bond with respect to the ground. It can be found that reducing h and l can decrease the inductance of wire bonds.

The utilized NG ALP283 LNA is designed for wire bond integration. To minimize the inductance of the wire bond, the LNA chip is embedded in a laser-drilled pocket in the top LCP layer, as illustrated in Figure 4.3 (a), reducing h in Equation (4.8). The empirical thickness of the conductive silver epoxy for the LNA adhering is approximately 20 μm . Thus, the LNA will be approximately level with the MS line feeds on the LCP substrate.

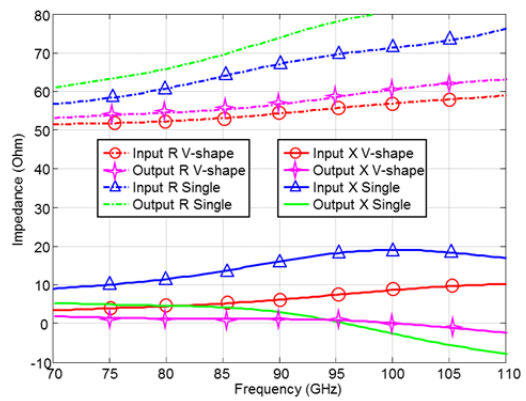
To match the mode profiles between the MS lines on the LCP substrate and LNA as well as further reduce the wire bond's inductance, V-shape wire bonds are



(a)



(b)



(c)

Figure 4.3. (a) Configuration of the V-shape wire bond and traditional single wire bond, (b) simulated S-parameters of these two wire bonds as well as the circuit module (CM) of the V-shape wire bond, and (c) calculated input and output impedances of the wire bonds.

designed and utilized for the LNA integration, as illustrated in Figure 4.3 (a). HFSS is utilized to construct and simulate the 3-D full-wave models of the proposed V-shape wire bond as well as a traditional single wire bond for comparison. The gap between

the LNA and MS line is 130 μm , and the length, L , and height, H , of the wire bond are 220 and 20 μm , respectively. The diameter of the wire bond is 25 μm , and the flared pitch, W , of the V-shape wire bond is 150 μm . In the simulation, the wave ports are de-embedded to the wire bonding positions, as shown in Figure 4.3 (a). The simulated S-parameters of the two wire bonds are illustrated in Figure 4.3 (b). It can be seen that the proposed V-shape wire bond provides much lower insertion loss and reflection than the traditional single wire bond. Tolerance analysis has been done to the V-shape wire bond's length (L) from 200 to 240 μm , flared width (W) from 130 to 170 μm , and height (H) from 10 to 30 μm , revealing little degradation to the performance of the proposed wire bond. Using Equations (4.1)-(4.7), the input and output impedances of these two wire bonds were calculated, as illustrated in Figure 4.3 (c). It can be seen that the proposed V-shape wire bond has a resistance of around 50 Ω and a low reactance of less than 10 Ω from 70 to 110 GHz.

To better understand the proposed V-shape wire bond, its equivalent circuit model was designed, as illustrated in Figure 4.4. According to the curvature, the low profile V-shape wire bond can be divided into three parts [77], i.e., *region A* on the LCP substrate, *region B* in free space, and *region C* on the LNA. L_{As} and L_{Aw} represent the inductances of the MS line and wire bond in *region A*, respectively; L_{Cs} and L_{Cw} are the inductances of the MS line and wire bond in *region C*, respectively. C_A and C_C are the capacitances for the bonding *regions A and C* [77], respectively, each including capacitance of MS line and fringing capacitance associated with the MS line open end [78]. In *region B*, R_B , L_B , and C_B are the resistance, inductance, and capacitance of each single wire bond, respectively. C_P is the capacitance between two wire bonds, and C_T is the parasitic capacitance for the wire bond taper. The values of these

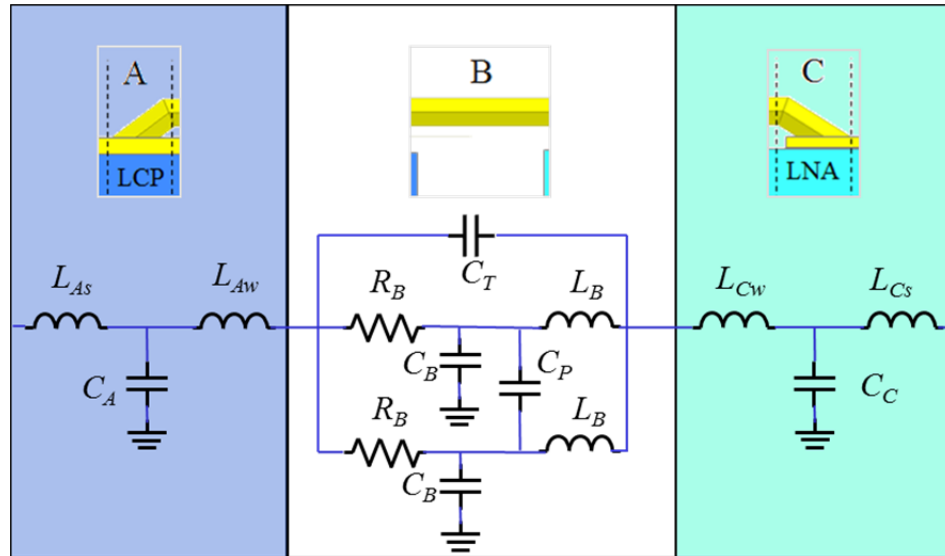


Figure 4.4. Equivalent circuit model of the proposed V-shape wire bond.

Table 4.1. Resistance, inductance, and capacitance of the circuit module for the V-shape wire bond.

Parameters	Values	Parameters	Values
L_{As}	8.5 pH	C_T	0.87 pF
L_{Aw}	77.5 pH	C_P	4.2 pF
C_A	0.0091 pF	L_{Cs}	1.4 pH
R_B	4.9Ω	L_{Cw}	28.5 pH
L_B	308 pH	C_C	0.0106 pF
C_B	0.0044 pF		

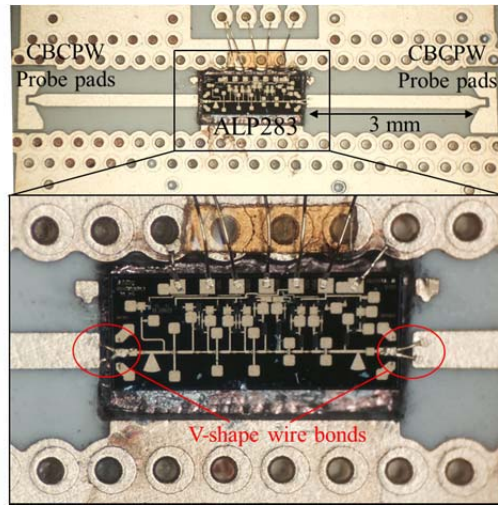
parameters for the circuit model can be estimated by using Keysight Advanced Design System (ADS) to match the simulated S-parameters obtained in HFSS, and are listed in Table 4.1. The S-parameters of the circuit model are also illustrated in Figure 4.3 (b), showing good agreement with the HFSS simulation.

4.4 Multi-Chip Module

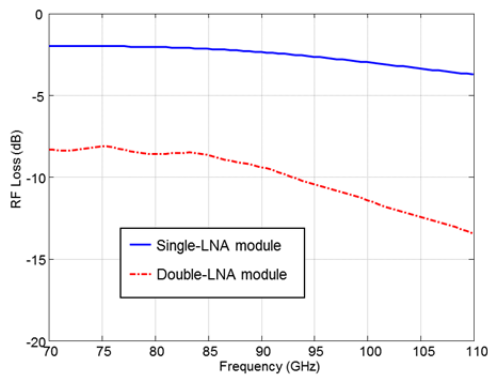
4.4.1 Single-LNA Module

The study of a MCM begins with a single-LNA module, which consists of one ALP283 LNA chip, two MS line feeds, a pair of CBCPW probe pads, and bias circuit, as shown in Figure 4.5 (a). The LNA chip is embedded in a pocket in the top LCP layer, and integrated with MS lines using V-shape wire bonds. The practical wire bonds have a length (L) varying from 210 to 235 μm , a flared width (W) varying from 133 to 160 μm , and a height (H) varying from 15 to 35 μm . Based on the tolerance analysis, these variations do not change the insertion loss of the V-shape wire bond significantly. The net loss of the single-LNA module can be estimated by combining the insertion losses of the individual components, including probe pads, V-shape wire bonds, and two 3mm long MS lines, and are illustrated in Figure 4.5 (b). It can be seen that the simulated net loss of the single-LNA module is less than 3.8 dB at W -band. Next, the net gain of the single-LNA module can be estimated by subtracting its net loss from the LNA's on-chip measured gain. The estimated net gain is higher than 27 dB from 80 to 100 GHz, as depicted in Fig. 5 (c).

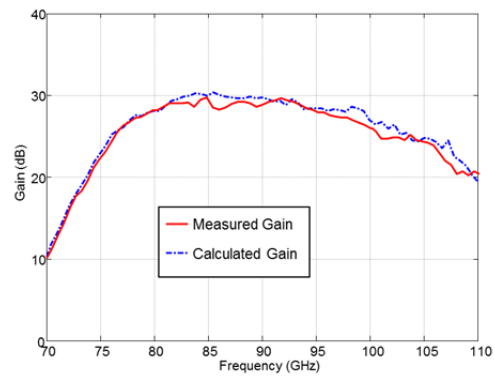
Throughout this measurement, the system set-up and calibration method aforementioned in Section 3.2 were utilized to characterize the single-LNA model as well as the following double-LNA module. The measured gain of the single-LNA module is illustrated in Fig. 4.5 (c). A high gain of 26.5-29.5 dB is demonstrated from 80 to 100 GHz, showing good agreement with the estimated gain. The discrepancy between the measured and calculated gain curves may be attributed to the fabrication and integration tolerance as well as the chip-to-chip gain variation.



(a)



(b)



(c)

Figure 4.5. (a) Configuration of the single-LNA module, (b) simulated net loss of the single-LNA module and double-LNA module, and (c) measured and calculated net gain of the single-LNA module.

4.4.2 Double-LNA Module

After successfully integrating and characterizing the single-LNA module, a MCM with two ALP283 LNA chips was investigated, as illustrated in Figure 4.6. Differing from the single-LNA module, substrate integrated waveguides (SIWs) are

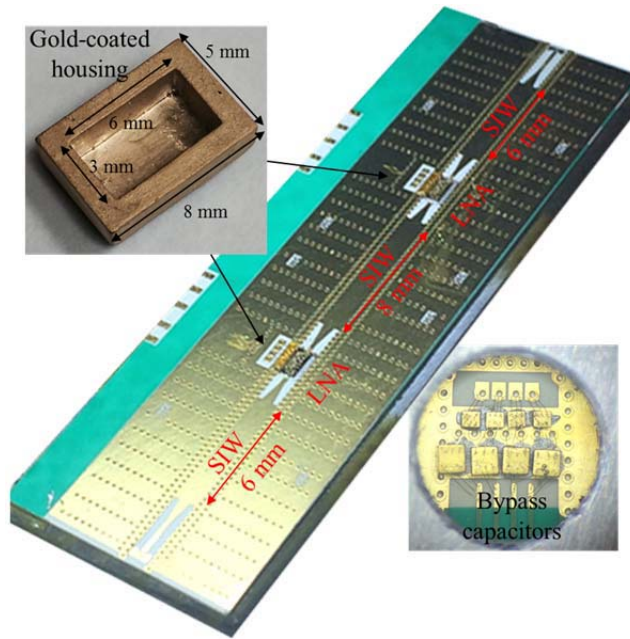


Figure 4.6. Packaged double-LNA module and 3-D printed housing.

designed and distributed between LNAs, and via barriers are distributed in the inactive region of the LCP carrier to minimize the undesired substrate modes in the carrier substrate. The diameter and pitch of the vias are 250 and 300 μm , respectively. The width of the SIW is 1.7 mm, and the corresponding cut-off frequency is approximately 58 GHz. Thereby, the SIWs can only support TE_{10} mode at *W*-band. The length of the three SIWs is 6, 8, and 6 mm, respectively. The SIW-to-MS transition presented in Section 3.2 is utilized to connect the SIWs with the MS lines, whose insertion loss is less than 0.7 dB from 70 GHz to 110 GHz. To eliminate the low-frequency oscillations, bypass capacitors are employed as high pass filters in the bottom circuit layer, as illustrated in Figure 4.6. As can be found in Figure 4.5 (b), the net loss of the

passive components in the double-LNA module, including SIWs, MS lines, SIW-to-MS transitions, CBCPW probe pads, and V-shape wire bonds, is less than 11.3 dB from 70 to 100 GHz. Thus, the net gain of the module can be calculated by subtracting its net loss (Figure 4.5 (b)) from two times of the on-chip gain of the LNA (Figure 4.1 (b)). Figure 4.7 (b) illustrates the estimated and measured net gain of the proposed module. The measured gain is higher than 45 dB from 78 to 100 GHz, and higher than 50 dB from 81 to 92 GHz, showing good agreement with the calculated data. The discrepancy can be attributed to the aforementioned reasons for the single-LNA module. The unwrapped phase of the double-LNA module is illustrated in Figure 4.6 (c), showing linearity at the working frequencies.

In wireless communication systems, NF is an important factor to describe noise performance, and determines the receiver's sensitivity. The NF of cascaded devices can be expressed as follows [79]:

$$NF_t = NF_1 + \frac{NF_2 - 1}{G_1} + \frac{NF_3 - 1}{G_1 G_2} + \frac{NF_4 - 1}{G_1 G_2 G_3} + \dots, \quad (4.9)$$

where NF_n and G_n (n is an integer) are the noise figure and gain of the cascaded n th element, respectively. Thus, the module's NF can be estimated by plugging the on-chip measured gain of a single LNA (Figure 4.1 (b)), the simulated insertion losses of the passive components, and the LNA's NF in NG's datasheet [73] into Equation (4.9). Figure 4.7 (c) illustrates the calculated and measured NFs of the proposed double-LNA module. The measured NF is characterized by using Y-factor method [79]. A W -band noise diode, QNS-FB15LW from Quinstar Inc., was integrated in front of the module as an excess noise ratio (ENR) source. By turning the noise diode on and off, Y-factor can be measured, and the NF of the module can be extracted. The measured

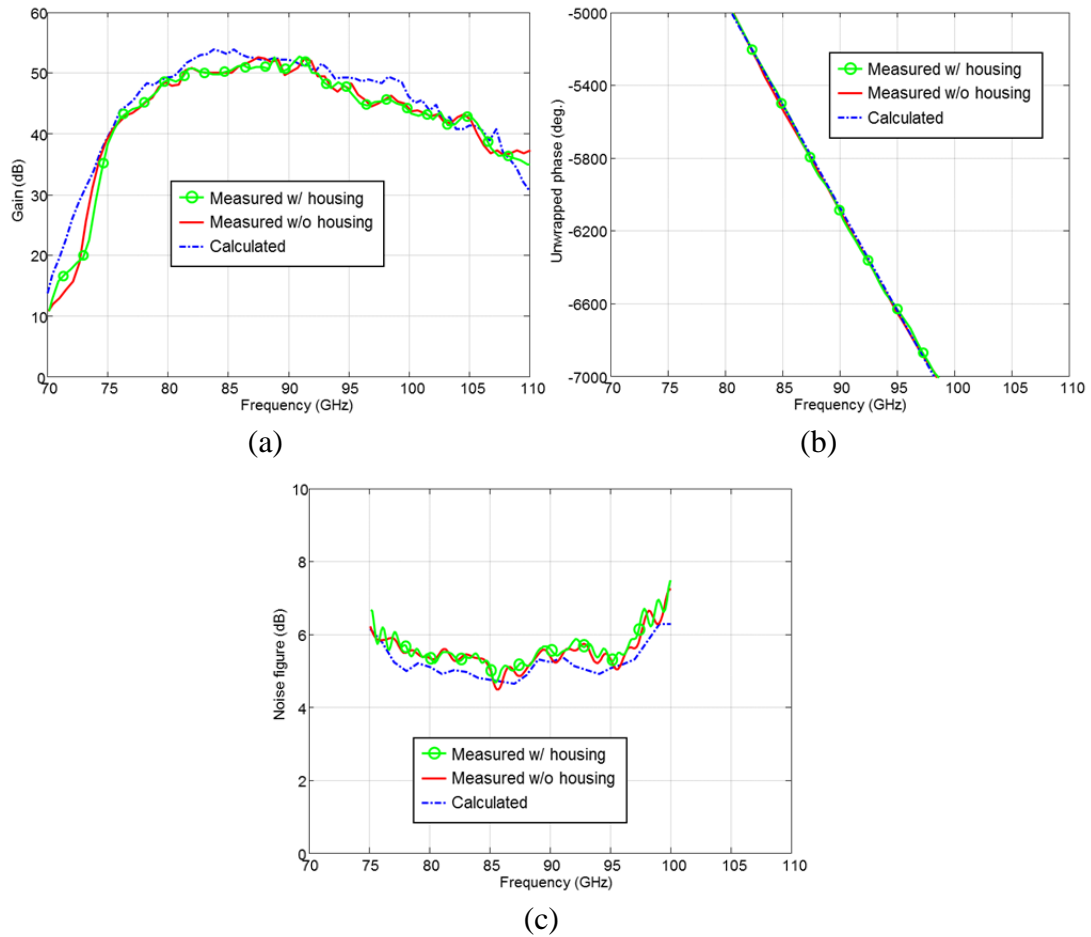


Figure 4.7. Measured and calculated (a) net gain, (b) unwrapped phase, and (c) noise figure of the double-LNA module.

NF of the proposed double-LNA module is less than 6 dB from 77 to 97 GHz, which is in good agreement with the calculated data. The small discrepancy can be attributed to the integration tolerance and the chip-to-chip NF variation. NG's datasheet [73] only provides the NF from 75 to 100 GHz. Thus, the measured NF is given in the same spectrum.

4.5 Packaging Technologies

Traditional mmW packaging utilizes metals [25] or ceramics [63], both of which are expensive, and have their own independent limitations. The metallic packaging is typically bulky and heavy, and ceramics require detrimentally high lamination temperature. As an alternative, inexpensive plastic packaging has gained great interest recently. References [70], [72], and [74] reported semi-hermetic organic packaging by laminating multilayer LCP substrates. However, these LCP packages cannot provide metallic cavities to isolate the MMICs from electromagnetic interference (EMI) in the high gain MCMs at high frequencies, i.e., *W*-band.

I proposed using 3D-printed resin housing coated with gold to encapsulate the LNAs, as illustrated in Figure 4.6. The length of the housing cavity is 6 mm, and the width and depth are 3 mm. The proposed housing was adhered on the top grounds of the SIWs and inactive regions to cover each LNA using silver epoxy, and provides light weight and low cost to module packaging and electromagnetic isolation, quasi-hermetization, and mechanical buffering to the LNAs. The measured gain, phase, and NF of the proposed double-LNA module with housing are also illustrated in Figure 4.7 (a), (b), and (c), respectively. It can be found that the proposed housing introduces little degradation to the performance of the double-LNA module.

4.6 Summary

In this chapter, I presented the MCM integration and packaging technologies, i.e., multilayer carrier, laser-drilled cavities, and V-shape wire bonding, and a 50dB gain double-LNA module at *W*-band using a four-circuit layer LCP substrate as a MMIC carrier. The utilized LCP carrier consists of four circuit layers, i.e., the top two for the RF components and the bottom two for the bias circuits. To reduce the wire

bond's inductance, the LNA chip is embedded into a laser-drilled pocket in the top LCP layer. To minimize the mode mismatch between the MS lines on the LCP substrate and LNAs as well as further reduce the wire bond's inductance, V-shape wire bonds are designed to integrate the LNAs with MS lines. The single-LNA module achieves a high gain of more than 26.5 dB from 80 to 100 GHz. In the MCM, SIWs and via barriers are designed to eliminate the undesired substrate modes in carrier substrates, and 3D-printed gold-coated housings are designed to encapsulate the LNAs and isolate them in free space. An impressive gain of 45-52 dB and a low NF of less than 6 dB were demonstrated for the double-LNA module from 80 to 100 GHz. The proposed module also achieves linear phase at the working frequencies.

Chapter 5

SIW FILTER AND DIRECTIONAL FILTER AT W-BAND

The most obvious application of a filter is to reject the unwanted signal frequencies while permitting good transmission of the desired frequencies [80]. According to their spectral response, filters can be classified into different categories, i.e., low-pass, high-pass, band-pass, and band-reject. Their applications can be found in virtually any type of microwave or millimeter wave wireless communication, radar, radiometry, and measurement systems. In the general sense, PCBs serve as the foundation for virtually all these systems. In the printed circuits of these systems, compact filters can be designed on various transmission lines, i.e., MS lines, CPWs, and SIWs. Traditionally, most filters are two-port structures, in which the desired frequencies pass through, and the undesired ones are reflected. However, the strong reflection may introduce many problems, i.e., noise, substrate modes, and oscillation, in the compact mmW systems, particularly for high-gain active applications. To mitigate the reflection, a four-port directional filter has been developed, which can pass the desired frequencies to one port and drop the undesired spectra to another port with low reflection and good isolation at the other two ports. Directional filters have found many applications in the high-gain systems and frequency division multiplexing of wireless communications at microwave frequencies.

In this chapter, I present a SIW-based two-port bandpass filter and a MS-based four-port bandpass directional filter in multilayer LCP substrates, which can be applied to many wireless applications at *W*-band. As presented in Section 3.1, MS

lines and SIWs are the two main transmission lines for the proposed front-end receiving module. Thus, the filter design is based on these two components. This chapter is organized as follows. In Section 5.1, I will discuss the detailed challenges for the printed filters on LCP substrates as well as other substrates at *W*-band. Then, the SIW-based filter and MS-based directional filter will be presented in Section 5.2 and Section 5.3, respectively. This is followed with a summary and conclusion.

5.1 Challenges for *W*-band Filters

In Section 1.2, I have discussed the challenges in materials, fabrication, electromagnetic interference, and measurement for *W*-band frequencies. In this section, I discuss the detailed challenges for the *W*-band filters in multilayer LCP substrates fabricated using commercial large-panel PCB technologies. Under the commercial fabrication standards, the minimum resolution of circuit patterns is 50 μm , and the diameter and pitch of the micro vias are 250 μm and 300 μm , respectively. The via's annular ring is suggested to be 125 μm larger than its hole [9].

Typically, the two-port filters can be designed on MS lines, CPWs, and SIWs. Among these three transmission lines, MS lines and SIWs are of great preference in multilayer printed circuits due to their good electrical shielding. The filters based on MS lines [80] and SIWs [44] have been thoroughly investigated at microwave frequencies. However, their applications for *W*-band frequencies are limited by commercial fabrication resolution. On one hand, the traditional MS line based filters are designed using cascaded half-wavelength impedance steps [80], or half-wavelength and/or quarter-wavelength MS lines with capacitive coupling [80]. The former require narrow line width to achieve high impedance, and the latter need tiny gaps to obtain sufficient coupling at *W*-band, both of which, however, cannot be

fabricated using the commercial large-panel circuit printing technologies. The interdigital filters with vias [80] can be designed with gaps wider than 50 μm between the adjacent MS lines. However, the electrically ‘large’ ring of the vias may change the resonant frequency and short-circuit the neighboring lines. On the other hand, the SIW-based filters can be designed using quarter-wavelength inductive coupling or cascaded cavities with irises [44]. The inductive posts and irises are typically defined using vias, which are practical at low frequencies. However, the diameter and pitch of the vias becomes electrically ‘large’ at *W*-band, which may potentially increase the SIW’s leakage, introduce difficulties to precisely define cavities, and reduce the quality factor of the cavities. Also, the registration tolerance of the vias for the inductive posts and irises may change the center frequency of SIW filters. Compared to the MS-based filters, the SIW-based filters are more robust and practical to the commercial large-panel fabrication technologies at high frequencies. To this end, the SIW-based filters are investigated in this dissertation.

A directional filter is a four-port structure, consisting of one travelling-wave resonator or two standing-wave resonators, terminating lines, and tiny gaps between them to obtain sufficient coupling. It can be designed on MS lines, SIWs, and SLs in printed circuits. The most critical parts of a directional filter are the resonator and the coupling gaps between the resonator and terminating lines. SIWs are not preferable for directional filters due to the fact that their width is too electrically ‘large’ to achieve compact resonators. The SL-based and MS-based direction filters suffer from the low coupling efficiency of the gaps, which aggravated as the frequency increases. As the frequency increases to *W*-band, the traditional directional filters based on MS lines and SLs encounter significant insertion loss and reflection, which is mainly limited by the

commercial fabrication standards. To the best of my knowledge, no directional filters have been reported at *W*-band so far. New topologies have to be invented for the directional filters at *W*-band.

5.2 SIW Filter at 94 GHz

Recently, substrate integrated waveguides have been investigated to substitute for traditional rectangular waveguides in printed circuits at microwave/mmW frequencies, due to their low profile, high density, light weight, and simple packaging. A SIW is a waveguide-like structure fabricated in a dielectric substrate by using two rows of metal vias to connect the top and bottom parallel conductor layers. It preserves most of the advantages of conventional air-filled RWGs, including high quality factor, high power-handling capability, and good electrical shielding. Originating from the planar H-plane RWG filters, SIW filters have gained great interest in the last decade. The SIW filters are superior over the traditional waveguide filters and planar transmission line filters due to the aforementioned benefits. According to the coupling topologies, SIW filters can be classified into four categories: inductive post, iris windows, circular cavities, and rectangular cavities with cross-coupling [44]. Most SIW filters reported so far are designed below 60 GHz [81]-[84], and fabricated on small panels.

The ultimate application of SIW filters and other passive components is in large-scale printed circuits, which becomes dominant in the circuit market due to their low unit cost and high manufacturing speed. However, it has to sacrifice the resolution of the minimum features in the fabrication. According to the commercial standards [9], the vias' pads should be 125 μm larger than their holes, and the diameter and pitch of vias are suggested to be at least 250 μm in the multilayer circuits of the proposed

receiving module, which is large in terms of wavelength at W -band. These commercial standards introduce many detrimental impacts to the design and measurement of SIW filters at high frequencies, as discussed in Section 5.1.

In this section, I present a second-ordered SIW filter, and demonstrate its application on a 100 μ m thick 12 \times 18 inch LCP panel using the state-of-the-art large-panel circuit print technologies. The SIW filter achieves an insertion loss of 1.5 dB at 94 GHz and a passband of 8% centered at 94 GHz.

5.2.1 SIW Filter Design

Differing from traditional RGWs, SIWs can only support TE_{m0} modes due to their electrically ‘small’ substrate thickness in terms of wavelength. For the structure illustrated in Figure 5.1, the fundamental mode of the SIW cavities is TE_{110} mode. The initial cavity dimensions can be determined by setting the resonant frequency of the TE_{110} mode equal to the center frequency of the desired passband, as described by the following formula:

$$f_0 = \frac{c_0}{2\sqrt{\epsilon_r}} \sqrt{\left(\frac{1}{W - d^2/0.95p}\right)^2 + \left(\frac{1}{L - d^2/0.95p}\right)^2}, \quad (5.1)$$

where ϵ_r is the dielectric constant, W and L are the SIW cavity’s width and length, d is the diameter of the vias, and p is the pitch size between two contiguous vias.

In this section, simple topologies and low orders are employed for the SIW filter, which are robust in my view with respect to the commercial state-of-the-art PCB manufacturing, to investigate application possibility of SIW filters in large scale printed circuits at W -band. The diameter and center-to-center pitch of vias are $d = 250$ and $p = 300$ μ m, respectively, which could be utilized in a multilayer substrate with a

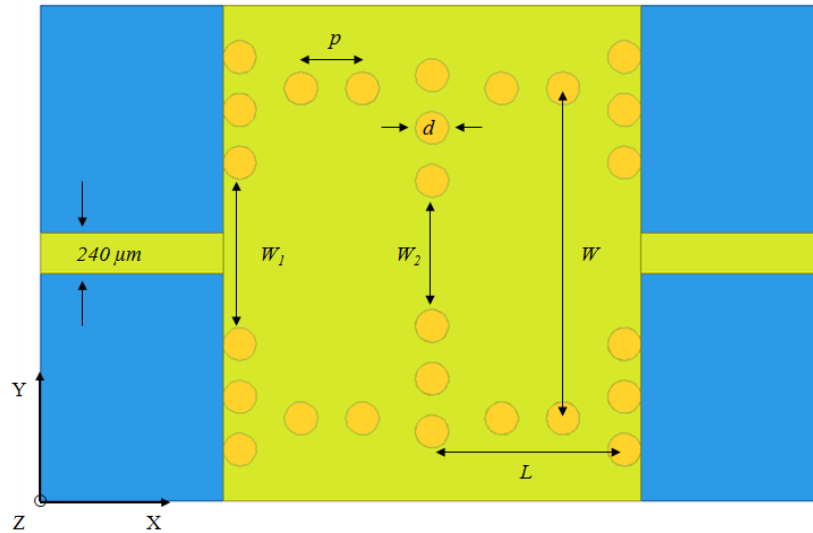
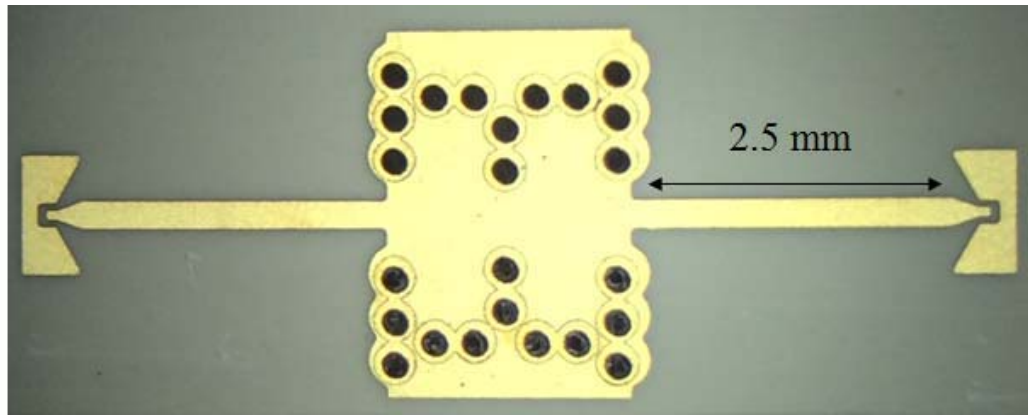
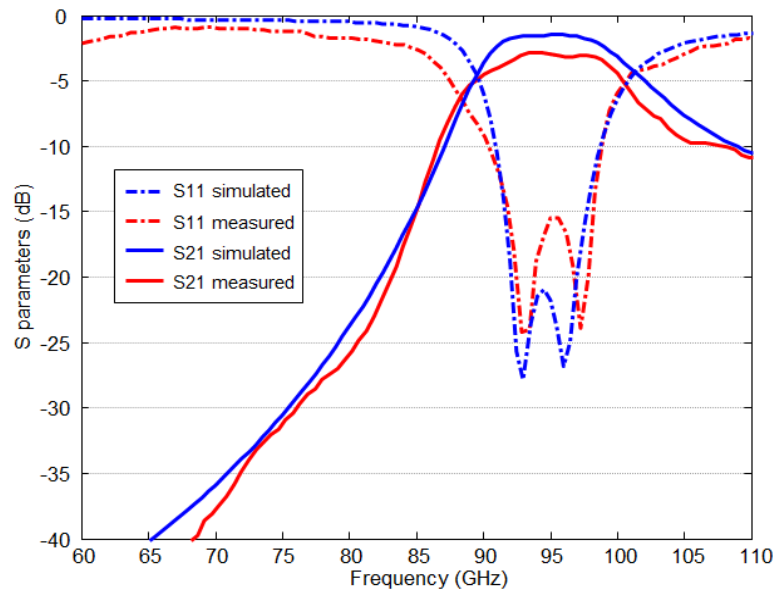


Figure 5.1. Configuration of the second-order SIW filter fed by MS lines.

thickness of $200\ \mu\text{m}$. The filter is second-ordered using one iris window as a coupling element and two MS lines as feeds. The cavities and windows are carefully defined using laser-drilled vias. Ansys HFSS was employed to design a full-wave model for the proposed filter, as illustrated in Figure 5.1, and tune the cavity dimensions to optimize the insertion loss and center frequency of the filter. To attain an impedance of $50\ \Omega$, the width of the MS lines is chosen as $240\ \mu\text{m}$, and the length and width of the two identical cavities are 2 and 0.9 mm, respectively. The widths of the feed window, W_1 , and iris window, W_2 , are 0.96 and 0.8 mm, respectively. Figure 5.2 (b) illustrates the simulated S-parameters of the second-order SIW filter. It can be found that the 3dB passband is from 90.8 to 98.5 GHz, and the insertion loss is 1.5 dB at 94 GHz. The stopband attenuation is 36 and 11 dB at 70 and 110 GHz, respectively. The out-of-band attenuation could be improved by cascading additional cavities.



(a)



(b)

Figure 5.2. (a) Fabricated second-order SIW filter, and (b) simulated and measured S-parameters of the SIW filter.

5.2.2 Measurement

The fabricated SIW filter is illustrated in Figure 5.2 (a). It comprises two identical cavities constructed with only twenty four vias and two MS lines terminated with a pair of low-loss CBCPW probe pads. The design and measurement of the probe pads have been presented in Section 3.3.2. The measurement set-up and calibration method discussed in Section 3.2 were employed for the characterization of this filter. Figure 5.2 (b) illustrates the measured S-parameters. It can be seen that the measured insertion loss is 2.6 dB at 94 GHz, including the two probe pads' loss, and the 3dB bandwidth is from 90.8 to 98.5 GHz. As can be found in Figure 3.8 (c), the averaged insertion loss of a pair of CBCPW probe pads is approximately 0.8 dB at 94 GHz. Thus, the true loss of the fabricated filter is 1.8 dB, showing little discrepancy with the simulated loss. The out-of-band rejection is 36 dB at 70 GHz and 11 dB at 110 GHz, respectively. The simulated and measured S-parameters are in good agreement, which demonstrates that the SIW filter can be utilized in large-panel printed circuits.

5.3 Directional Filters at 95 GHZ

Directional filters (DFs) have gained tremendous interest in the application of frequency division multiplexing (FDM) in wireless communication systems. They can act either as channel combiners or channel separators. Superior over the other multiplexers, the DFs address miniaturization and low reflection. Various DFs have been devised since the 1960s, however, a limited number of them have found practical applications. Figure 5.3 illustrates the most useful types of the reported DFs. Ideally, a broadband signal fed into *Port 1* of the DFs will be isolated at *Port 4*, the desired spectrum will be dropped to *Port 3*, and the signal at the undesired frequencies will travel to *Port 2*, with no reflection at *Port 1* [80]. According to this mechanism,

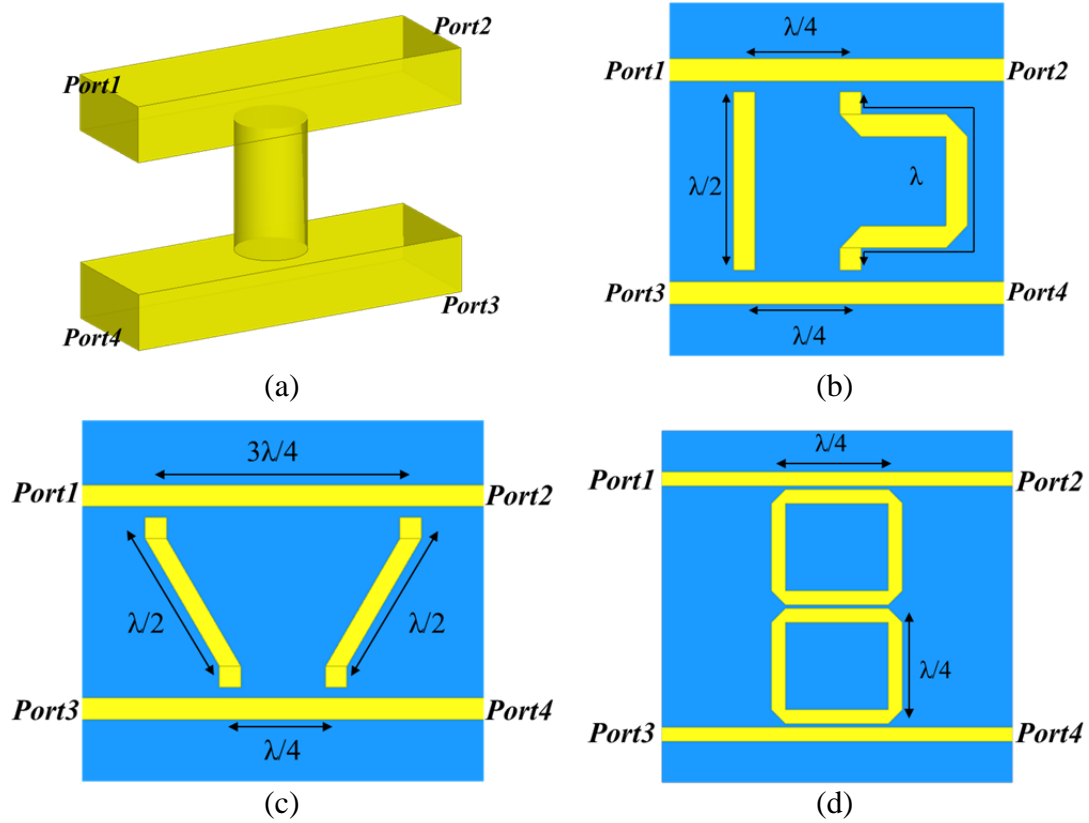


Figure 5.3. Traditional directional filters: (a) waveguide-based, (b) standing-wave I, (c) standing-wave II, and (d) travelling-wave.

directional filters can be classified into three categories: waveguide-based DFs [85], standing-wave DFs [86]-[90], and travelling-wave DFs [90]-[96]. The waveguide-based DF comprises two rectangular waveguides and one cylindrical direct-coupled cavity resonator, as depicted in Figure 5.3 (a). Typically, it is bulky and heavy, and has a narrow bandwidth of less than 2 percent due to the high quality factor of the waveguide structures [80] [85]. Figures 5.3 (b) and (c) illustrate two types of standing-

wave DFs with essentially the same frequency response. Each of them has two standing-wave resonators between two terminating lines, and can provide several percent bandwidth [86]-[90]. However, very tiny coupling gaps between the resonators and terminating lines are critically required to provide sufficient coupling, which is extremely challenging for the commercially available circuit print technologies, particularly at high frequencies. The travelling-wave DF comprises one or several travelling-wave loop resonators and two terminating lines [90]-[96], as illustrated in Figure 5.3 (d). The resonators and terminating lines are coupled by means of quarter-wavelength directional couplers. 3dB passband width on the order of several percent can be achieved by using multiple loops [80] [92]. However, the travelling-wave DFs suffer from the same fabrication tolerance problem as the standing-wave DFs as the frequency increases.

To the best of my knowledge, all the reported DFs are designed below 40 GHz [86]-[96]. As the frequency increases, it becomes increasingly critical to obtain sufficient coupling between the resonators and terminating lines with planar structures [86]-[89] [91]-[94]. To this end, multilayer directional couplers were introduced to construct DFs [90] [95]-[96]. In these structures, the resonators and terminating lines are overlapped vertically, which can enhance the coupling, but also introduce large insertion loss and reflection. The insertion losses of the multilayer DFs in Ref. [90] [95] and [96] are reported as high as 5 dB and 4 dB at 6 GHz and 2.9 dB at 38 GHz. The coupling efficiency of the traditional multilayer quarter-wavelength directional coupler is strongly limited by the thickness of the substrates. Thus, it is challenging to scale the reported multilayer DFs to higher frequencies.

In this section, I present a new type of travelling-wave DF fabricated using multilayer liquid crystal polymer (LCP) substrates at 95 GHz. It comprises two dual-slot directional couplers and one two-wavelength long loop resonator. The proposed filter is superior to the traditional symmetric travelling-wave DF by using asymmetric loop phase topology and the developed dual-slot directional couplers. To improve the directivity and reduce the insertion loss, cascaded DFs were also designed and characterized. The proposed DFs have no critically sized features, and were fabricated on 12×18 inch LCP panels by using commercial large-scale circuit print technologies. This section is organized as follows. Section 5.3.1 will discuss the proposed dual-slot directional coupler. Then, the design of the single-loop and cascaded double-loop DFs in LCP multilayer substrates will be depicted in Section 5.3.2. Section 5.3.3 will present the hybrid substrates, measurement setup, and measured results of the proposed DFs.

5.3.1 Directional Coupler Design

The traditional travelling-wave DF comprises loop resonators and quarter-wavelength directional couplers [90]-[92] [94]-[96], as illustrated in Figure 5.3 (d). The couplers can be designed either using planar parallel lines with very narrow coupling gaps or vertically parallel lines in multilayer thin substrates. Reference [97] reported a directional coupler based on double-sided MS lines coupled through a slot with a length of quarter wavelength in the shared ground in multilayer substrates. However, these reported structures are not suitable for high-frequency applications due to the aforementioned problems of the reflection and coupling efficiency.

Inspired by the multi-hole rectangular waveguide coupler [11], we designed a new type of dual-slot MS line based directional coupler in three-layer LCP substrates.

The proposed directional coupler comprises two parallel MS lines on the top and bottom layers, respectively, a shared ground in the inner layer, and two rectangular slots distributed in the ground with a pitch of a quarter wavelength of the MS lines.

5.3.1.1 Slot coupling of the vertically overlapped MS lines

To understand how the proposed directional coupler operates, the coupling mechanism of two vertically overlapped MS lines is first investigated. Its configuration and electric fields along the propagation direction of the guided wave are illustrated in Figure 5.4 (a). According to Ref. [11], for a signal sent into *Port 1*, it can excite an even mode to *Port 4* and an odd mode to *Port 3*. For the even mode, the electric field is evenly symmetric according to the center line, thus no current flows between the two MS lines. For the odd mode, the field shows an odd symmetry, and a voltage null exists between the two strip conductors. Thus, these two modes propagate in opposite directions. The equivalent circuit models of these two modes are also illustrated in Figure 5.4 (a). C_{12} represents the coupling capacitance between the top and bottom MS lines, and C_{11} and C_{22} represent the capacitances of these two lines to the shared ground. Due to the small coupling slot, the capacitance (C_{12}) is not significant, and, thereby, the even and odd modes have similar amplitude.

Ansys HFSS was employed to design and simulate the full-wave models of the vertically coupled MS lines and the following devices. As illustrated in Figure 5.4 (a), the bond-ply is a 50 μm thick LCP, and the top and bottom LCP core layers are 100 and 50 μm , respectively. The dielectric constant and loss tangent of LCP are 3.2 and 0.0045 at 95 GHz, respectively, as reported in Ref. [8]. The top MS line has a length of 5 mm and a width of 0.24 mm, providing an impedance of 50 Ω for probing. A narrower width of 0.16 mm is chosen for the bottom MS lines to suppress the

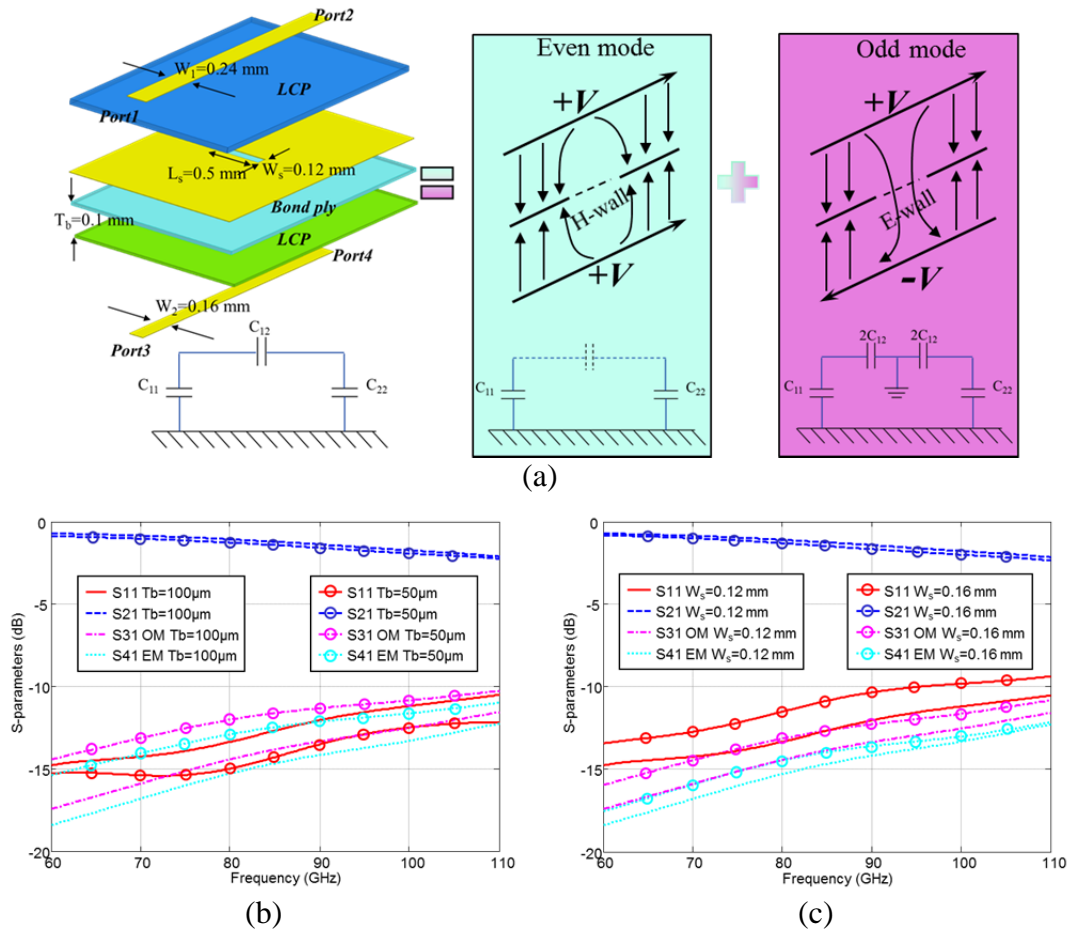


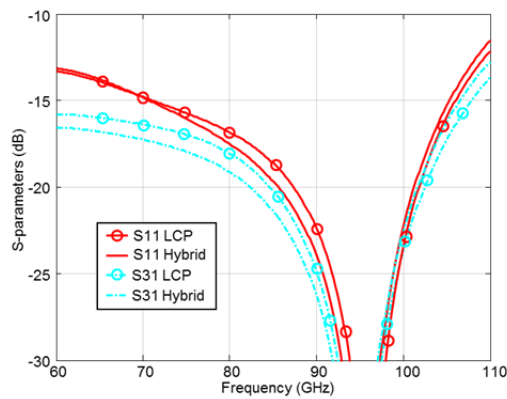
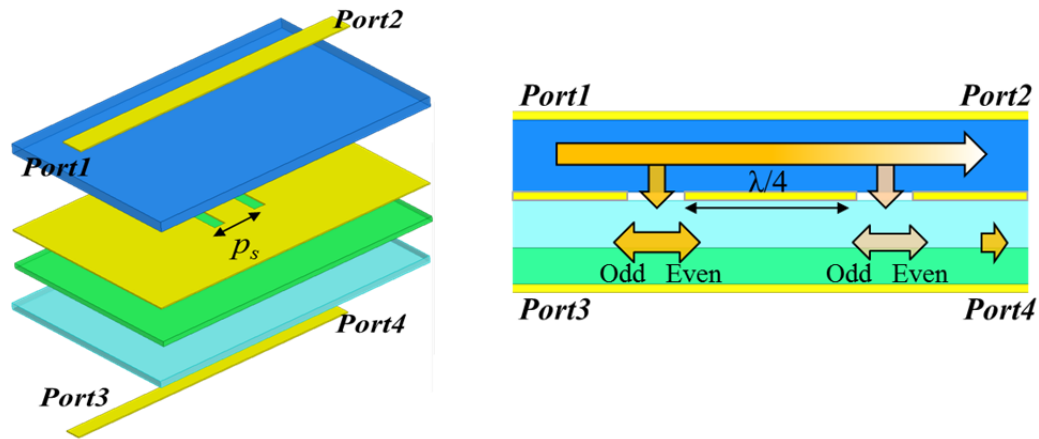
Figure 5.4. (a) Configuration, electric fields, and equivalent circuit models of the slot-coupled vertically overlapped MS lines, and simulated S-parameters of the slot-coupled MS lines with (b) different LCP thickness and (c) slot size.

dispersion of the loop resonator [8] [71] in the DFs. As can be seen in Figure 5.4 (a), S_{31} and S_{41} represent the odd mode and even mode, respectively, due to the same propagation directions. Tolerance analysis of the substrate thickness and slot size is illustrated in Figure 5.4 (b) and (c). The total thickness of the bond-ply and bottom

LCP is denoted as T_b . As can be seen in Figure 5.4 (b), using a thin substrate can enhance the coupling efficiency. At $T_b = 50 \mu\text{m}$, the simulated S_{31} and S_{41} are 1.8 dB higher than their counterparts at $T_b = 100 \mu\text{m}$. However, the MS lines on a $50\mu\text{m}$ thick LCP substrate have significant propagation loss [8], which is not suitable for practical applications. Increasing the size of the coupling slot can also enhance the coupling efficiency, however, significantly increasing the reflection, as illustrated in Figure 5.4 (c). It should be noted that a large slot introduces large discrepancy between the even mode and odd mode, which can be explained by the equivalent circuit models in Figure 5.4 (a). The odd mode is controlled by C_{11} , C_{22} , and C_{12} , while the even mode is determined by C_{11} and C_{22} . Enlarging the slot can increase C_{12} , thus enhancing the odd mode faster than the even mode. When the slot width, W_s , equals a quarter wavelength, the traditional slot-coupled directional coupler reported in Ref. [97] can be achieved, however, whose reflection is significant at W -band. Based on the aforementioned analysis, to compensate for MS line's loss, reflection, and coupling efficiency, T_b is chosen as $100 \mu\text{m}$, and the width, W_s , and length, L_s , of the slot are 0.12 and 0.5 mm, respectively. The simulated magnitude of the even mode, S_{41} , and odd mode, S_{31} , is -13.6 and -12.9 dB at 95 GHz, respectively, and the reflection, S_{11} , is less than -12 dB from 70 to 100 GHz.

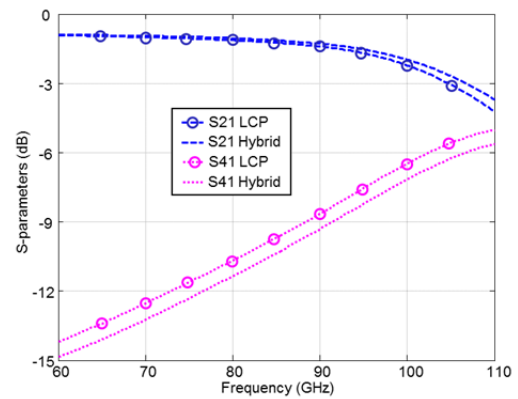
5.3.1.2 Dual-slot directional coupler

The configuration and mechanism of the proposed directional coupler are illustrated in Figure 5.5 (a). It consists of two coupling slots in a shared ground with a phase delay of 90° and an optimized distance of $p_s = 3.4$ mm along the propagation direction of the guided wave. Due to the weak coupling of the slots, the two even modes and two odd modes excited by these two slots have similar amplitude. The two



(b)

(a)



(c)

Figure 5.5. (a) Configuration, (b) simulated S11 and S31, and (c) simulated S21 and S41 of the directional coupler in LCP substrates and hybrid substrates.

even modes, propagating toward *Port 4*, are in-phase at the second slot, thus adding constructively, while the two odd modes, propagating towards *Port 3*, are 180° out-of-phase at the first slot, thus providing a high isolation, as depicted in Figure 5.5 (a). The simulated S-parameters of the dual-slot directional coupler are illustrated in Figures

5.5 (b) and (c), showing good directivity. It can be seen that S_{41} is -7.5 dB, S_{31} is less than -30 dB, and S_{11} is less than -30 dB at 94 GHz. Due to the high directivity, the proposed directional coupler can be utilized to design directional filters.

5.3.2 Directional Filter Design

Another key element to construct a travelling-wave DF is the loop resonator. The traditional DFs utilize loop resonators with a mean circumference of one wavelength at its center frequency [90]-[96], which is not suitable for high frequencies. As the frequency increases to *W*-band, i.e., 95 GHz, the widths of MS lines and coupling slots become electrically ‘large’ in terms of wavelength. In this case, the one wavelength loop resonator cannot provide enough space to combine with the proposed dual-slot directional filter efficiently. Meanwhile, the limited loop length of a one wavelength loop with ‘large’ line width may increase mutual coupling between the MS lines in the loop, thus reducing the resonator’s Q-factor. To mitigate this problem, the mean circumference of the loop resonator is chosen as two wavelengths of the MS line at 95 GHz. The configuration of the utilized loop resonators is illustrated in Figure 5.6 (a). Its mean length and width are 1.32 mm and 0.71 mm, respectively. The width of the bottom MS line is 0.16 mm, providing an impedance of 62 Ω to suppress the dispersion of the loop resonator. Figure 5.7 illustrates the simulated effective dielectric constant and propagation loss of the MS lines with a width of 160 μm . It can be seen that their propagation loss is 0.156 dB/mm at 95 GHz. The simulated unloaded Q-factor of the loop resonator is 58 at 95 GHz, which can be calculated using the methods reported in Ref. [8] and [71]. Then, the corresponding averaged attenuation of the loop resonator can be calculated as 0.226 dB/mm, including the radiation loss and propagation loss of the loop line [71]. The averaged radiation loss can be obtained

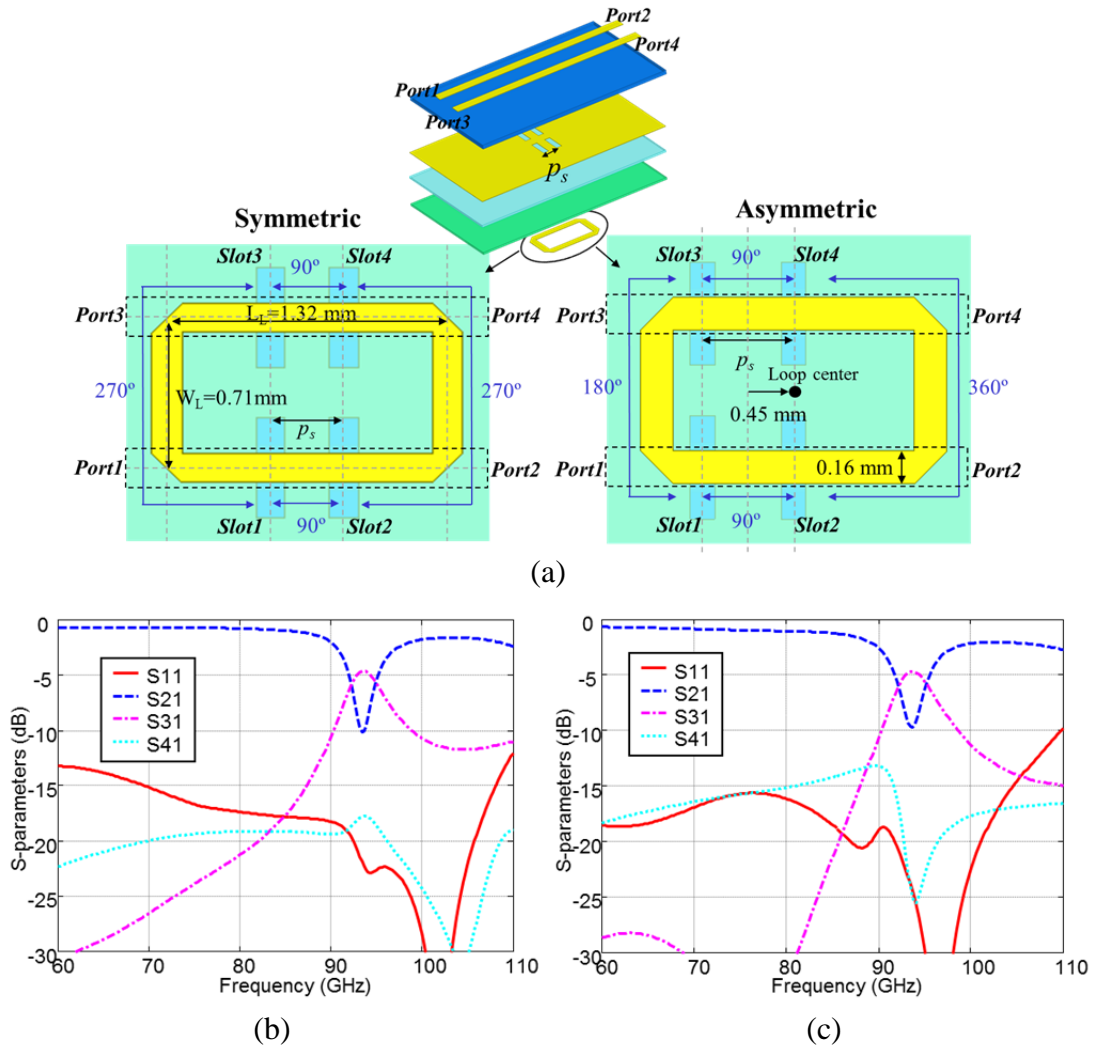


Figure 5.6. (a) Configuration of the single-loop DFs with symmetric and asymmetric loop topologies in multilayer LCP substrates, and simulated S-parameters of the (b) symmetric and (c) asymmetric DFs with $p_s = 0.35$ mm.

by subtracting the propagation loss illustrated in Figure 5.7 (b) from the total loss. The estimated radiation loss is approximately 0.065 dB/mm at 95 GHz, which is not significant with respect to the total loss.

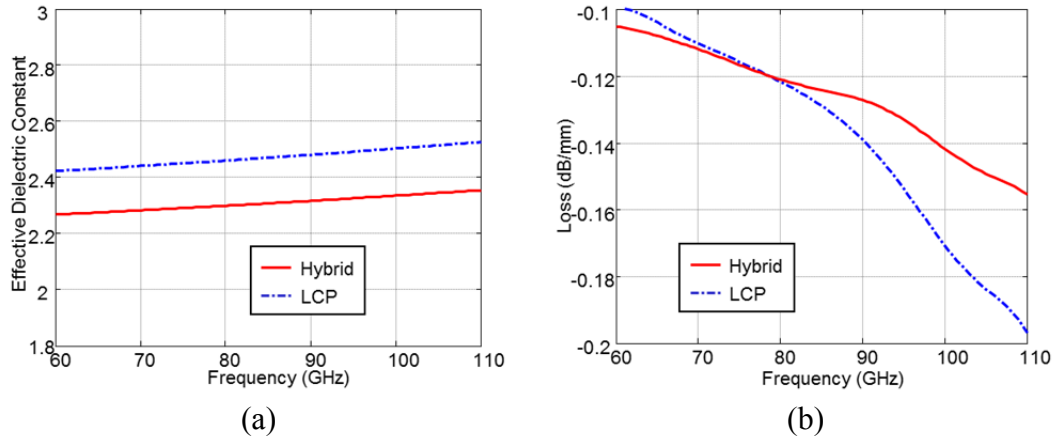


Figure 5.7. Simulated (a) effective dielectric constant and (b) loss of MS lines with a width of $160\ \mu\text{m}$ on a $100\ \mu\text{m}$ LCP substrate and a $50\ \mu\text{m}$ LCP substrate laminated with a $66\ \mu\text{m}$ AG bond-ply.

5.3.2.1 Single-loop directional filter

5.3.2.1.1 Symmetric loop

I first investigated a DF with a symmetric loop, which is typically utilized for the traditional travelling-wave DFs [90]-[96], as illustrated in Figure 5.6 (a). According to the directional coupler's mechanism aforementioned in Section 5.3.1, the signal input to *Port 1* will be dropped at *Port 3*, and isolated at *Port 4* at 94 GHz. The pitch between the two coupling slots, p_s , is optimized to 0.35 mm, instead of 0.34 mm, to achieve a higher directivity for the DF. Figure 5.6 (b) illustrates the simulated S-parameters of the proposed symmetric DF. The insertion loss of the passband, S_{31} , is -4.6 dB at *Port 3* at 94 GHz, and the 3dB bandwidth is 5.3% centered at 94 GHz. It should be noted that the through loss, S_{21} , is as high as -9.5 dB, which is limited by

the coupling efficiency, and can be reduced by cascading directional filters. The isolation, S_{41} , and reflection, S_{11} , are better than -17 dB at 94 GHz at *Port 4* and *Port 1*, respectively.

However, the symmetric loop reduces the directivity of the DF inherently. As can be seen in Figure 5.6 (a), the phase between *Slot 1* and *Slot 2* and between *Slot 3* and *Slot 4* is approximately 90° , and the phase between *Slot 1* and *Slot 3* and between *Slot 2* and *Slot 4* is 270° . With such a phase distribution, the signals transmitted from *Port 1* to *Port 3* in the clockwise and anti-clockwise directions are 180° out of phase, which actually degrades the directivity.

5.3.2.1.2 Asymmetric loop

To improve the directivity of the DF, I proposed an asymmetric loop topology, as depicted in Figure 5.6 (a). This asymmetric phase topology is similar to that of the standing-wave DF [88] in Figure 5.3 (b). The center of the loop is shifted by a factor of 0.45 mm with respect to the slots. In this case, the phase between *Slot 1* and *Slot 3* and between *Slot 2* and *Slot 4* becomes approximately 180° and 360° , respectively. With such a phase distribution, the signals transmitted from *Port 1* to *Port 3* in the clockwise and anti-clockwise directions are constructive, and the counterparts from *Port 1* to *Port 2* and from *Port 1* to *Port 4* are 180° out of phase, thus improving the directivity of the DFs. The simulated S-parameters of the asymmetric single-loop DFs are illustrated in Figure 5.6 (c). The 3dB bandwidth of the passband is reduced from 5.3% to 4.9%, the out-of-band rejection is improved more than 5 dB, and the isolation and reflection are also improved dramatically.

5.3.2.2 Double-loop directional filter

Typically, to improve the directivity and the insertion loss, the travelling-wave DFs may cascade multiple loop resonators [92], as illustrated in Figure 5.3 (d), and the standing-wave DFs can cascade the identical DFs along the terminating lines [88]. Here, I cascade two identical single-loop DFs in the direction of the terminating lines with the same topology for the standing-wave DFs, as illustrated in Figure 5.8 (a). The *Port 1* and *Port 3* of the second DF connect to the *Port 2* and *Port 4* of the first DF, respectively. The S_{21} and S_{41} of the first DF will travel to the second DF as the input signals, and can be depicted by the following formula:

$$\begin{aligned} S'_{in} &= S_{21}^1 e^{-j\theta} \\ S''_{in} &= S_{41}^1 e^{-j\theta}, \end{aligned} \quad (5.2)$$

where S_{21}^1 and S_{41}^1 are the through and isolated signals of the first DF, respectively, θ is the phase delay between two DFs, and S'_{in} and S''_{in} are the input signal to the *Port 1* and *Port 3* of the second DF, respectively. Due to the symmetry of the proposed DF, the S-parameters satisfy the following relationships:

$$\begin{aligned} S_{21}^1 &= S_{12}^1 = S_{34}^1 = S_{43}^1 \\ S_{41}^1 &= S_{23}^1. \end{aligned} \quad (5.3)$$

Both S'_{in} and S''_{in} will be filtered using the same mechanism. Thus, the fundamental response of the second DF will be the overlapped responses of these two signals:

$$\begin{aligned} S_{11}^2 &= S'_{in} S_{11}^1 + S''_{in} S_{31}^1 = (S_{21}^1 S_{11}^1 + S_{41}^1 S_{31}^1) e^{-j\theta} \\ S_{21}^2 &= S'_{in} S_{21}^1 + S''_{in} S_{41}^1 = (S_{21}^1 S_{21}^1 + S_{41}^1 S_{41}^1) e^{-j\theta} \\ S_{31}^2 &= S'_{in} S_{31}^1 + S''_{in} S_{11}^1 = (S_{21}^1 S_{31}^1 + S_{41}^1 S_{11}^1) e^{-j\theta} \\ S_{41}^2 &= S'_{in} S_{41}^1 + S''_{in} S_{21}^1 = 2S_{21}^1 S_{41}^1 e^{-j\theta}. \end{aligned} \quad (5.4)$$

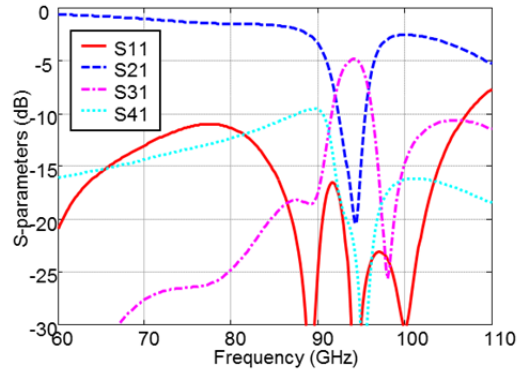
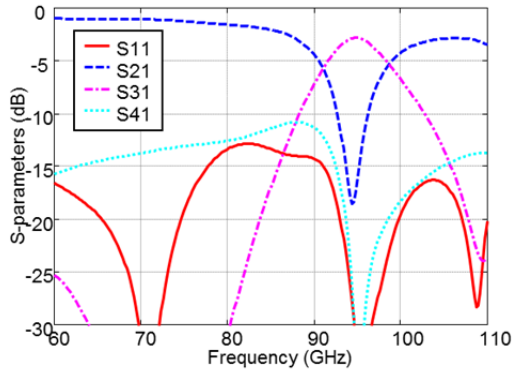
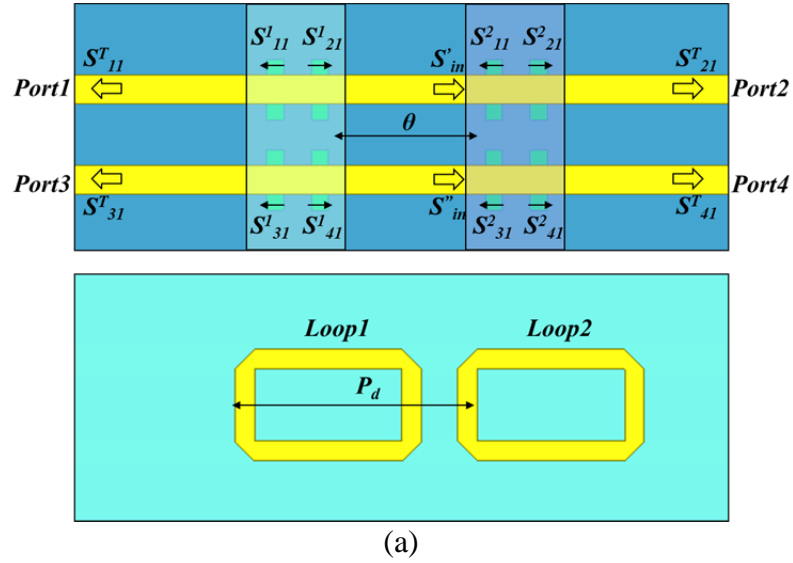


Figure 5.8. (a) Configuration of the cascaded double-loop DF with asymmetric loops, and simulated S-parameters of the cascaded DF with $P_d =$ (b) 1.9 mm and (c) 2.3 mm.

S_{11}^2 and S_{31}^2 will be fed back to the first DF, part of which will contribute to S_{11}^T and S_{31}^T and the rest of which will be reflected back to the second DF as the high-order mutual coupling between the two DFs. As can be found in Figure 5.6 (c), the S_{11}^1 , S_{21}^1 ,

and S_{41}^1 of the single-loop DF are less than -20 dB, -10 dB, and -17 dB at 95 GHz, respectively. Therefore, it is fair to neglect the high-order mutual coupling and high-order items, simplifying our analysis. The S-parameters of the cascaded double-loop travelling-wave DF can be described as follows:

$$\begin{aligned}
S_{11}^T &\approx S_{11}^1 + S_{11}^2 e^{-j\theta} S_{12}^1 + S_{31}^2 e^{-j\theta} S_{14}^1 \\
&= S_{11}^1 + S_{21}^1 (S_{21}^1 S_{11}^1 + S_{41}^1 S_{31}^1) e^{-j2\theta} + S_{41}^1 (S_{21}^1 S_{31}^1 + S_{41}^1 S_{11}^1) e^{-j2\theta} \\
&\approx S_{11}^1 + 2S_{21}^1 S_{41}^1 S_{31}^1 e^{-j2\theta} \\
S_{21}^T &\approx S_{21}^2 = (S_{21}^1 S_{21}^1 + S_{41}^1 S_{41}^1) e^{-j\theta} \\
S_{31}^T &\approx S_{31}^1 + S_{31}^2 e^{-j\theta} S_{34}^1 + S_{11}^2 e^{-j\theta} S_{32}^1 \\
&= S_{31}^1 + S_{21}^1 (S_{21}^1 S_{31}^1 + S_{41}^1 S_{11}^1) e^{-j2\theta} + S_{41}^1 (S_{21}^1 S_{11}^1 + S_{41}^1 S_{31}^1) e^{-j2\theta} \\
&\approx S_{31}^1 + S_{21}^1 S_{21}^1 S_{31}^1 e^{-j2\theta} + S_{41}^1 S_{41}^1 S_{31}^1 e^{-j2\theta} \\
S_{41}^T &\approx S_{41}^2 = 2S_{21}^1 S_{41}^1 e^{-j\theta}.
\end{aligned} \tag{5.5}$$

It is noted that the S-parameters of the cascaded DFs have periodic characteristics, which are controlled by the phase delay, θ , between them. S_{31}^T is maximum at $\theta = n\pi$ (n is an integer) and minimum at $\theta = (2n+1)\pi/2$. Limited by the loop dimensions, $\theta = 2\pi$ is chosen to reduce the insertion loss, which corresponds to $P_d = 1.9$ mm. The simulated S-parameters of the cascaded double-loop DF with $P_d = 1.9$ mm are illustrated in Figure 5.8 (b). Superior to the single-loop DFs, the insertion loss, S_{31} , is improved to 2.6 dB, and the through loss, S_{21} , is reduced to -17 dB at 94 GHz. The isolation is better than -20 dB at 95 GHz, and the reflection is less than -11 dB at W -band. Due to the weak disturbance coupling between the two DFs, the 3dB bandwidth of the passband is broadened to 8%. Tuning the phase delay can also introduce two transmission zero points to sharp the passband. As the frequency deviates from the center frequency, the item $S_{21}^1 S_{21}^1 + S_{41}^1 S_{41}^1$ for S_{31}^T in Equation (5.5) approaches one.

Thus, at $\theta \approx (2n+1)\pi/2$, two transmission zero points can be introduced to S_{31}^T . The simulated S-parameters of the double-loop DF with $P_d = 2.3$ mm and $\theta = 5\pi/2$ are illustrated in Figure 5.8 (c). The passband width is reduced to 4% centered at 94 GHz with an increased insertion loss of 4.8 dB.

5.3.3 Hybrid Substrates and Measurement

5.3.3.1 Hybrid substrates

To improve the yield for large panel lamination [9], the manufacturer suggests using 66 μ m (2.6mil) thick Arlon GenClad (AG) 280 bond-ply [98] as a substitute to the LCP bond-ply. Consequently, we have to adapt the directional couplers and filters in the hybrid substrates. The dielectric constant and loss tangent of the AG bond-ply at 95 GHz is approximately 2.82 and 0.005, respectively, which can be calculated using classic ring resonator method and transmission line method reported in Ref. [71]. As can be seen in Figure 5.7, using AG bond-ply slightly reduces the effective dielectric constant and propagation loss of the MS lines. To maintain the same resonant frequency, the pitch between slots, p_s , is increased to 3.7 mm, and the length and width of the loop are slightly increased to 1.35 mm and 0.745 mm, respectively. The unloaded Q-factor and the averaged radiation loss of the loop resonator in the hybrid substrates are similar to their counterparts in LCP substrates. The AG bond-ply slightly increases the MS line's impedance from 62 to 67 Ω , which is preferable to suppress the dispersion of the loop resonator. The drawback of the hybrid substrates is the slightly-reduced coupling efficiency of the slot-coupled double-sided MS lines, which is due to the fact that AG bond-ply with low dielectric constant (2.82) and large thickness (66 μ m) reduces C_{21} and C_{22} . The simulated S-parameters of the directional

couplers in the hybrid substrates are illustrated in Figure 5.5 (b) and (c). The insertion loss, S_{41} , is -8.2 dB at *Port 4*, and the isolation, S_{31} , is better than -30 dB at *Port 3* at around 95 GHz. The coupling efficiency is 0.7 dB lower than that in the LCP substrates at 95 GHz, which may slightly increase the loss of DFs in hybrid substrates. The HFSS models of the DFs are modified and re-simulated with an AG bond-ply as a reference for the measured data.

5.3.3.2 Measurement set-up and W-band load

The measurement setup and calibration method discussed in Section 3.2 were utilized to characterize the MS-to-SIW transition. To probe the DFs, via-less CBCPW probe pads presented in Section 3.3.2 were utilized to connect the terminating MS lines. These probe pads achieve low loss and low reflection at W-band.

To characterize the proposed four-port structures, two ports are probed, while the remaining two ports should be terminated with perfect loads. However, the commercially available state-of-the-art 50 Ω resistors can only function up to 50 GHz. Beyond 50 GHz, these resistors become inductive, and, thus, cannot serve as perfect loads. To improve the load performance, we attached RF absorbers onto the MS lines to attenuate the reflection. CBCPW probe pads terminated MS lines were integrated with 50 Ω resistors and high-loss RF absorbers to investigate the reflection. The utilized resistors are S0402AF from State of the Art Inc. [99], and the absorber material is C-RAM GDSS from Cuming Microwave Corp. [100]. With only the resistor load, the reflection is as strong as -4 dB at W-band. With a 10mm long RF absorber, the reflection is less than -14 dB. With both absorber and resistor, the reflection can be suppressed down to less than -17 dB at W-band.

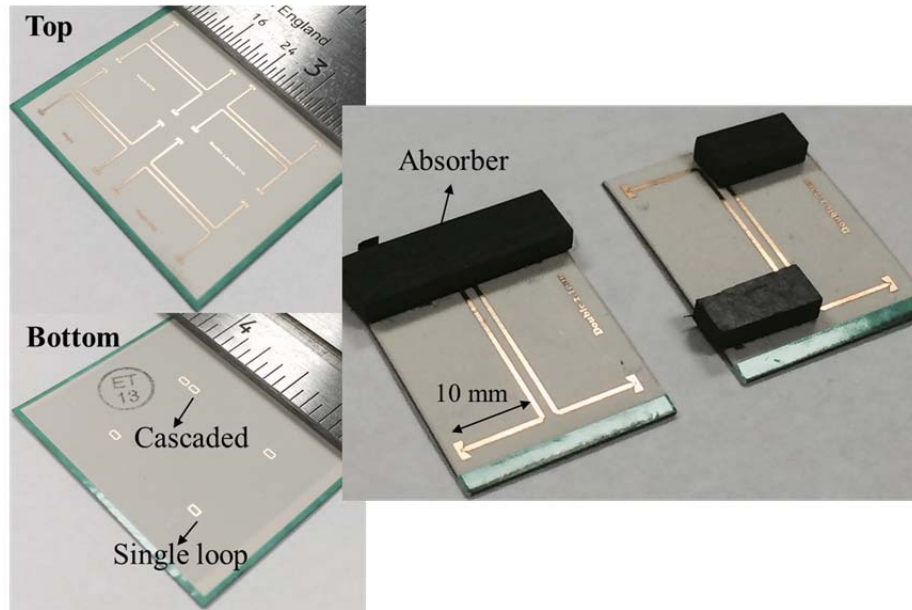


Figure 5.9. Fabricated single-loop and cascaded DFs with RF absorbers.

Table 5.1. Material properties of the substrates and dimensions of the HFSS models and fabricated devices

Parameters	HFSS	Fabricated	Parameters	HFSS	Fabricated
W_l	0.24 mm	0.228 mm	$\epsilon_r (LCP)$	3.2	
W_2	0.16 mm	0.15 mm	$\tan\theta (LCP)$	0.0045	
W_s	0.12 mm	0.126 mm	$\epsilon_r (AG)$	2.82	
L_s	0.5 mm	0.508 mm	$\tan\theta (AG)$	0.005	
T_{copper}	17 μm	17 \pm 3 μm	T_{AG}	66 μm	62-67 μm

5.3.3.3 Measured S-parameters

The fabricated single-loop and cascaded DFs are illustrated in Figure 5.9. The material properties utilized in the HFSS simulation and the dimensions of the HFSS modules and fabricated devices are listed in Table 5.1, revealing a small fabrication

tolerance. During the measurement, different ports of the DFs were terminated properly to characterize the corresponding S-parameters. To simplify the load switch for the two terminated ports, we utilized 10mm long RF absorbers to attenuate the reflection. The reflection from these two terminated ports is approximately -16 dB at 95 GHz, which will slightly affect the measured S-parameters of the proposed DFs. In the practical application, both resistors and absorbers may be required to eliminate the reflection.

5.3.3.3.1 Single-loop DFs

The simulated and measured S-parameters of the asymmetric single-loop DF in the hybrid substrates are illustrated in Figure 5.10 (a), showing good agreement. It can be seen that the measured insertion loss of the passband is 5.2 dB at 95 GHz, and the 3dB bandwidth is 4.8% centered at 95 GHz. The isolation is better than -17 dB, and the reflection is lower than -16 dB at 95 GHz. Limited by the coupling efficiency of the directional coupler, the through signal, S_{21} , is approximately -9 dB at 95 GHz. In this case, the through signal can be fed into another DF to reduce the through loss. The measured out-of-band rejection of the passband is slight higher than the simulated result, which may be attributed to the reflection from the terminated ports attached with RF absorbers.

5.3.3.3.2 Cascaded double-loop DFs

The simulated and measured S-parameters of the cascaded DFs in the hybrid substrates are illustrated in Figures 5.10 (b) and (c). By cascading two DFs, the insertion loss (S_{31}), isolation (S_{41}), and through loss (S_{21}) can be improved significantly with a cost of slightly increased bandwidth and reflection. At $P_d = 1.9$ mm, the

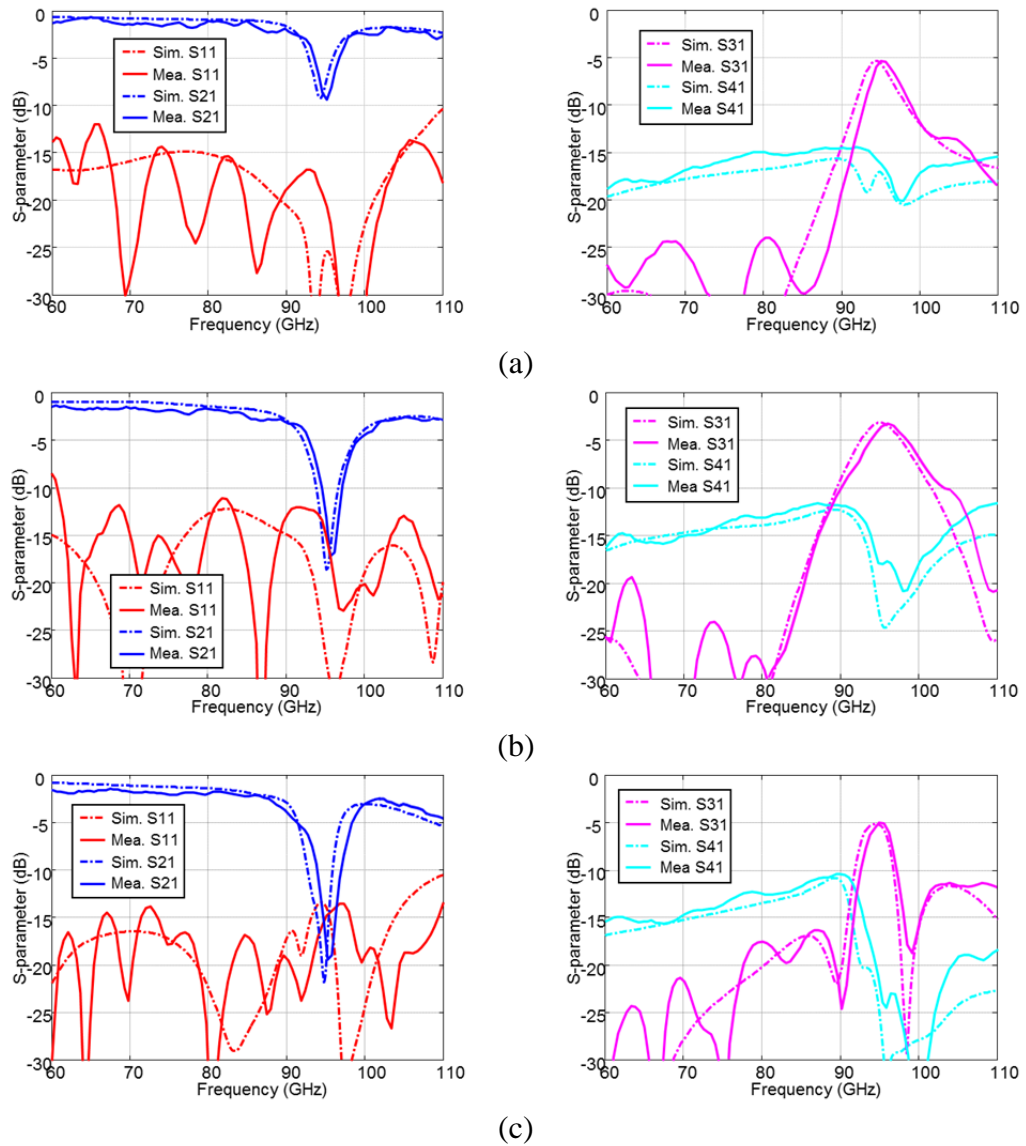


Figure 5.10. Measured and simulated S-parameters of (a) the asymmetric single-loop DF with $p_s = 0.37$ mm and cascaded double-loop DFs with $P_d =$ (b) 1.9mm and (c) 2.3 mm.

corresponding phase delay θ between two DFs is 2π . The measured insertion loss of

Table 5.2. Insertion loss, bandwidth, and out-of-band rejection of the directional filters.

Sub.	Config.	P_d (mm)	loss (dB)	BW	Rejection (dB)
LCP	S. Sym.		4.6	5.8%	-25(L)/-11(H)
Hybrid	S. Sym.		5.3	6%	-27(L)/-12(H)
LCP	S. Asym.		4.6	4.9%	-30(L)/-14(H)
Hybrid	S. Asym.		5.2	4.8%	-30(L)/-16(H)
LCP	D. Asym.	1.9	2.5	8%	-27(L)/-23(H)
Hybrid	D. Asym.	1.9	3.16	7.8%	-40(L)/-26(H)
LCP	D. Asym.	2.3	4.8	4.2%	-20(L)/-11(H)
Hybrid	D. Asym.	2.3	5.4	4.0%	-20(L)/-12(H)

Sub. and Config. denote the substrates and loop configuration, respectively.

BW and Rejection denote the 3dB bandwidth and out-of-band rejection of the passband, respectively.

(L) and (H) denote at low and high frequencies, respectively.

S. and D. denote single-loop and double-loop, respectively.

the passband is 3.16 dB at 96 GHz, the 3dB passband width is increased to 7.8% centered at 96 GHz, and the through signal is reduced to -18 dB at the center frequency. At $P_d = 2.3$ mm, the corresponding phase delay θ between two DFs becomes $5\pi/2$. The measured insertion loss is increased to 5.4 dB at 95.5 GHz due to the destructive phase delay between the DFs. Two transmission zero points can be introduced to achieve a narrow bandwidth of 4% centered at 95.5 GHz. The measured reflection S_{11} and isolation S_{41} of these two cascaded double-loop DFs are below -12 and -10 dB, respectively.

The center frequency of the measured data is slightly higher than that of the simulated ones, which can be attributed to the over etching. The over etching slightly reduces the loop length as well as the width of the MS lines, which slightly reduces the effective dielectric constant. The insertion losses of the DFs in the hybrid substrates

are approximately 0.7 dB lower than their counterparts in LCP substrates, which is due to the AG bond-ply with low dielectric constant and large thickness. Cascading two single-loop DFs can reduce the insertion loss by a factor of 2 dB. The insertion loss, bandwidth, and out-of-band rejection of the single-loop and double-loop DFs in the LCP substrates and hybrid substrates are listed in Table 5.2.

5.4 Summary

In this chapter, I first discussed the detailed challenges for the design of filters and directional filters using the commercial state-of-the-art circuit print technologies in Section 5.1. Then, a second-ordered SIW-based filter 94 GHz was presented in Section 5.2, consisting of two cascaded cavities and an iris window. A passband of 8% centered at 94 GHz and a low loss of 1.5 dB at 94 GHz were demonstrated for the proposed filter. This effort demonstrates the application possibility of the SIW filters in multilayer LCP substrates at *W*-band using commercial PCB technologies. In Section 5.3, slot-coupled travelling-wave DFs in multilayer LCP and hybrid substrates were presented. The proposed single-loop DF consists of two dual-slot quarter-wavelength directional couplers and one loop resonator with a circumference of two wavelengths at 95 GHz. To improve the directivity, asymmetric loop is carefully designed. The passband insertion loss and 3dB bandwidth of the single-loop DF in LCP substrates are approximately 4.6 dB at 94 GHz and 4.9% centered at 94 GHz, respectively. To further improve the directivity and reduce the insertion loss, two DFs can be cascaded in series. An insertion loss of 2.6 dB can be achieved for the cascaded DFs in LCP substrates. Limited by the practical applications, AG bond-ply is utilized to substitute the LCP bond-ply, slightly reducing the coupling efficiency of the coupler and increasing the insertion loss of the DFs. The simulated and measured insertion

loss of the single-loop and double-loop DFs in the hybrid substrates is increased to 5.4 dB and 3.1 dB at 95 GHz, respectively. This is the first time the DFs are designed and demonstrated at *W*-band.

Chapter 6

CONCLUSION AND FUTURE WORK

In this chapter, I first summarize my work presented in this dissertation and emphasize the major accomplishments. Then, my following work on the fully-packaged front-end receiving modules and their applications in wireless systems at *W*-band are discussed.

6.1 Conclusion

In this dissertation, I have presented the individual components of a *W*-band front-end receiving module based on multilayer liquid crystal polymer substrates, which can be potentially utilized in a variety of wireless systems, such as wireless communication, radar, and radiometry. The advantages and benefits of the proposed module are summarized as follows.

- The passive RF components of the proposed module address low dielectric loss at *W*-band due to the low loss tangent and low dielectric constant of the LCP substrates. Additionally, LCP can provide low cost, light weight, and low water absorption for the module.
- The developed multilayer circuits achieve small size, light weight, high density for assembly, low interconnection loss, layer-to-layer isolation, and multi-function capability.
- MCM technologies enable the proposed module to obtain high net gain and low noise figure, which are virtually preferable in all wireless receivers.

- The proposed module is fabricated on 12×18 inch LCP panels using the commercial state-of-the-art large-panel circuit print technologies to reduce the unit cost and manufacturing cycle as well as enable large-volume production.

The proposed receiving module comprises antennas, various transmission lines and their transitions, LNAs and their integration circuits, and filters. All these components except filters can provide an ultra-wide band covering most of the frequencies at *W*-band, which can satisfy the bandwidth requirement of the gigabyte data rate wireless communication. For the narrowband applications, the designed filters can be utilized to efficiently pick out the spectra of interest with low insertion loss and high out-of-band attenuation. The developed components can also be utilized for other applications, such as transmitters and transceivers, whose novelties were presented in the previous chapters separately:

- In Chapter 1, I first discussed *W*-band frequencies and the challenges at *W*-band. Then, I presented three important wireless applications, namely, wireless communication, radar, and radiometry, which can use a common front-end receiving module.
- In Chapter 2, a MS-fed high gain linearly tapered antipodal slot antenna on a 100 μ m thick LCP substrate was presented. By using an MS-to-APSL balun, the proposed antenna achieves an ultra-wide bandwidth from 47 to 110 GHz. An optically-addressed antenna far field measurement system based on optical upconversion was developed and constructed to characterize the antenna at high frequencies. A high gain of 17 \pm 0.5 dBi, narrow beamwidth, low side lobes, and low cross-polarization were demonstrated for the proposed antenna at *E*- and *W*-bands.

- In Chapter 3, I presented a CBCPW-to-stripline vertical transition, a MS line-to-SIW transition, a SIW-to-rectangular waveguide transition, and a MS-to-CPW transition at *W*-band, all of which can be utilized in the multilayer LCP based front-end receiving module. The proposed transitions achieve low insertion loss, low reflection, and ultra-wide bandwidth. Different transmission lines and the corresponding transitions can be utilized for different applications.
- In Chapter 4, the integration and packaging technologies for high-gain multi-chip module at *W*-band were presented. By using these technologies, a double-LNA module was developed in multilayer LCP substrates, achieving high density, light weight, low interconnection loss, and perfect EMC at *W*-band. A high gain of 46-50 dB, a low noise figure of less than 6 dB, and linear phase were demonstrated for the proposed double-LNA module from 80 to 100 GHz.
- In Chapter 5, I presented a SIW-based filter and a MS-based directional filter at 95 GHz. The former is comprised of only twenty four micro vias, and demonstrates the manufacturing possibility of *W*-band SIW filters using the commercial large-panel PCB fabrication technologies. The latter addresses low reflection and high directivity, and can be utilized for frequency division multiplexing. This is the first time that directional filters are reported at *W*-band. Both filters achieve low insertion loss and high out-of-band rejection at *W*-band.

Assembling these components will enable the realization of a high density, high gain, low noise figure, light weight, and low cost front-end receiving module, as illustrated in Figure 6.1. To achieve frequency division multiplexing, directional filters can be integrated into this receiving module. For high-power applications, the last LNA can

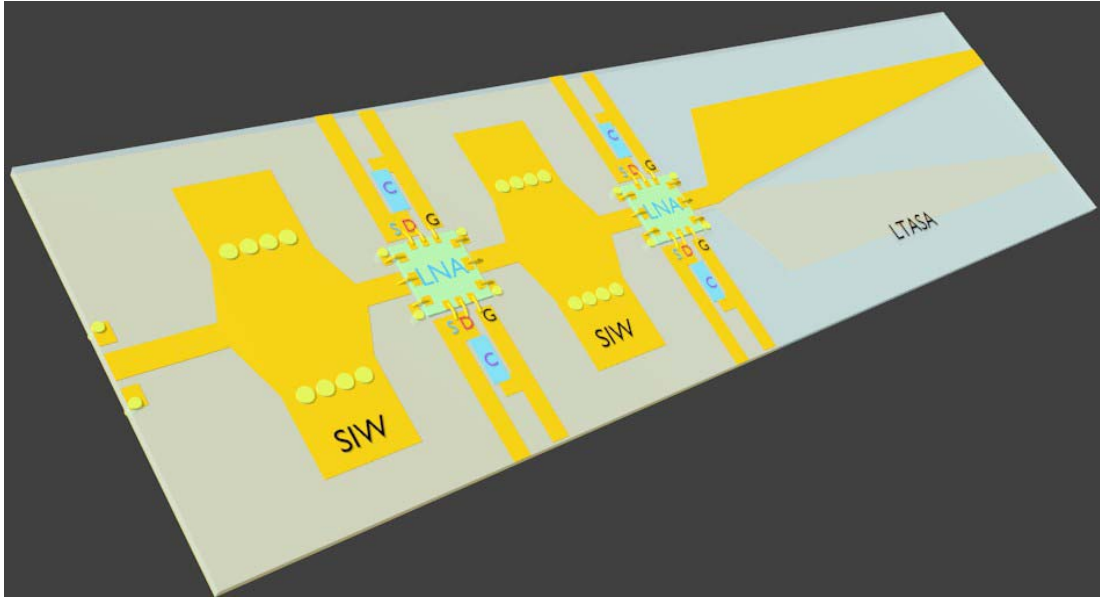


Figure 6.1. Configuration of a multilayer LCP-based ultra-wideband front-end module.

be substituted with a power amplifier. For a more general application, the linearly tapered antipodal slot antenna can be replaced by a standard rectangular horn antenna integrated with the SIW-to-waveguide transition depicted in Section 3.4. The output of the proposed module can be either a rectangular waveguide or CPW by using the transitions presented in Chapter 3. The former is suitable for the general applications, and the latter can be utilized in EO systems.

6.2 Future Work

Future research should focus on additional applications of the *W*-band front-end receiving modules in wireless communication, radar, and radiometry systems. For

instance, the directional filters can be migrated to other frequencies at *W*-band, and cascaded in series to separate the frequencies into different channels in wireless communication systems. The integration of duplexers and switches on LCP substrates may also be of great interest. The former is typically utilized for the monostatic radars, and the latter can be employed for the phased array antenna in radar and communication systems.

At the University of Delaware, an optically-addressed radiometer, passive mmW imager, has been developed at 77 GHz using optical upconversion [2], whose configuration is shown in Figure 6.2. Unlike a focal plane array, a distributed aperture [21] configuration is utilized in this imager to eliminate the need for mmW lens and expensive detection electronics for each pixel. The phase and amplitude of the mmW signals are captured by the antennas distributed in a flat or conformal array. These signals are then up-converted onto a telecommunication laser carrier, generating two optical sidebands, and routed via light weight fiber optic waveguides to an optical processor. This approach can reduce the SWaP of the imaging system. The compact optical processor maps the fiber signals to the homothetic configuration of the antenna array, filters off one of the mmW sidebands, and coherently combines each of the signals onto a standard short wavelength infrared (SWIR) camera for imaging.

To make the system more manufacturable and reduce size, weight, power, and cost (SWaP-C) of the instruments, multilayer LCP based compact receiving modules with simplified housing have been developed for the imager to mitigate these factors. The proposed receiving module comprises three LNAs, two directional filters, a standard WR-10 waveguide as the input interface, and a CPW output for the integration with a LiNbO_3 EO modulator. Multiple LNAs can achieve higher net gain

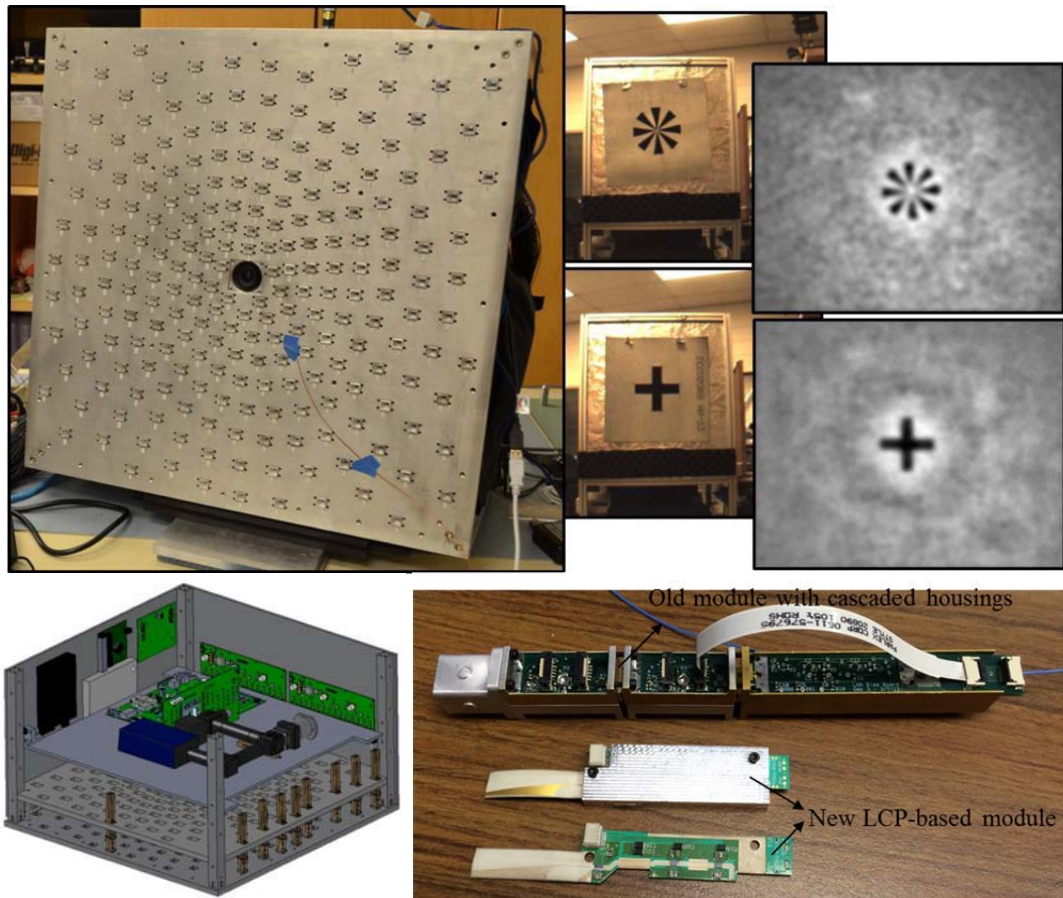


Figure 6.2. Passive mmW imager at 77 GHz.

and low noise figure, thus distinguishing the black body radiation signals from the system noise. The directional filters are utilized to obtain narrow bandwidth and drop the undesired power to the loading ports, while maintaining low reflection back to the LNAs. Figure 6.3 illustrates a packaged receiving module, which can provide a net gain of 62 dB at 96 GHz, a narrow bandwidth of 5% centered at 96 GHz, and a noise

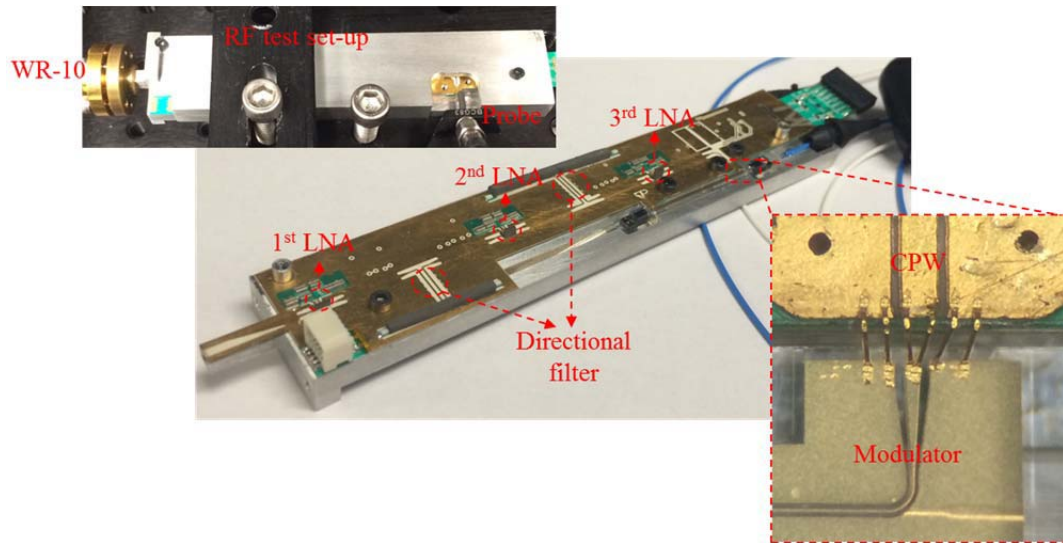


Figure 6.3. Packaged receiving module based on multilayer LCP substrates for mmW imaging at 95 GHz.

figure of less than 6 dB on average at the working frequencies. The detailed design of this module will be discussed in my future paper.

REFERENCES

1. National Telecommunications and Information Administration, *United States Frequency Allocations*, [Online]. Available: https://www.ntia.doc.gov/files/ntia/publications/spectrum_wall_chart_aug2011.pdf
2. R. Martin, C. Schuetz, T. Dillon, D. Mackrides, et al., “Optical up-conversion enables capture of millimeter-wave video with an IR camera” *SPIE Newsroom*, DOI: 10.1117/2.1201208.004406, Aug. 2012.
3. IPC-Association Connecting Electronics Industries, *Market Research from IPC*, [Online]. Available: http://www.ipc.org/3.0_Industry/3.2_Market_Research/Market-Research-Reports-Brochure.pdf
4. P. Macleod, *A Review of Flexible Circuit Technology and its Applications*, Prime Faraday Technology Watch, 2010.
5. IPC-Association Connecting Electronics Industries, *World PCB Production Report for the Year 2010*, [Online]. Available: <http://www.eipc.org/wp-content/uploads/2013/05/2010WorldPCBReport-July-2011-EIPC.pdf>
6. DuPont, *Teflon PTFE Properties Handbook*, [Online]. Available: http://www.rjchase.com/ptfe_handbook.pdf
7. Ferro Electronic Materials, *A6M High Frequency, High Reliability LTCC Taper System*, [Online]. Available: <http://www.ferro.com/noncms/ems/EPM/content/docs/A6M%20LTCC%20System.pdf>
8. D. C. Thompson, O. Tantot, H. Jallageas, G. E. Ponchark, M. M. Tentzeris, and J. Papapolymerou, “Characterization of liquid crystal polymer (LCP) material and transmission lines on LCP substrates from 30 to 110 GHz,” *IEEE Transactions on Microwave Theory and Techniques*, vol. 52, no. 4, pp. 1343-1352, Apr. 2004.
9. Compunetics Inc., private communication, 2013-2015.
10. K. C. Gupta, R. Garg, I. Bahl, and P. Bhartia, *Microstrip Lines and Slotlines*, 2nd edition, Artech House, Norwood, MA, 1996.

11. D. M. Pozar, *Microwave Engineering*, 4th edition, John Wiley & Sons, New York, NY, 2012.
12. Metro Circuits, private communication, 2013-2014.
13. Y. C. Lee and C. S. Park, "A compact and low-radiation CPW probe pad using CBCPW-to-microstrip transitions for V-band LTCC application," *IEEE Transactions on Advanced Packaging*, vol. 30, no. 3, Aug. 2007.
14. I. Bahl, *Lumped Elements for RF and Microwave circuits*, Artech House, 1999.
15. W. L. Gore and Associates, *Microwave/ RF Test Assemblies*, [Online]. Available: http://www.gore.com/MungoBlobs/219/358/GORE_PhaseFlex_120315.pdf
16. Southwest Microwave Inc., commercial communication, 2010-2013.
17. State of the Art Inc., *S0402AF high frequency thin film chip resistor*, [Online]. Available: <http://www.resistor.com/assets/pdf/0402afhifreq.pdf>
18. D. S. Woo, K. W. Kim, and H-C Choi, "A broadband and high gain tapered slot antenna for W-band imaging array applications," *International Journal of Antennas and Propagation*, vol. 2014, ID, 378527, Nov. 2014.
19. F. Tarinou, D. Dousset, J. Bornemann, and K. Wu, "Broadband CPW feed for millimeter-wave SIW-based antipodal linearly tapered slot antennas," *IEEE Transactions on Antennas and Propagation*, vol. 61, no. 4, pp. 1756-1762, Apr. 2013.
20. M. L. Skolnik, *Introduction to Radar Systems*, 3rd edition, McGraw-Hill, New York, NY, 2001.
21. R. D. Martin, S. Shi, Y. Zhang, A. Wright, et al., "Video rate passive millimeter-wave imager utilizing optical upconversion with improved size, weight, and power," *Proc. SPIE 9462, Passive and Active Millimeter-Wave Imaging XVIII, 946209*, May 2015.
22. C. A. Balanis, *Antenna Theory*, 2nd edition, John Wiley & Sons, New York, NY, 1997.
23. Rogers Corporation, *Ultralam3000 liquid crystal polymer circuit material*, [Online]. Available: <http://www.rogerscorp.com/documents>.

24. Federal Communication Commission, *Allocation and Service Rules for the 71-76 GHz, 81-86 GHz, and 92-95 GHz Bands*, FCC 03-248, Nov. 2003.
25. Y. Zhang, S. Shi, R. D. Martin, P. Yao, K. Shreve, and D. W. Prather, "Multilayer liquid crystal polymer based RF front-end module for millimeter wave imaging," *IEEE Antennas and Propagation Society International Symposium (APSURSI)*, pp. 1700-1701, Jul. 2014.
26. K. S. Yngvesson, D. H. Schaubert, T. L. Korzeniowski, E. L. Kollberg, T. Thungren, and J. F. Johansson, "Endfire tapered slot antennas on dielectric substrates," *IEEE Transactions on Antennas and Propagation*, vol. 33, no. 12, pp. 1392-1400, Dec. 1985.
27. B. Veidt, G. J. Hovey, T. Burgess, R. J. Smegal, R. Messing, A. G. Willis, A. D. Gray, and P. E. Dewdney, "Demonstration of a dual-polarized phased-array feed," *IEEE Transactions on Antennas and Propagation*, vol. 59, no. 6, pp. 2047-2057, Jun. 2011.
28. N. Ghassemi and K. Wu, "Planar high-gain dielectric-loaded antipodal linearly tapered slot antenna for E- and W-Band gigabyte point-to-point wireless services," *IEEE Transactions on Antennas and Propagation*, vol. 61, no. 4, pp. 1747-1755, Apr. 2013.
29. D-G Yoon, Y-P Hong, Y-J An, J-S Jang, U-Y Pak, and J-G Yook, "High-gain planar tapered slot antenna for Ku-band applications," *Asia-Pacific Microwave Conference Proceedings (APMC)*, pp. 1914-1917, Dec. 2010.
30. J. Y. Siddiqui, Y. M. M. Antar, A. P. Freundorfer, E. C. Smith, G. A. Morin, and T. Thayaparan, "Design of an ultrawideband antipodal tapered slot antenna using elliptical strip conductors," *IEEE Antennas and Wireless Propagation Letters*, vol. 10, pp. 251-254, Apr. 2011.
31. R. Shireen, S. Shi, and D. W. Prather, "Wideband millimeter-wave bow-tie antenna," *Journal of Electromagn. Waves and Appl.*, vol. 23, pp. 737-746, Sep. 2009.
32. Y. Zhang, S. Shi, R. D. Martin, and D. W. Prather, "Substrate integrated waveguide filter on LCP substrate at 94 GHz," *Microwave and Optical Technology Letters*, vol. 58, no. 3, pp. 577-580, Mar. 2016.
33. J. P. Wilson, C. A. Schuetz, T. E. Dillon, P. Yao, C. E. Harrity, and D. W. Prather, "Passive 77 GHz millimeter-wave sensor based on optical upconversion," *Appl. Opt.*, vol. 51, no. 18, pp. 4157-4167, Jun. 2012.

34. J. Macario, P. Yao, S. Shi, A. Zablock, C. E. Harrity, R. Martin, C. Scheutz, and D. W. Prather, "Full spectrum millimeter-wave modulation," *Opt. Exp.*, vol. 20, no. 21, pp. 23623-23629, Oct. 2012
35. S. Shi, J. Bai, G. J. Schneider, Y. Zhang, R. Nelson, J. Wilson, C. Schuetz, D. W. Grund, and D. W. Prather, "Conformal wideband optically addressed transmitting phased array with photonic receiver," *Journal of Lightwave Technology*, vol. 32, no. 20, pp. 3468-3477, Oct. 2014.
36. J. Coonrod, "Benefits of mixed dielectrics when used for high-frequency PCB applications," *High Frequency Electronics*, pp. 28-36, Nov. 2012.
37. L. Zhu, and K. Wu, "Ultrabroad-band vertical transition for multilayer integrated circuits," *IEEE Microwave and Guided Wave Letters*, vol. 9, no. 11, pp. 453-455, Nov. 1999.
38. N. VandenBerg and L. Katehi, "Broadband vertical interconnects using slot-coupled shielded microstrip lines," *IEEE Transactions on Microwave Theory and Techniques*, vol. 40, no. 1, pp. 81-88, Jan. 1992.
39. X. Huang, and Ke-Li Wu, "A broadband and vialess vertical microstrip-to-microstrip transition," *IEEE Transactions on Microwave Theory and Techniques*, vol. 60, no. 4, pp. 938-944, Apr. 2012.
40. A. Panther, C. Glaser, M. G. Stubbs, and J. S. Wight, "Vertical transitions in low temperature co-fired ceramics for LMDS applications," *IEEE MTT-S Int. Microwave Symp. Dig.* Vol. 3, pp. 1907-1910, May 2001.
41. F. P. Casares-Miranda, C. Viereck, C. Camacho-Penalosa, and C. Caloz, "Vertical microstrip transition for multilayer microwave circuits with decoupled passive and active layers," *IEEE Microwave and Wireless Components Letters*, vol. 16, no. 7, pp. 401-403, July. 2006.
42. R. Valois, D. Baillargeat, S. Verdyme, M. Lahti, and T. Jaakola, "High performances of shielded LTCC vertical transitions from dc up to 50 GHz," *IEEE Transactions on Microwave Theory and Techniques*, vol. 53, no. 6, pp. 2026-2032, Jun. 2005.
43. S. Pan, and J. Fan, "Characterization of vias structures in multilayer printed circuit boards with an equivalent transmission-line model," *IEEE Transactions on Electromagnetic Compatibility*, vol. 54, no.5, Oct. 2012.

44. M. Bozzi, A. Georgiadis, and K. Wu, "Review of substrate-integrated waveguide circuits and antennas," *IET Microw. Antennas Propag.*, vol. 5, Iss. 8, pp. 909-920, 2011.
45. Y. Ding and K. Wu, "Substrate integrated waveguide-to-microstrip transition in multilayer substrate," *IEEE Transactions on Microwave Theory and Techniques*, vol. 55, no. 12, pp. 2839-2844, Dec. 2007.
46. R. Glogowski, J.-F. Zurcher, C. Peixeiro, and J. R. Mosig, "Broadband Ka-band rectangular waveguide to substrate integrated waveguide transition," *Electronics Letters*, vol. 49, no. 9, pp. 602-604, Apr. 2013.
47. C. Li, D. Wu, and K. Seo, "Rectangular waveguide to substrate integrated waveguide transition and power divider," *Microwave and Optical Technology Letters*, vol. 52, no. 2, pp. 375-378, Feb. 2010.
48. L. Xia, R. Xu, B. Yan, J. Li, Y. Guo, and J. Wang, "Broadband transition between air-filled waveguide and substrate integrated waveguide," *Electronics Letters*, vol. 42, no. 24, pp. 1403-1405, Nov. 2006.
49. D. Dousset, K. Wu, and S. Claude, "Millimeter-wave broadband transition of substrate-integrated waveguide to rectangular waveguide," *Electronics Letters*, vol. 46, no. 24, pp. 1610-1611, Feb. 2010.
50. H. Lee, S. Yun, M. Uhm, and I. Yom, "Full-band transition from substrate integrated waveguide to rectangular waveguide," *Electronics Letters*, vol. 51, no. 14, pp. 1089-1090, Jul. 2015.
51. J. L. Cano, A. Mediavilla, and R. Perez, "Full-band air-filled waveguide-to-substrate integrated waveguide (SIW) direction transition," *IEEE Microwave and Wireless Components Letters*, vol. 25, no. 2, pp. 79-81, Feb. 2015.
52. C. L. Zhong, J. Xu, Z. Y. Zhi, and C. X. Jin, "Broadband substrate integrated waveguide to rectangular waveguide transition with fin-line," *Electronics Letters*, vol. 45, no. 4, pp. 205-207, Feb. 2009.
53. J. Li, G. Wen, and F. Xiao, "Broadband transition between rectangular waveguide and substrate integrated waveguide," *Electronics Letters*, vol. 46, no. 3, pp. 223-224, Feb. 2010.
54. H. Jin, W. Chen, and G. Wen, "Broadband transition between waveguide and substrate integrated waveguide based on quasi-Yagi antenna," *Electronics Letters*, vol. 48, no. 7, pp. 355-356, Mar. 2012.

55. A. M. E. Safwat, K. A. Zaki, W. Johnson, and C. H. Lee, "Novel design for coplanar waveguide to microstrip transition," *Microwave Symposium Digest, 2001 IEEE MTT-S International*, vol. 2, pp. 607-610, May 2001.
56. G. Strauss, P. Ehret, and W. Menzel, "On-wafer measurement of microstrip based MIMICs without via holes," *Microwave Symposium Digest, 1996 IEEE MTT-S International*, vol. 3, pp. 1399-1402, Jun. 1996.
57. G. Zheng, J. Papapolymerou, and M. M. Tentzeris, "Wideband coplanar waveguide RF probe pad to microstrip transitions without via holes," *IEEE Microwave and Wireless Components Letters*, vol. 13, no. 12, pp. 544-546, Dec. 2003.
58. S. Bulja, and D. Mirshekar-Syahkal, "Novel wideband transition between coplanar waveguide and microstrip line," *IEEE Transactions on Microwave Theory and Techniques*, vol. 58, no. 7, pp. 1851-1857, Jul. 2010.
59. Z. Tao, J. Wang, and Y. Dou, "Design of broadband microstrip-to-CPW transition," *Electronics Letters*, vol. 50, no. 1, pp. 35-37, Jan. 2014.
60. J. J. Burke, and R. W. Jackson, "Surface-to-surface transition via electromagnetic coupling of microstrip and coplanar waveguide," *IEEE Transactions on Microwave Theory and Techniques*, vol. 37, no. 3, pp. 519-525, Mar. 1989.
61. L. Zhu, and W. Menzel, "Broad-band microstrip-to-CPW transition via frequency-dependent electromagnetic coupling," *IEEE Transactions on Microwave Theory and Techniques*, vol. 52, no. 5, pp. 1517-1522, May 2004.
62. Y-G Kim, K. W. Kim, and Y-K Cho, "An ultra-wideband microstrip-to-CPW transition," *Microwave Symposium Digest, 2008 IEEE MTT-S International*, pp. 1079-1082, Jun. 2008.
63. K. Kitazawa, S. Koriyama, H. Minamiue, and M. Fujii, "77-GHz-band surface mountable ceramic package," *IEEE Transactions on Microwave Theory and Techniques*, vol. 48, no. 9, pp. 1488-1491, Sep. 2000.
64. M. I. Herman, K. A. Lee, E. A. Kolawa, L. E. Lowry, and A. N. Tulintseff, "Novel techniques for millimeter-wave packages," *IEEE Transactions on Microwave Theory and Techniques*, vol. 43, no. 7, pp. 1516-1523, Jul. 1995.

65. A. Tessmann, M. Riessle, S. Kudszus, and H. Massler, "A flip-chip packaged coplanar 94 GHz amplifier module with efficient suppression of parasitic substrate effects," *IEEE Microwave and wireless components letters*, vol. 14, no. 4, pp. 145-147, Apr. 2004.
66. C. Kuo, P. Lin, H. Lu, Y. Jiang, C. Liu, Y. Hsin, and H. Wang, "W-band flip-chip assembled CMOS amplifier with transition compensation network for SiP integration," *IEEE MTT-S Int. Microwave Symposium Digest*, pp. 1-3, May 2010.
67. C. E. Patterson, D. Dawn, and J. Papapolymerou, "A W-band CMOS PA encapsulated in an organic flip-chip package," *IEEE MTT-S Int. Microwave Symposium Digest*, pp. 1-3, Jun. 2012.
68. W. T. Khan, A. L. Vera Lopez, A. C. Ulusoy, and J. Papapolymerou, "Packaging a W-band integrated module with an optimized flip-chip interconnect on an organic substrate," *IEEE Transactions on Microwave Theory and Techniques*, vol. 62, no. 1, pp. 64-72, Jan. 2014.
69. W. T. Khan, C. Ulusoy, M. Kaynak, H. Schumacher, and J. Papapolymerou, "A 94 GHz flip-chip packaged SiGe BiCMOS LNA on an LCP substrate," *Microwave Symposium Digest (IMS), 2013 IEEE MTT-S International*, pp. 1-4, Jun. 2013.
70. D. C. Thompson, M. M. Tentzeris, J. Papapolymerou, "Packaging of MMICs in multilayer LCP substrates," *IEEE Microwave and Wireless Components Letters*, vol. 16, no. 7, pp. 410-412, Jul. 2006.
71. G. Zou, H. Gronqvist, J. P. Starski, and J. Liu, "Characterization of liquid crystal polymer for high frequency system-in-a-package applications," *IEEE Transaction on Advanced Packaging*, vol. 25, no. 4, pp. 503-508, Nov. 2002.
72. K. Aihara, A. Pham, T. Flack, and E. Stoneham, "Development of multi-layer liquid crystal polymer Ka-band receiver modules," *Asia-Pacific Microwave Conference, APMC2007*, pp. 1-4, Dec. 2007.
73. Northrop Grumman, *ALP283 80-100 GHz Low Noise Amplifier Product Datasheet, 2014*, [Online]. Available: <http://www.northropgrumman.com/BusinessVentures/Microelectronics/Products/Documents/pageDocs/ALP283rev0514.pdf>.

74. K. Jayaraj, T. E. Noll, and D. R. Singh, "A low cost multichip packaging technology for monolithic microwave integrated circuits," *IEEE Trans. on Antennas and Propagat.*, vol. 43, no. 9, pp. 992-997, Sep. 1995.
75. R. N. Simons, *Coplanar Waveguide Circuits, Components and Systems*, John Wiley & Sons, New York, NY, 2001.
76. A. Jentzsch and W. Heinrich, "Theory and measurements of flip-chip interconnects for frequencies up to 100 GHz," *IEEE Transactions on Microwave Theory and Techniques*, vol. 49, no. 5, pp. 871-878, May 2001.
77. F. Alimenti, P. Mezanotte, L. Roselli, and R. Sorrentino, "Modeling and characterization of the bonding-wire interconnection," *IEEE Transactions on Microwave Theory and Techniques*, vol. 49, no. 1, pp. 142-150, Jan. 2001.
78. N. G. Alexopoulos and S-C. Wu, "Frequency-independent equivalent circuit model for microstrip open-end and gap discontinuities," *IEEE Transactions on Microwave Theory and Techniques*, vol. 42, no. 7, pp. 1268-1272, Jul. 1994.
79. Agilent Technologies, *Noise Figure Measurement Accuracy – The Y-Factor Method*, [Online]. Available: <http://cp.literature.agilent.com/litweb/pdf/5952-3706E.pdf>.
80. G. Matthaei, E. M. T. Jones, and L. Young, *Microwave Filters, Impedance-Matching Networks, and Coupling Structures*, Artech House, Norwood, MA, 1980.
81. X-P Chen, K. Wu, and D. Drolet, "Substrate integrated waveguide filter with improved stopband performance for satellite ground terminal," *IEEE Transactions on Microwave Theory and Techniques*, vol. 57, no. 3, pp. 694-683, March. 2009.
82. D. Deslandes and K. Wu, "Single-substrate integration technique of planar circuits and waveguide filters," *IEEE Transactions on Microwave Theory and Techniques*, vol. 51, no. 2, pp. 593-596, Feb. 2003.
83. S. T. Choi, K. S. Yang, K. Tokuda, and Y. H. Kim, "A V-band planar narrow bandpass filter using a new type integrated waveguide transition," *IEEE Microwave and Wireless Components Letters*, vol. 14, no. 12, pp. 545-547, Dec. 2004.

84. D. Zelenchuk and V. Fusco, "Low insertion loss substrate integrated waveguide quasi-elliptic filters for V-band wireless personal area network applications," *IET Microwaves, Antennas & Propagation*, vol. 5, Iss. 8, pp. 921-927, 2011.
85. F. S. Coale, "Applications of directional filters for multiplexing systems," *IRE Transactions on Microwave Theory and Techniques*, vol. 6, pp. 450-453, Oct. 1958.
86. H. L.-Morales, A. C.-Chavez, T. Itoh, and J. L. O.-Cervantes, "Dual-band multi-pole directional filter for microwave multiplexing applications," *IEEE Microwave and Wireless Components Letters*, vol. 21, no. 12, pp. 643-645, Dec. 2011.
87. H. L.-Morales, J. S. Sun, A. C.-Chavez, T. Itoh, and J. L. O.-Cervantes, "Novel microstrip diplexer for ultra-wide-band (UWB) and wireless LAN (WLAN) bands," *Journal of Electromagnetic Waves and Applications*, vol. 27, no. 11, pp. 1338-1350, Jun. 2013.
88. J. P. Kim, "Improved design of single-section and cascaded planar directional filters," *IEEE Transactions on Microwave Theory and Techniques*, vol. 59, no. 9, pp. 2006-2013, Sep. 2011.
89. S. R. Zinka, S. Nam, and J. P. Kim, "Multilayer directional filters with transmission zero characteristics," *2008 IEEE Antennas and Propagation Society International Symposium*, pp. 1-4, Sep. 2003.
90. S. B. Cohn and F. S. Coale, "Directional channel-separation filters," *Proceedings of the IRE*, vol. 44, pp. 1018-1024, Aug. 1956.
91. F. S. Coale, "A travelling-wave directional filter," *IRE Transactions on Microwave Theory and Techniques*, vol. 4, pp. 256-260, Oct. 1956.
92. S. Uysal, "Microstrip loop directional filter," *Electronics Letters*, vol. 33, no. 6, pp. 475-476, Mar. 1997.
93. Y. Cheng, W. Hong, and K. Wu, "Half mode substrate integrated waveguide (HMSIW) directional filter," *IEEE Microwave and Wireless Components Letters*, vol. 17, no. 7, pp. 504-506, Jul. 2007.
94. J. L. B. Walker, "Exact and approximate synthesis of TEM-mode transmission-type directional filters," *IEEE Transactions on Microwave Theory and Techniques*, vol. 26, no. 3, pp. 186-192, Mar. 1978.

95. S. Uysal, "Multilayer microstrip loop directional filter," Microwave and Optoelectronics Conference, 2003, IMOC 2003. Proceedings of the 2003 SBMO/IEEE MTT-S International, vol. 1, pp. 25-29, Sep. 2003.
96. S. Sarkar, S. Pintel, N. Kidera, and J. Laskar, "Analysis and application of 3-D LTCC directional filter design for multiband millimeter-wave integrated module," *IEEE Transactions on Advanced Packaging*, vol. 30, no. 1, pp. 124-131, Feb. 2007.
97. T. Tanaka, K. Tsunoda, and M. Aikawa, "Slot-coupled directional couplers between double-sided substrate microstrip lines and their applications," *IEEE Transactions on Microwave Theory and Techniques*, vol. 36, pp. 1752-1757, Dec. 1988.
98. Arlon Technology Enabling Innovation, *GenClad™ 280-The next generation low loss thermoset bond-ply for low-cost multilayer printed circuit boards*, [Online]. Available: https://imageserv11.team-logic.com/mediaLibrary/303/GenClad_280.pdf
99. State of the Art Inc., *S0402AF high frequency thin film chip resistor*, [Online]. Available: <http://www.resistor.com/assets/pdf/0402afhifreq.pdf>
100. Cuming Microwave Corp., *C-RAM high loss silicone rubber sheet absorber for suppression of surface waves*, [Online]. Available: <http://www.cumingmicrowave.com/pdf/310-Rubber%20Sheets/310-4%20C-RAM%20GDSS.pdf>

Appendix

COPYRIGHT PERMISSION

All necessary copyright permissions for the figures and data reproduced in and adapted for this work can be found in the remainder of the document.

Conference Proceedings



Journals

SPIE Digital Library

Books

Collections

Open Access

Contact SPIE Publications

Reprint Permission

Conference Content
Management+Publication
Services

Shipping Info

Reprint Permission

If you are seeking permission to use previously published material, please contact reprint_permission@spie.org. In your e-mail, please include the following information:

- Title and author
- Volume, issue, and page numbers
- What you would like to reproduce
- Where you will republish the requested material.

Requests may also be faxed to SPIE at +1 360 647 1445 (Attention: Reprint Permissions).

Information for authors reproducing their own SPIE material

As stated in the SPIE Transfer of Copyright agreement, authors, or their employers in the case of works made for hire, retain the following rights:

1. All proprietary rights other than copyright, including patent rights.
2. The right to make and distribute copies of the Paper for internal purposes.
3. The right to use the material for lecture or classroom purposes.
4. The right to prepare derivative publications based on the Paper, including books or book chapters, journal papers, and magazine articles, provided that publication of a derivative work occurs subsequent to the official date of publication by SPIE.

Thus, authors may reproduce figures and text in new publications. The SPIE source publication should be referenced.

Web posting policy for papers published in SPIE Journals and Proceedings

SPIE grants to authors of papers published in an SPIE Journal or Proceedings the right to post an author-prepared version or an official version (preferred version) of the published paper on an internal or external server controlled exclusively by the author/employer, provided that (a) such posting is noncommercial in nature and the paper is made available to users without charge; (b) an appropriate copyright notice and full citation appear with the paper, and (c) a link to SPIE's official online version of the abstract is provided using the DOI (Document Object Identifier) link.

Citation format:

Author(s), "Paper Title," Publication Title, Editors, Volume (Issue) Number, Article (or Page) Number, (Year).

Copyright notice format:

Copyright XXXX (year) Society of Photo Optical Instrumentation Engineers. One print or electronic copy may be made for personal use only. Systematic reproduction and distribution, duplication of any material in this paper for a fee or for commercial purposes, or modification of the content of the paper are prohibited.

DOI abstract link format:

<http://dx.doi.org/DOI#>

Note: The DOI can be found on the title page or the online abstract page of any article published by SPIE.

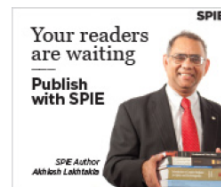
Example:

Neal R. Erickson and Thomas M. Goyette, "Terahertz Schottky-diode balanced mixers," Terahertz Technology and Applications II, Kurt J. Linden,



Thousands of people from academia, industry, and national labs publish their work with SPIE every year. Get the recognition you

- [Proceedings Authors](#)
- [Journal Authors](#)
- [Book Authors](#)



4/20/2016

Reprint Permission - Publications -- SPIE.org

Laurence P. Sadwick, Créidhe M. O'Sullivan, Editors, Proc. SPIE 7215, 721508 (2009).

Copyright 2009 Society of Photo Optical Instrumentation Engineers. One print or electronic copy may be made for personal use only. Systematic electronic or print reproduction and distribution, duplication of any material in this paper for a fee or for commercial purposes, or modification of the content of the paper are prohibited.

<http://dx.doi.org/10.1117/12.807505>

Dear officer,

This is Yifei Zhang, a Ph. D. candidate at University of Delaware. In my dissertation in progress, I referenced your open-access data online ([http://www.ipc.org/3.0 Industry/3.2 Market Research/Market-Research-Reports-Brochure.pdf](http://www.ipc.org/3.0_Industry/3.2_Market_Research/Market-Research-Reports-Brochure.pdf)). Could I get your copyright permission?

Thanks and Best Regards!

Yifei

Dear Yifei,

Thank you for your inquiry. You have our permission to disseminate or publish the link to our catalog of market research reports in your message below, as well as any data that is publicly available on IPC's website.

Best regards,
Sharon

Sharon Starr
Director of Market Research
IPC – Association Connecting Electronics Industries®
3000 Lakeside Drive, Suite 105N
Bannockburn, IL 60015 USA
Tel: [+1 847 597 2817](tel:+18475972817)
Fax: [+1 847 615 5617](tel:+18476155617)
Email: sharonstarr@ipc.org
URL: www.ipc.org